Fall 9-24-2021

3D PRINTED CONCRETE & POLYMER CONCRETE FOR INFRASTRUCTURE APPLICATIONS

Daniel Heras Murcia
University of New Mexico

`

Daniel Heras Murcia
Candidate

Civil, Construction & Environmental Engineering
Department

This dissertation is approved, and it is acceptable in quality and form for publication:

Approved by the Dissertation Committee:

Mahmoud Reda Taha , Chairperson

John Stormont

Maryam Hojati

Kamal H. Khayat

`

3D PRINTED CONCRETE & POLYMER CONCRETE FOR INFRASTRUCTURE APPLICATIONS

by

DANIEL HERAS MURCIA

B.S. Civil Engineering, University of Granada, Spain, 2014.

MSc. Structural Engineering, Technical University of Madrid, Spain, 2015

DISSERTATION

Submitted in Partial Fulfillment of the

Requirements for the Degree of

Doctor of Philosophy

Engineering

The University of New Mexico

Albuquerque, New Mexico

December 2021

`

DEDICATION

I would like to dedicate this work to my parents, Juana Murcia Ruiz and Antonio José Heras Pino, and my brother Álvaro Heras Murcia, for their unconditional love and support.

`

ACKNOWLEDGMENTS

I would like to thank my advisor and committee chair, Dr. Mahmoud Reda Taha, for his mentoring, support, and guidance throughout this research. I would also like to extend my gratitude to Dr. Maryam Hojati, Dr. Kamal H. Khayat, and Dr. John Stormont for serving on my committee.

The generous support of the Dana C. Wood Endowment at the University of New Mexico is greatly acknowledged. The contributions of Mr. Brian Burnett, Mr. Don Kawal, Dr. Gerald May, and Mr. Ken Wylie for creating the Dana Wood Materials and Structures Lab are greatly appreciated.

The continuous support of Transpo Industries and Euclid Chemicals for polymer concrete research at UNM is immensely appreciated.

I would like to thank my colleagues Serafin García Fernández, Mohammed Jaradat, Moneeb Genedy, Shreya Vemuganti, RahulReddy ChennaReddy, and Mohammed Abdellatef for their help and support.

`

3D Printed Concrete & Polymer Concrete for Infrastructure Applications

BY

Daniel Heras Murcia

B.S. Civil Engineering, University of Granada, Spain, 2014.

MSc. Structural Engineering, Technical University of Madrid, Spain, 2015.

Ph.D. Engineering, University of New Mexico, USA, 2021.

ABSTRACT

Additive manufacturing technology has been established as one of the fastest-growing building technologies worldwide. Three-dimensional concrete printing (3DCP) has developed an increasing interest in the last decade due to its prospects as a transformative technology for industries such as the concrete precast. Besides the improvements in automation technologies in construction, traditional construction has faced considerable challenges: high accident rates, labor dependency, significant potential for automation, and high costs associated with the use of traditional formwork. In this context, three-dimensional concrete also referred to as physical prototyping, is a novel construction technique in which the concrete is extruded layer-to-layer. 3DCP is positioning itself as an alternative to conventional fabrication processes under specific circumstances such as complex geometries, expensive workforce, and high automation requirements.

Furthermore, labor investment in the building industry has decreased over the last decades, which places this technology in an advantageous place. Concrete is the most globally consumed material for construction applications due to its competitive cost, worldwide availability of the raw components, good mechanical properties, longevity, and ability to

`

remain fluid before hardening. Cementitious materials present some inherent limitations, such as time-variable rheological properties or low tensile strength, among others. As a consequence of the deposition nature of 3DCP, an anisotropic mechanical behavior has been reported in the literature. This work examines the significance of infill printing patterns on the anisotropic properties of 3D printed concrete.

Polymer concrete (PC) is a type of concrete in which a polymer entirely replaces the cementitious binder. It has been widely used in the construction industry since 1970, offering some advantages such as manufacturing simplicity, remarkable mechanical properties in both compression and tension behavior, low curing time, low permeability, and superior bond between different layers of the same material and to different substrates. Many characteristics make PC a good alternative for the additive manufacturing industry. Research work has been performed to characterize cement-based concrete for additive manufacturing. However, the use of PC in 3D printing is still yet to be examined. This study aims to investigate the potential use of PC for 3D printing for infrastructure applications.

Textile reinforced concrete (TRC) has gained attention from the construction industry due to its lightweight, high tensile strength, design flexibility, and corrosion resistance with remarkably long service life. Structural applications that utilize TRC components include precast panels, structural repair, waterproofing elements, and façades. TRC is produced by incorporating multiple textile fabrics into thin cementitious concrete panels. In this thesis, innovative reinforcement techniques such as interlayer textile reinforcement are explored for both cement and polymer-based 3D printing materials.

Finally, the level of maturity of 3DCP as an emerging technology is examined. The potential of 3DCP as a technology to improve infrastructure resilience is investigated.

`

Table of Contents

`

`

`

List of Figures

`

`

`

`

`

`

List of Tables

`

`

List of Equations

`

List of Abbreviations and Acronyms

3D	Three-dimensional
3DCP	Three-dimensional concrete printing
3DPC	Three-dimensional printed concrete
AM	Additive manufacturing
FF	Freeform fabrication
ISO	International organization for standardization
ASTM	American society for testing and materials
PC	Polymer concrete
ET	Emerging technology
TRC	Textile reinforced concrete
TRPC	Textile reinforced polymer concrete
3DP-TRC	Three-dimensional printed textile reinforced concrete
3DP-TRPC	Three-dimensional printed textile reinforced polymer concrete
CNF	Carbon nanofiber
MMA	Methyl Methacrylate
MoR	Modulus of Rupture

`

List of Symbols

τ_s	Static yield stress
$\dot{\gamma}$	Shear rate
τ_{s0}	Static yield stress at the time of deposition
G	Shear elastic modulus
A_{thix}	Structuration rate
S	3D printed contour length
h_0	3D printed layer height
t_0	Time of deposition
V	In-layer printing speed
$\dot{H}$	Buildup rate (rising speed)
H	Final 3D printed object height
ρ	Density of the 3D printed material
g	Gravitational constant
τ_d	Dynamic shear/yield stress
k	Consistency
n	Flow index
A, B	Linear fitting parameters for time-dependent regression of the consistency *k*(t)
C, D	Linear fitting parameters for time-dependent regression of the flow index *n*(t)
E, F	Exponential fitting parameters for time-dependent regression of the static yield stress τ_s(t)

`

τ_c	Critical yield stress
η	Viscosity

`

Preface

During this Ph.D. (Fall 2017-Now), the following papers have been published:

- *D. Heras Murcia*, M. Abdellatef, M. Genedy, M. Reda Taha, Rheological Characterization of 3D Printed Polymer Concrete, ACI Materials Journal. Accepted for publication (n.d.).
- *D. Heras Murcia*, M. Genedy, M. Reda Taha, Examining the significance of infill printing pattern on the anisotropy of 3D printed concrete, Construction and Building Materials. 262 (2020) 120559. https://doi.org/10.1016/j.conbuildmat.2020.120559.
- M. Reda Taha, B.M. Ayyub, K. Soga, S. Daghash, *D. Heras Murcia*, F. Moreu, E. Soliman, Emerging Technologies for Resilient Infrastructure: Conspectus and Roadmap, ASCE-ASME Journal of Risk and Uncertainty in Engineering Systems, Part A: Civil Engineering. 7 (2021) 03121002. https://doi.org/10.1061/AJRUA6.0001134.
- *D. Heras Murcia*, M. Reda Taha, C. Minnig, J. Gisiger, U. Rösli, J. Stormont, Nano Sealant for CO2 Seal Integrity and Overcoring at Mont Terri, SSRN Journal. (2021). https://doi.org/10.2139/ssrn.3819742.
- *D. Heras Murcia*, M. Genedy, M. Reda Taha, 3D-printing Polymer Concrete for Infrastructure Applications. Proceedings, 1st International Conference on 3-D Printing and Transportation. November, 2019: Washington DC, USA.
- *D. Heras Murcia*, M. Genedy, M. Reda Taha, "The Effect of Infill Pattern on Anisotropy of 3D-Printed Concrete" The Engineering Mechanics Institute Conference 2021 and Probabilistic Mechanics & Reliability Conference 2021 (EMI 2021/PMC 2021), May 2021.

`

- Provisional patent: Invention No. 2020-090, titled "3D-Printed Segmental Concrete Structures and Methods of Making". M. Reda Taha, *D. Heras Murcia,* M.A. Dehghani Najvani.
- *D. Heras Murcia*, B. Comak, E. Soliman, M. Reda Taha, Flexural Behavior of Textile Reinforced Polymer Concrete. Submitted for review to Journal of Construction and Building Materials.
- M. Abdellatef, *D. Heras Murcia*, J. Hogancamp, E. Matteo, J. Stormont, M. Reda Taha, The Effect of Multi-Size Carbon Fibers on The Mechanical and Fracture Characteristics of Fiber Reinforced Cementitious Composites. Under review.
- P.G. Hubbard, Z. Chen, K. Soga, M. Reda Taha, *D. Heras Murcia*, P. Tang, B. Glisic, O. Ozbulut, C. Ford, A framework for evaluating emerging technologies' contributions to system resilience. Submitted for review to Natural Hazards Review.
- K. Soga, P.G. Hubbard, M. Reda Taha, Z. Chen, *D. Heras Murcia*, P. Tang, B. Glisic, O. Ozbulut, C. Ford, N. Lu, Y.-F. Su, Evaluation of emerging technologies for system resilience contributions: case studies. Submitted for review to Natural Hazards Review.

`

Chapter 1. Introduction

Motivation and Problem Statement

Freeform fabrication (FF), also known as rapid prototyping, rapid fabrication, or solid freeform fabrication, is a compilation of technologies that apply to many markets. Applications for this set of technologies share a common characteristic: manufacturing products with complex geometries on a small production scale. Traditionally, this technology has been used for prototyping since the quality of the parts was not good enough for mechanical applications. Recently, the evolution of automation robotics with tighter manufacturing tolerances, increased time efficiency, and the creation of post-processing techniques has open the market applications to many market niches such as customized parts for structural, medical, and architectural applications, among others as well the mass production of customized parts [1].

Additive manufacturing (AM) is a subset of FF backgrounds from topography and photo sculpture fields that backdate as early as 1890 [1]. Nonetheless, modern AM techniques were envisioned for the first time in the 1950s and evolved through the second half of the 20th century by inventors such as Munz [2], Swainson [3], Housholders [4], and Kodama [5], among others.

AM is defined by the ISO/ASTM terminology [6] standard as the "*process of joining materials to make parts from 3D model data, usually layer upon layer, as opposed to subtractive manufacturing and formative manufacturing methodologies"*. Although the term "3D-printing" is commonly used as a synonym for AM, there are a variety of AM technologies that, depending on the technology and the materials used, significantly diverge from the traditional layer to layer material extrusion. To clarify this, the American Society

`

for Testing and Materials (ASTM) defined a set of standards that organize the range of Additive Manufacturing processes into seven categories, as shown in Figure 1. The main features of each one of those processes are described herein.

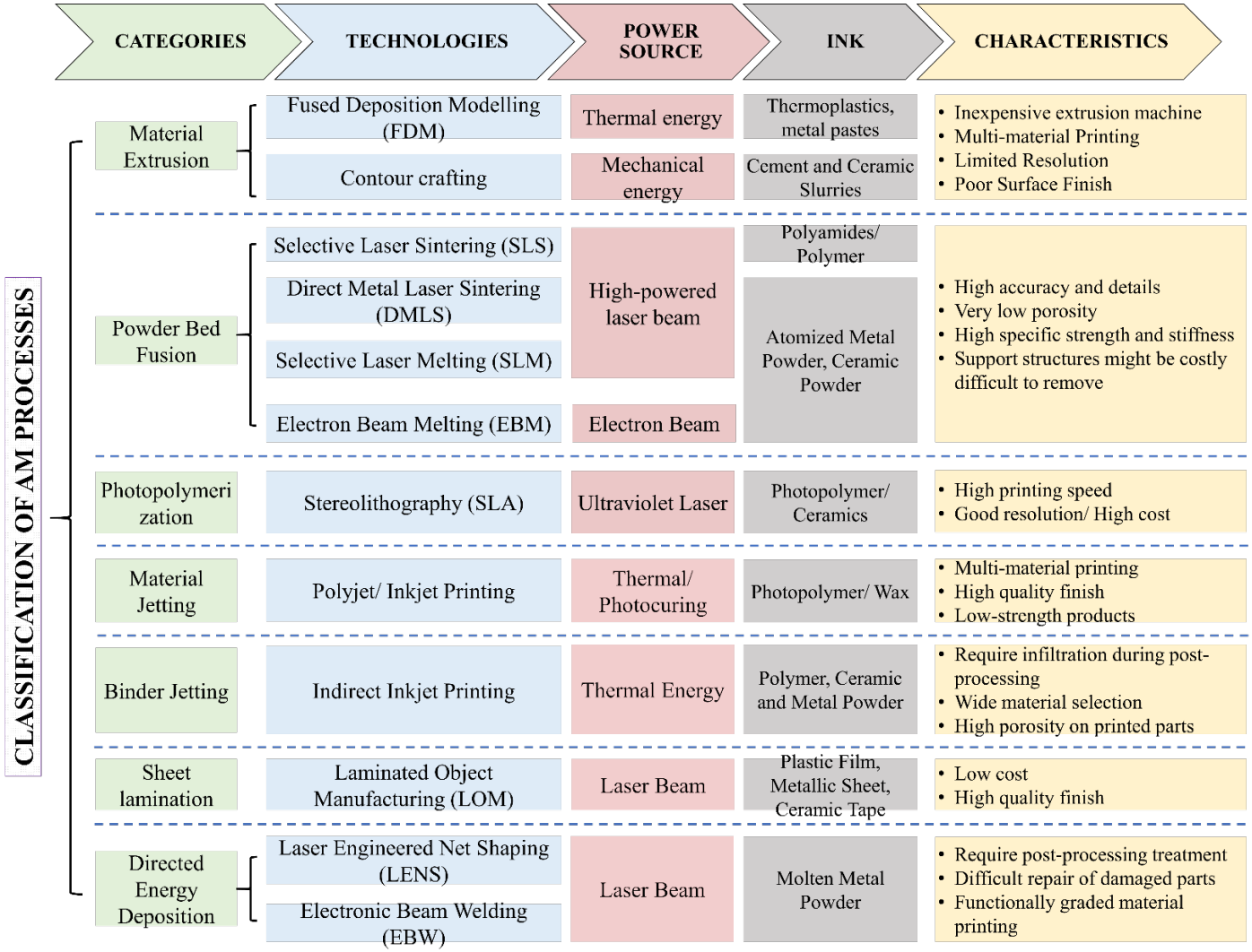

Figure 1. Classification of additive manufacturing processes by ASTM International (ISO/ASTM52900-15). Adapted from [7].

`

Additional information on AM processes can be found elsewhere [7,8]. The global market value of AM systems, materials for this process, software, and complimentary services was estimated to be about $13 billion in 2016 [9]. According to the Wohlers report [10], AM is experiencing exponential growth, specifically in industrial fields such as automotive, aerospace, and defense applications. It is worth mentioning the development of new markets such as biomedical and dental. In this context, AM has been drawing attention from the construction sector. The main AM category of interest for large-scale infrastructure applications is material extrusion, particularly contour crafting technology, which is compatible with concrete and other pastes.

3D printing technology is abruptly gaining ground [11] (Figure 2), positioning itself as an alternative to traditional fabrication processes for cases where geometries might be intricate, the workforce is expensive, or a high degree of automatization is profitable.

Furthermore, the nature of some construction projects requires the manufacturing of custom products in limited quantities. 3D printing could be a transformational technology for this type of project since it is alleged to reduce design and execution times, enhance communication, enable digitization, improve collaboration processes, and narrow the existent gap between engineering and design [12]. On the other hand, labor investment in the building industry has suffered a noticeable decline over the last decades [13], placing 3D printing technology in an advantageous place.

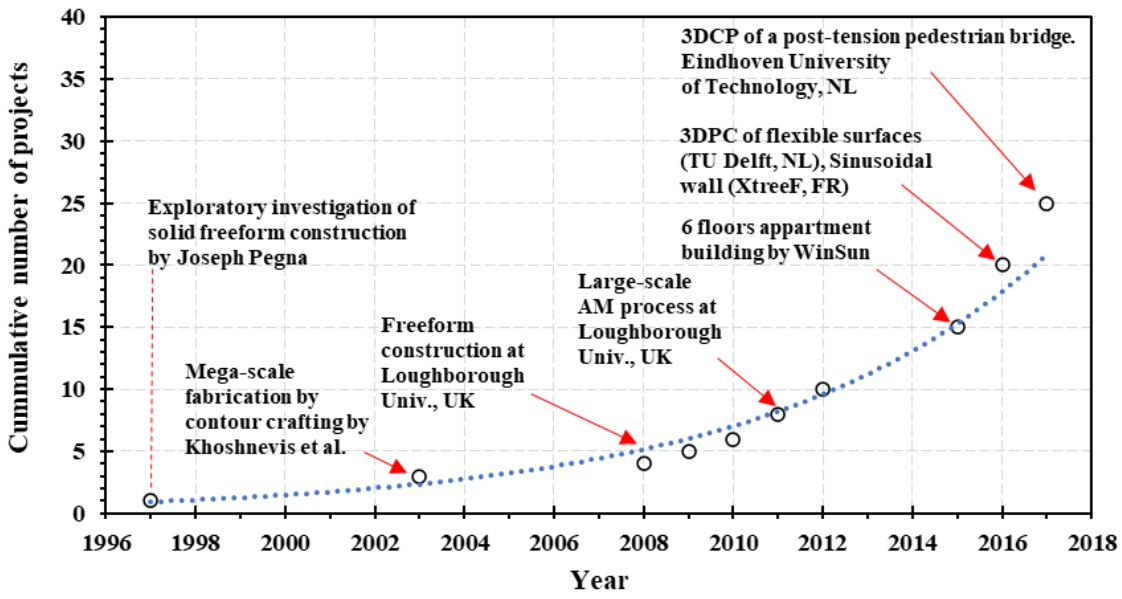

Figure 2. The exponential rise in large-scale 3D printed projects for construction applications. Adapted from [11].

Most 3D printing materials for infrastructure applications are composed of an aggregate matrix surrounded by a pozzolanic material that acts as a binder. The matrix hardens by an exothermic hydration process [14]. Additions and additives such as silica fume, fumed silica, fly ash, superplasticizers, and retarders have been used to achieve specific properties for 3D printing applications such as high strength, delayed hardening, thixotropic behavior, high ductility, and extended setting time, among others.

It has been established that AM of most materials (polymer, metallic, and ceramics) can introduce microstructural heterogeneities, such as porosity and weaken interfaces, resulting in an overall anisotropic behavior [15]. The presence of these potential defects due to the printing process and the likely presence of weakened interfaces between layers suggest that 3DPC can have an anisotropic mechanical behavior [16–22].

`

Nevertheless, the low tensile strength of cement-based materials, the challenge to incorporate reinforcement, and the anisotropic behavior of the printed structures make those materials unsuited for some structural applications. Moreover, the potential presence of defects during the manufacturing (printing) process due to factors such as the printing settings and the material's time-dependent rheological behavior makes the harden mechanical behavior of the 3D printed concrete (3DPC) challenging to predict. Research efforts need to focus on understanding the factors behind such directional dependency. In this context, it is crucial to comprehend the fundamental mechanisms by which bond is formed in 3D printed concrete and realize how the constituent materials, the concrete mix design, and the printing process affect the rheological and hardened properties of the printed product.

Most of the research in concrete printing has focused on investigating cement-based 3D printable materials. Most recently, due to the high environmental cost of cement production in terms of CO_2 and other contaminants emissions, alternative pozzolanic materials such as fly ash and slag have been investigated as alternative partial replacement materials.

Polymer concrete (PC) has been widely studied for construction applications. PC consists of entirely replacing the cement as a binder by using a thermosetting polymer matrix. PC offers some advantages due to its physicochemical properties such as low permeability, high ductility, chemical resistance, high mechanical strength in compression and tension, and excellent bond between layers of the same material and other substrates. These properties make PC a promising candidate for concrete printing, especially in applications requiring demanding performance. This research investigation is the first attempt to use polymer concrete (PC) as an alternative material for 3D printing to the best of the author's knowledge. This research addresses the characterization of PC for 3D printing applications in terms of

`

rheological and mechanical properties. Moreover, the implementation of reinforcement in concrete printed structures has been a challenging subject of research. In this context, this work also researches the use of textile fiber mesh reinforcement at the interlayer interface as an innovative alternative reinforcing mechanism for 3D printed materials will be analyzed. The combined use of cement-based and polymer-based mixes with this textile reinforcement will be explored.

Objective and Contribution

This research analyzes new materials and manufacturing methods amenable to concrete printing that could push the functionality of concrete printing to new applications. The contributions of this work are listed herein:

- Understanding the nature of the directional-dependent behavior of 3D printed concrete. Examining the significance of infill patterns on the anisotropic properties of 3DPC and how those mechanical properties compare to conventionally cast concrete.
- Analyzing the viability of polymer-based concrete (PC) as an alternative to classical cement-based mixes for additive manufacturing processes. Characterize the properties of this innovative material and its suitability for printing applications from a rheological and mechanical perspective.
- Compare the mechanical characteristics of PC, and cement-based textile reinforced 3D printed composites manufactured by a distinct-layer casting technique.
- Evaluate the possible use of textile reinforcement in 3D printed concrete as an alternative reinforcement, given its potential for automation. The thesis also quantifies the improvement in the mechanical properties of the manufactured product.

`

- Investigate the level of maturity of concrete 3D printing as an emerging technology at various scales and identify the potential contributions towards infrastructure resilience.

Dissertation Layout

This dissertation consists of a general introduction (Chapter 1) to AM technology as well as concrete 3D printing and an analysis of the rationale behind the market (AM) and research (concrete 3D printing) eruption of these technologies. Chapter 1 also outlines the research gaps that drive this research work.

Chapter 2 consists of a set of comprehensive literature reviews about the following topics:

- Additive manufacturing of concrete. Inception and overview of the different technologies for concrete materials.
- Rheological behavior of 3D printed concrete.
- Mechanical anisotropy in 3D printed concrete. The interdependence of factors affecting the mechanical behavior of 3D printed concrete is examined. Material design, printing, rheological, and harden properties are examined, and their dependency through a review of the work performed up to date.
- Polymer concrete (PC) as an alternative material for 3D printing. The potential of polymer-based composites (in particular polymer concrete) for 3D printing from a rheological and mechanical perspective is analyzed.
- Reinforcement of 3D printed concrete structures. A state-of-the-art review of the different reinforcement systems implemented in 3D printed structures is provided.
- Textile reinforcement of cement composites. The use of textile reinforcement for structural and infrastructure reinforcing applications is analyzed. The advantages of

`

textile reinforcement over traditional reinforcement typologies are evaluated by reviewing the current literature on the topic.

Chapter 3 examines the anisotropic nature of 3D printed concrete. The significance of the infill printing patterns is analyzed. The mechanisms that could be inducing that anisotropy are investigated.

Chapter 4 investigates the potential of polymer concrete as an alternative material for 3D printing for specific applications. An in-depth rheological analysis, as well as mechanical analysis, is performed for this material. The use of carbon nano fibers as a rheology modifier for polymer concrete is also explored in Chapter 5.

Chapter 6 details the flexural properties of distinct-layer casted cement and polymer composites adding textile reinforcement. This chapter aims to determine whether PC is compatible with this type of reinforcement and explore any potential synergies on using PC with textile reinforcement.

Chapter 7 explores the implementation of textile reinforcement technology into 3D printing for both cement and polymer-based materials.

Chapter 8 analyzes concrete 3D printing as an emerging technology and the potential socio-economic impacts that this technology could have. The potential contributions of this technology towards infrastructure resilience are also detailed.

In Chapter 9, conclusions about the investigations and recommendations for future work are presented. Finally, all the references used in this dissertation are cited. The outline of this dissertation is summarized in the flow chart shown in Figure 3.

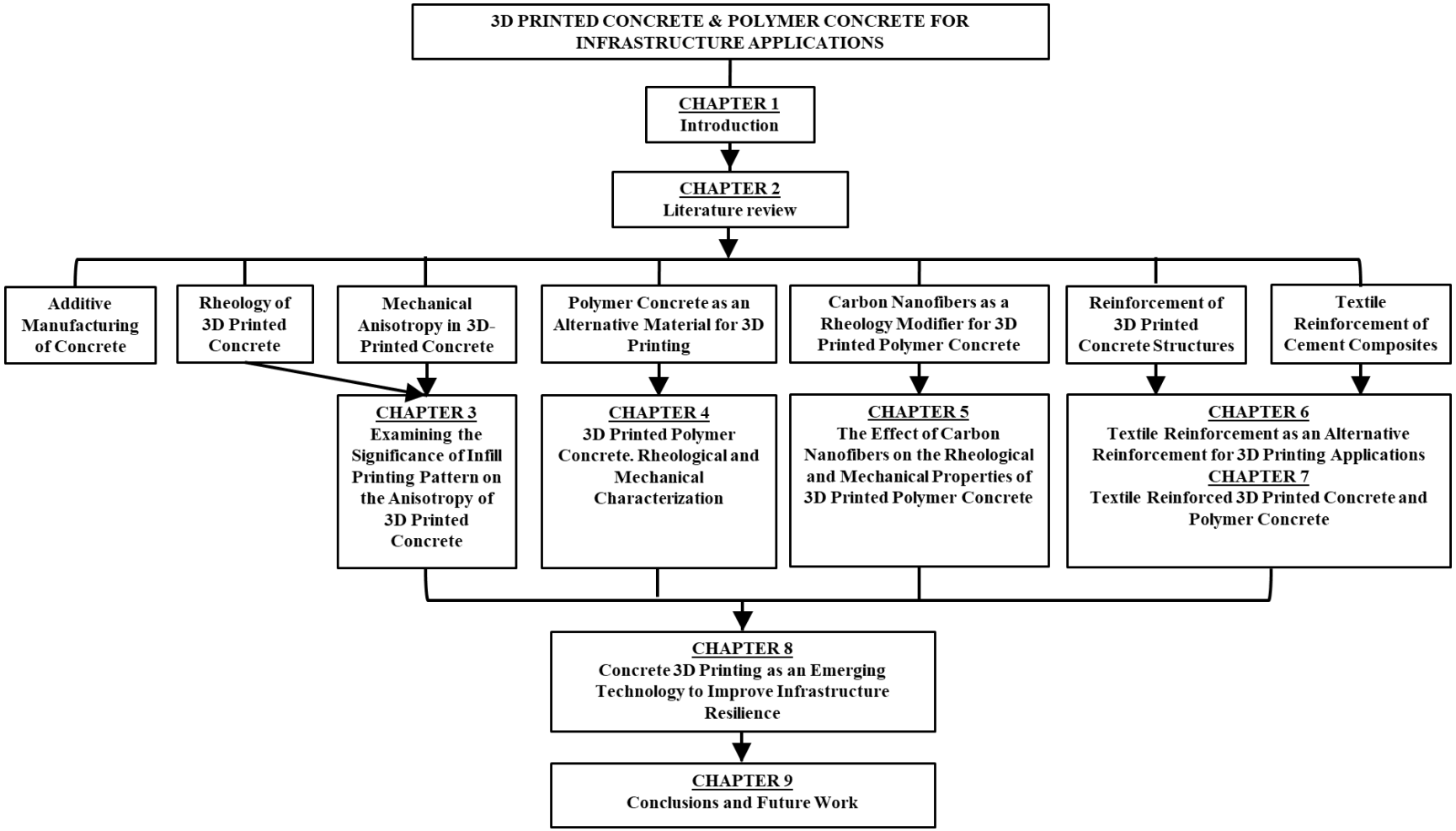

Figure 3. Flowchart of dissertation outline.

`

Chapter 2. Literature Review

Additive Manufacturing of Concrete

Different aspects push the construction industry towards a high automatization degree, such as the progressive increase in labor and production costs, the costs associated with construction times, and the ability to have more freedom in design due to the absence of precast techniques [23]. AM is already being used for rapid prototyping and custom mass production in other industries such as aerospace or automotive manufacturing. The technology for thermoplastic materials has become so well adopted that 3D printers are now affordable for home and industrial use [9].

AM technologies are often referred to as “rapid prototyping”. Rapid since the production of the object from a conceptual state until its manufacturing is relatively fast. Prototyping refers to the fact that the process is too slow for mass production [24]. Nonetheless, in construction, structural elements are typically customized in terms of material design, geometry, and size due to each design's specific and unique conditions. To manufacture each component, there is a need to customize forms and molds. There is a clear cost-saving opportunity because of the use of AM technology to design custom-made elements. Significant cost savings could be achieved since the design can be optimized from a material and topology perspective, and there is no need for molds [24]. The costs associated with formwork in traditional reinforced concrete are estimated to be one-third of the total construction costs and one-third to one-half of the construction time [25,26]. For intricated geometrical designs, the utilization of monetary and time resources could be even more intensive. AM could be more cost-effective than traditional precast methods for these distinct custom-made elements in which the number of elements produced does not exceed a certain critical number. AM not only can

`

reduce costs in some construction applications, but it could also transform the designing approach, enabling architects to conceptualize unique structures [27–30] since the limitations in traditional mold casting production will be removed by AM technology. From a technical perspective, Pacillo et al. [31] summarized the advantages and opportunities of AM for construction:

- Automation of the construction process on-site and off-site [12].
- More freedom in geometrical design. Functional and topological optimization [12,32,33].
- Multi-material printing with properties on-demand.
- Reduction of material waste due to the structural optimization and the absence of formwork.
- Increase of safety at the construction workplace due to the reduction in labor force.

Since the inception of the use of a cement material for AM by Pegna [33], concrete AM for concrete material has undergone exponential growth in research and development, as depicted in Figure 2. Nowadays, for concrete AM there are three main techniques: contour crafting incepted by Khoshnevis [34], D-shape (monolithic objects), and concrete printing [35]:

- *Contour crafting* has been under development since its invention by Khoshnevis [34]. This technology is based on the extrusion of a cement-based material against a trowel that allows for a smooth surface finish [35]. The structure is created by the subsequent deposition of layers.

`

- *Concrete printing* is very similar to contour crafting, but the cement-based material is engineered from a rheological perspective to retain its shape preventing the need to use any trowel.
- *D-shape technology* does not follow a layer-by-layer approach, and it is based on the selective placement of binder in a powder bed at the desired location to be solid.

Some authors [27] have envisioned large-scale 3DPC into three main applications for the construction industry, namely 3D printing elements as a prefabrication technique, 3D printing of formworks, and 3DPC on-site. For large-scale 3DPC on-site, numerous complex logistics such as 3D printer installation and calibration, material preparation and pumping, transportation, assembling, and disassembling of the precise 3D printer equipment must be considered [36–40]. All these factors could make 3DCP for in-field applications not as profitable as the prefabrication of elements. The interdependency of factors affecting the economic and ecological efficiency of concrete 3D printing is depicted in Figure 4.

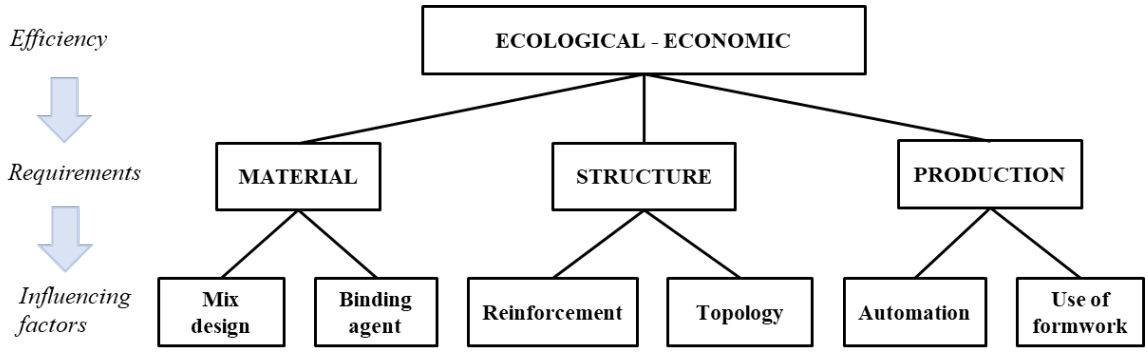

Figure 4. Factors affecting the economic and ecological efficiency of concrete 3D printing. Adapted from [41].

This thesis will be focused on concrete printing technology. This process is very similar to other AM techniques since the object is designed as a solid geometry mesh, then it is processed by a software that divides it into slices creating a code for the printing process, and

`

finally is printed and post-processed if needed. Since its origin [42], layered extrusion concrete printing techniques have relied on the sequential construction of geometries by stacking one layer over the previous one. Relevant work has been performed to design new cementitious materials for this purpose and to characterize the fresh and hardened properties of 3D printable concrete [23,43]. Extensive literature reviews about concrete additive manufacturing (AM) state of the art can be found elsewhere [11,12,44–47]. This study will not cover AM methods regarding selective binder jetting (e.g. D-shape) [48,49].

Rheology of 3D Printed Concrete

Conventional cement-based concrete is widely used as a construction material due to its ability to flow before hardening and adopt the shape of the formwork as it is poured. Contrarily, in layered extrusion additive manufacturing, commonly known as 3D printing, concrete is shaped without formwork. Then, the filament material is required to resist the gravitational stresses imposed by its self-weight and the weight imposed by the printed structure as it is extruded above it. This dictates stringent time-dependent rheological requirements of materials used for 3D printing. The printability requirements are depicted in Figure 5.

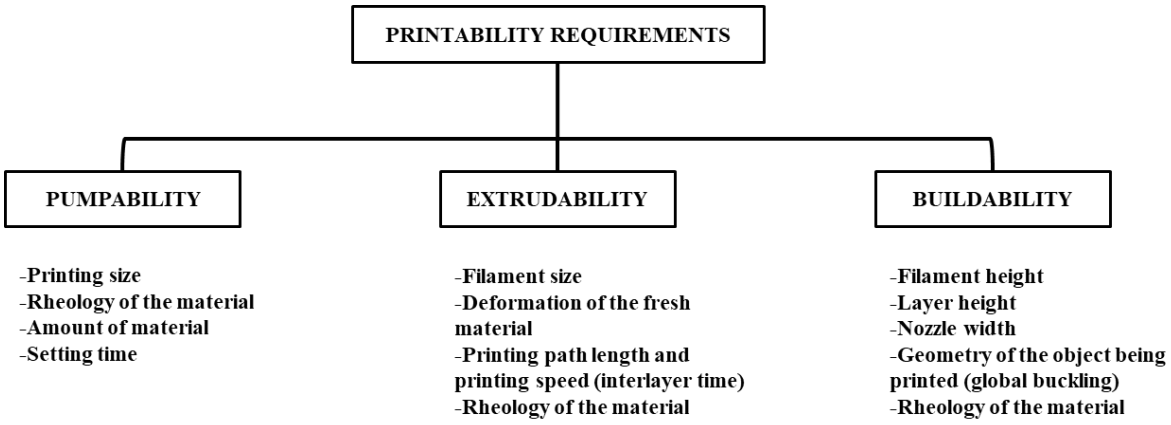

Figure 5. Requirements for successful 3D printing.

`

Most cement-based materials show a dualistic rheological character. They can be considered solid when stress smaller than a critical value is applied, keeping the shape given. This characteristic is crucial for additive manufacturing since concrete is shaped by layer deposition. When the stress exceeds this threshold value, they behave as viscous liquids, and they flow if the stress is maintained. This threshold value is called critical yield stress, τ_c , also known as static yield stress (τ_s) (Figure 6).

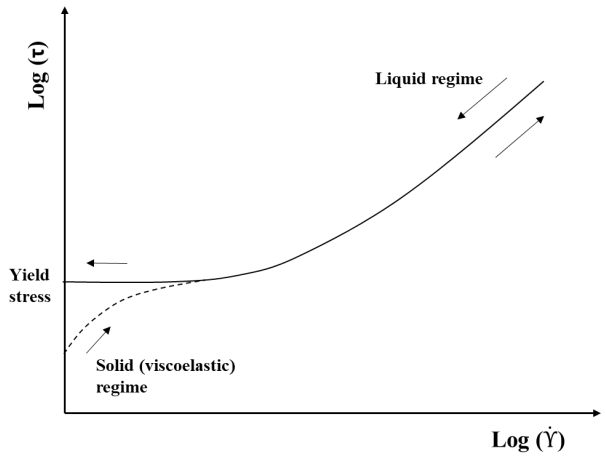

Figure 6. Apparent flow curve. Yield stress vs. shear rate from an increase-decrease shear rate ramp. Extracted from [50].

Concrete also shows a time-dependent behavior called thixotropy, meaning that their resistance to flow increments after an increasing time at rest. Thixotropic fluids can be defined as dispersions, which, when at rest, construct an intermolecular system of forces that increases the fluid's viscosity, also known as flocculation. For the material to flow, considerable external energy must break these binding forces, reducing its viscosity. This is known as the de-flocculation phase. In rheological terms, applied stress equal to or larger than a material's static yield stress will result in de-flocculation.

`

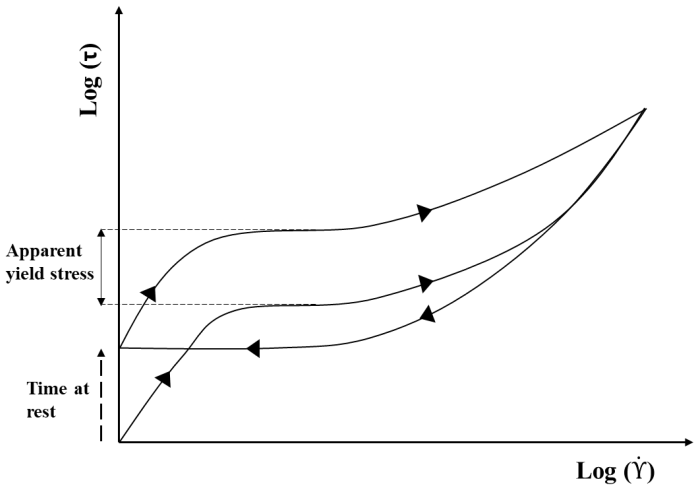

Figure 7. Apparent flow curve. Shear stress vs. shear rate from an increase-decrease shear rate ramp after different times at rest (thixotropic behavior). Extracted from [50].

In the liquid regime, the apparent viscosity relates both shear stress and shear rate. The shear rate ($\dot{\gamma}$), is defined as the ratio of the relative velocity (V) of the pseudo-solid planes to the sample thickness (H): $\dot{\gamma} = V/H$ or as the time variation of the deformation: $\dot{\gamma} = (\Delta x/H\Delta t)$. To ensure continuity with the solid regime, the viscosity (η) should tend towards infinity as the shear rate tends to zero (material stops flowing). This is what is generally observed in practice (Figure 8). The apparent viscosity η is then $\eta = \tau_c/\dot{\gamma}$, which tends to infinity when $\dot{\gamma}$ tends to zero. In general, the Herschel-Bulkley model describes this relationship as follows (Equation 1):

Equation 1. Herschel-Bulkley model. General equation.

$$\tau > \tau_c \xrightarrow{Then} \tau = \tau_c + k\dot{\gamma}^n \qquad \text{(Equation 1)}$$

In which *k* and *n* are material parameters. This model can fit experimental data for a wide range of shear stresses and shear rates. Therefore, this model can represent the material behavior from very slow flows (typically at shear rates of the order of 10^{-2} s^{-1}) to rapid

`

flows (at shear rates of the order of 100s $^{-1}$). No significant physical meaning has been provided so far for the fitting parameters (*k* and *n*) in the general form of the model. Thus, this model is just an appropriate fit for the data. The Bingham model is a particular case of the Herschel-Bulkley model for n=1. This model might not be the correct prediction for cases with a wide range of shear rates. In the Bingham model, the fitting parameter (*k*) represents the viscosity of the fluid (Figure 8).

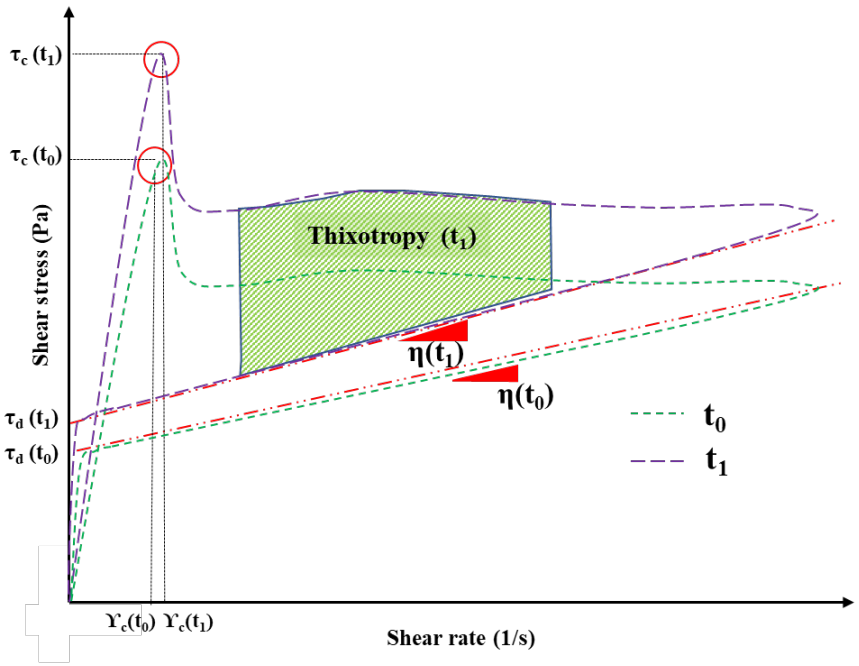

Figure 8. Schematic representation of the thixotropic Bingham plastic material model and parameters.

On the other hand, the material's elastic modulus can be related to the interaction between the structure's elements in the solid regime. The critical (or static) yield stress value (τ_c) is the stress required to break the structure. For most printing processes, we only flow the material while extruding it through the nozzle. Most of the time, the material is in a solid regime, being the elastoplastic behavior of the material in this phase especially relevant. Before the

`

yield stress, cement-based materials show a roughly elastic behavior in which the shear elastic modulus (G) can be determined as $G = \tau_c/\gamma_c$ with γ_c being the critical shear strain at flow onset, as shown in Figure 8.

The thixotropy nature of those materials is represented physically by the ability to build up an internal structure at rest (which is a crucial feature for most printing applications) [51]. After deposition, when the material is at rest, it shows initial yield stress and shear strain (τ_0 and γ_0). If the material is kept at rest, those parameters evolve with time. Experimental results [52–54] show that the shear stress and the shear modulus increase as a function of time, while the shear rate decreases with the time at rest. The material then becomes stronger (higher yield stress) and stiffer (higher shear modulus) [53]. The rate at which the static yield stress increase with time is defined in the literature as structuration rate, A_{thix} (Pa/s). If this rate is constant with time, as suggested by [55,56], the yield stress of the material after a resting time *t* is defined as $\tau_c(t)=\tau_{c0}+A_{thix}t$. It must be noted that assuming that the structuration rate is constant does not seem to apply to all printable materials from literature. For instance, some material tested [52] seemed to go through the exponential growth of its bulk strength. From a physical point of view, the cement-based material evolution and the transition between those two regimes can be explained by flocculation and the material's ability to nucleate early hydrates at the pseudo-contacts points between cement grains in the flocculated structure formed by the cement grains [56]. In a chronological timeframe, the following phases can be described:

- The cement particles are dispersed right after the mixing stage, and no interaction is observed (Figure 9).

`

- Cement particles start flocculating and forming a network of interacting particles that resist stress and display an initial elastic modulus G_0 and an initial yield stress τ_{c0} due to the attractive colloidal forces (Figure 9). This phase is referred to as flocculation [56]. This flocculation is due to the equilibrium between the colloidal forces between cement particles that oppose the interstitial water's viscous dissipation between cement grains [56]. This phase can start seconds after the flow stops and last for tenths to hundreds of seconds until the material reorganizes its particles to its final configuration [53,56].
- Calcium silicate hydrates (CSH) nucleation occurs at the contact points between particles, although the material is still in the dormant period. Those interactions possess higher energy, increasing the macroscopic elastic modulus of the material. This phenomenon usually takes place simultaneously with the flocculation.
- An increase in the size or numbers of hydrates bridges between percolated cement particles (Figure 9). This phase is called structuration, and permanent chemical reactions occur at a microscopic range as the cement hydrates. These bonds can be broken if the material is re-sheared and formed again (if the chemical reactions allow it). This process can be reversible if the mixing power is enough to break those bonding bridges [55]. If not, it would result in a loss of workability.

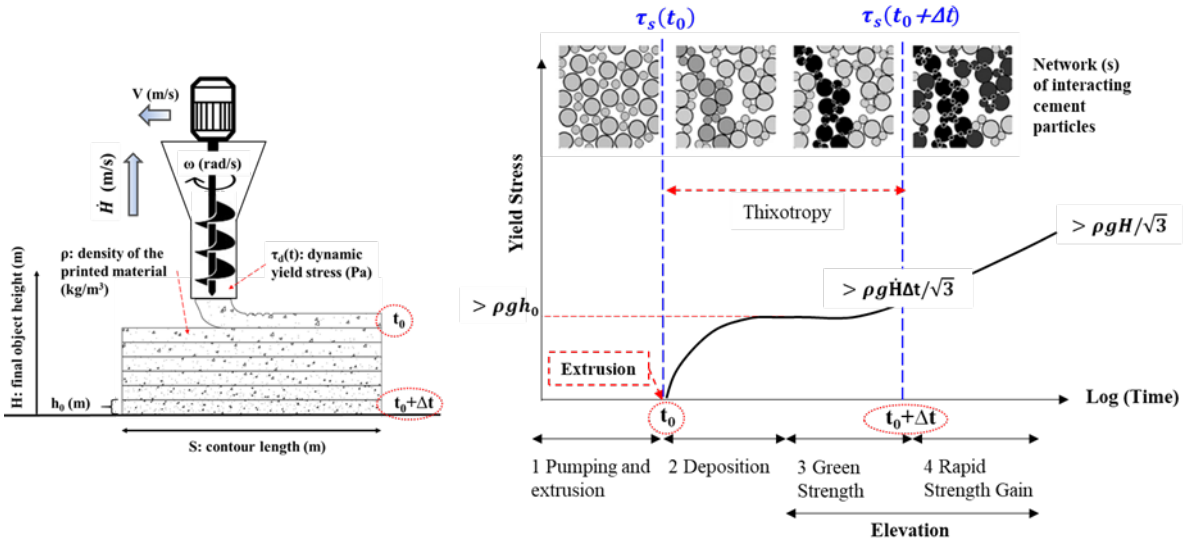

Figure 9. Printing settings and object geometry and their time dependency (Left). Interacting cement particles vs. yield stress evolution and its evolution over time (Right). Adapted from [57].

Mechanical Anisotropy in 3D Printed Concrete

The nature of the extrusion-based process, the layer build-up, and the lack of compaction [58] favor the presence of joints at the printing interfaces, which should exhibit a minimum bond strength to ensure a safe structural design. Also, cement-based materials are subjected to hydration and colloidal changes over time [14], making the fresh state properties variable during the extrusion process. As 3D printing technology expands, there is an increasing need for predicting how the manufacturing process affects the hardened mechanical properties of the 3D printed concrete [16,43,58,59]. Research studies reported on some of the printing factors that can potentially influence the hardened mechanical properties of the 3D printed concrete [43,60,61]. The printing interface between layers has been shown as a critical element that can impact structural performance [16,58,62–65]. The mechanical properties of

`

the 3D printed concrete at this interface can be weaker, inducing an anisotropic behavior generated by the predetermined planes or pathways for cracks to propagate.

The adhesion between two concrete layers at the interface has been reported to be governed by four main factors [66]: mechanical interaction, chemical bond, intermolecular forces, and surface forces. For conventional cast concrete, Hui-cai et al. [59] observed using Scanning Electron Microscopy (SEM) that the interface between two concretes cast at different times is composed of different microstructural phases. One of these phases is notably weaker than the other due to the relatively high content of calcium hydroxide crystals deposited at the interface. For 3D printing, the interfacial bond and consequently the mechanical behavior can be affected by material and manufacturing interdependent factors such as layer orientation [16,17,64,67–69], interlayer interval time [17,43,58,68], the height of the printing nozzle to the printing surface [17,58], rheology of the mix [53,70,71], and surface moisture content of the deposited concrete layer [18,58].

One of the main limitations of manufacturing is the difficulty of depositing the material with a certain quality standard while changing direction [72], especially at high printing speed. Other related aspects include the inertia of the extruded filament and the printing system, limitations of the printer itself, and the filament distortion due to the layer deposition and other robotic limitations [11,17,72–74]. Thus, a clear dependency relation is observed between the fresh material properties and the extrusion process. The dependency of the printing product quality and performance upon the printing process and settings selected is fundamental. The repeatability of a printing process using a different printing system, operator, or while printing at a different printing environment (temperature and humidity) is one of the main challenges for concrete 3D printing technology implementation. This also

`

points out to the importance of the role of the operator in terms of skill and training on the printing process and final product.

The interlayer interval time relates both printing and geometrical parameters with the material properties. It can be defined as the time between the deposition of two consecutive layers, and it has a considerable influence on the hardened properties of 3D printed concrete. This time gap must be long enough to ensure the stability of the extruded layer under the self-weight and the pressure of the layers above it. There is also a lower limit to ensure good interlayer adhesion [75]. Low adhesion will ultimately extrapolate to a weak hardened structure due to the presence of the so-called "cold joints" when the layer cycle-time is too long [11,16], especially for interval times longer than the initial setting time [58]. Nerella et al. [68] showed that the bond at the interface might be weakened due to carbonatation or shrinkage. The properties of these joints can evolve as the hydration process develops, becoming sufficiently strong with time [11]. Le et al. [16] studied the influence of the interlayer interval time on the hardened compressive, flexural, and tensile strength in the three principal directions. A mix composed of silica fume, fly ash, cement, sand, superplasticizer, retarders, and propylene fibers was analytically designed to do so. A decrease in the tensile strength while increasing the interval time was observed. Nerella et al. [19,68] extended this work by performing SEM observations, which showed clear interlayer interfaces at a microstructural level for long interval times.

From a rheological perspective, the low yield stress required for the material to be pumped and extruded opposes the deposed filament’s need to keep its shape [43]. As the mix is extruded and layers are placed, the vertical deformation due to the elastic behavior of the pseudo-solid material under the self-weight of the structure increases due to the deformation

`

of the substrate layers. For pressure-driven layer extrusion techniques (the layer height is lower than the nozzle size, pressing the filament against the previous one), this phenomenon reduces the pressure exerted by the nozzle between layers and influences interlayer adhesion [17]. This effect becomes increasingly significant as new layers are built since the distance between the nozzle and the material increases, and it can ultimately cause the filament to move laterally before being placed, causing instability (buckling) of the whole structure [43]. This phenomenon is relevant when printing tall structures [45,74]. Two approaches to address this problem have been studied: a real-time adjustment of the height of the nozzle while printing based on the real-time deformability of the structure [74], and the control of the structuration rate by using accelerators sprayed at the nozzle and reducing the printing speed (set on-demand solution) [65,75]. Roussel [53] introduced a set of rheological requirements for 3D printed concrete to prevent these problems.

Cold joints have also been associated with a limited intermixing of the layers at the interface [53,70,71]. The mix's ability to partially flow over the previous layer contrasts the need from the material to withstand the hydrostatic pressure exerted by the printing layers above it. The material capacity to build up an internal structure at rest is known as thixotropy, and it is essential for layered extrusion techniques. In this context, the structuration rate is understood as the rate by which the static yield stress increases with time. Researchers [53,70,71] reported that for distinct-layer casting, the structuration rate should be within an optimum range to prevent flow under the stresses generated by the process and to guarantee a partial flow of the deposited layer over the previous one. Open time is defined as the "*operability window*" in which the material retains its rheological properties (viscosity, yield stress, and thixotropy) within a range that makes the extrusion possible without compromising the

`

hardened properties of the final product [16,17,43,65,75]. Open time relates the rheological properties of the mix to the printing process through the mix design. The printing speed should be adjusted to be fast enough to ensure an appropriate layer-to-layer bond while maintaining a build-up rate that would be compatible with the structuration rate of the mix. Printing factors such as printing speed, layer thickness, and interlayer time need to be considered while designing the rheology of the mix. Wolfs et al. [54] developed a numerical model to predict the mechanical behavior of fresh 3D printed concrete from the deposition time and up to 90 minutes after deposition. The numerical failure criterion used was a time-dependent Mohr-Coulomb, and linear stress-strain behavior was considered until failure. More recently, researchers [18] have suggested that thixotropy could not be the main limiting factor for the interlayer strength of 3D printed concrete but rather the presence of a micrometer range thickness dried zone at the substrate layer. Wolfs et al. and Keita et al. [18,58] associated the layer interface strength for smooth surfaces with the superficial drying of the resting layer.

They studied how the surface moisture content would influence the bond strength in the interlayer zone. Keita et al. [18] detected reductions up to 50% for uncovered interfaces exposed a long time before printing. Wolfs et al. [58] examined the flexural tensile strength of 3D printed concrete samples for covered and uncovered specimens printed with interlayer interval times of 4 and 24 hours. A significant reduction in bond strength as a function of the time and humidity exposure was observed.

Finally, the bulk density of the 3D printed concrete is crucial to ensure adequate hardened mechanical properties. The printing path can have a significant influence on the density by a process called under-filling. The generation of millimetric-scale voids by under-filling was

`

first identified by Le et al. [16] and, more recently, reported by others [20]. This phenomenon is depicted in Figure 10.

(a) (b)

Figure 10. Linear voids between filaments (namely inter-filament voids) in (a) transverse and (b) side view.

The tool path, the printing system, and the rheological properties of the concrete mix remarkably influence density and, consequently, the hardened mechanical properties. Researchers have observed relatively high densities for 3D printed concrete specimens than in cast ones [16,17,20] for cases in which rheology and printing parameters were optimized. We suggest that the interdependence of factors affecting 3D printed concrete can be described by a 3D tetrahedral model, analogous to a silica tetrahedral, as presented in Figure 11. The material properties, the mix design, and the 3D printing process represent the tetrahedral base. The rheological properties and the green strength of 3D printed concrete are hidden at the center of the model, analogous to the Oxygen atom in the silica tetrahedral. Finally, the hardened concrete characteristics are placed at the top of the tetrahedral. We suggest this model can help to understand the factors affecting 3D printed concrete for successful design and simulation.

`

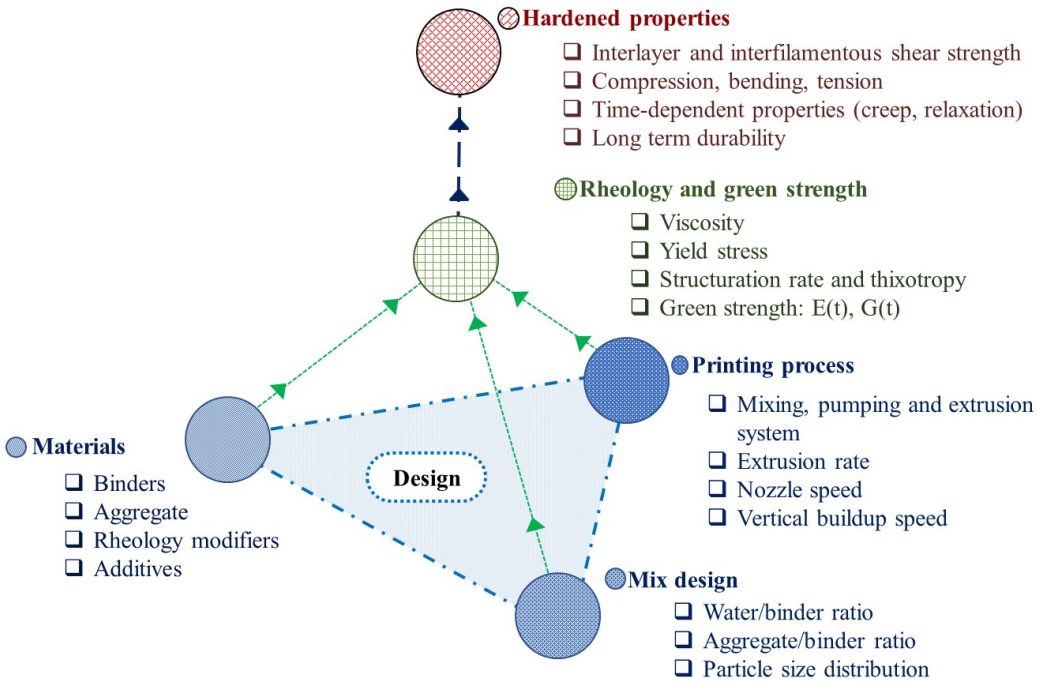

Figure 11. Tetrahedral model of 3D printed concrete, analogous to silica tetrahedral, showing interdependence among parameters affecting 3D concrete printing.

In this context, research [16–21] has tried to quantify the anisotropy that the printing process exerts on the hardened product. Research work [17–19] focused on the interlayer interface behavior for monofilament specimens. On the other hand, the behavior at the interface between filaments (interfilamentous) has not received that much research attention [16,21]. For bulk specimens, both interfaces can have a significant impact on the hardened mechanical performance. Higher macro-scale porosity, induced by the printing process, is prone to appear in both interfaces. Macro-scale porosity was reported as a critical factor in inducing an anisotropic behavior [19]. Researchers [16,20,21] show an anisotropic behavior induced by the printing process by performing compression testing in the three principal directions. Although compression testing is not an indicator of the interface strength, it can be used to indicate the overall anisotropy of a sample if three principal directions are

`

examined [19]. Most of the research did not show any statistically significant difference between the three directions [20,21] for a determined printing pattern, probably due to the small sample size (three samples per direction). Le et al. [16] tested the anisotropic behavior of a pre-determined infill pattern and concluded that the vertical direction was significantly stronger than the other two directions.

Polymer Concrete as an Alternative Material for 3D Printing

Concrete 3D printing commonly relies on the deposition of layered filaments of the material. Cement-based materials have been used for this application due to their ability to stay as pseudo-solid before hardening when their flow properties are properly designed [44]. Cement concrete has limitations in its tensile capacity, ductility, fatigue, and resistance to chemical exposure. To overcome these limitations, polymer concrete (PC) was developed in the 1970s for applications that require protection against aggressive environments [76,77], dynamic and cyclic loads [78], high ductility [78–80], and fatigue [81]. The main applications of PC in infrastructure include bridge deck, industrial overlays, waste-water pipes and containers, utility holes, underground communication and transmission line boxes, building façade panels, machine foundations, and other elements subjected to dynamic and cyclic loads [82,83]. Numerous PC applications are directed toward precast elements, making PC amenable for 3D printing technology.

This work focuses specifically on polymer concrete, denoted PC. PC is a composite material developed by mixing well-graded aggregate/fillers and a polymer resin that fully substitutes the cement binder. Other types of polymer concrete can be found elsewhere [84]. The polymer matrix and aggregate mix design enable engineering specific PC properties, potentially reducing the mix's cost [85]. PC offers numerous advantages over cement

`

concrete as an infrastructure material, such as low permeability, high ductility, chemical resistance, acceptable mechanical strength, and excellent bond with other materials [86]. On the other hand, PC needs to be carefully designed for field application by accounting for temperature effects and considering the time-dependent behavior of PC under sustained stresses [86].

The use of fillers to modify the rheological properties of polymers has been of paramount importance to enable innovative applications of polymers [85]. Research has also been performed to understand the effects of using different filler materials on PC's behavior. Fly ash [87–89] and silica fume [89] were investigated as potential fillers for PC and showed an increase in PC's mechanical strength and overall durability performance. The improvement of mechanical strength in PC incorporating silica-based pozzolanic fillers is not attributed to the pozzolanic reaction as in cement concrete but to the ability of those fillers to improve the packing fraction of the particles [90] and to form with the fine and coarse aggregate a well-graded system of particles with reduced overall porosity [91]. Fly ash and silica fume are often used due to their wide availability and proven to provide PC with improved workability, high strength [92,93], good thermal stability [94–96], improved fire resistance [97], good electrical conductivity [96,98], and shielding features [99]. The addition of fly ash was also proven to lead to better mechanical performance than silica fume [89].

Engineering the rheology of 3D printed concrete is critical to balance the hardened state properties while maintaining good processability of the material for pumping and extrusion. Rheology is also essential to predict material response during the printing process. Rheological properties for concentrated suspensions of particles in a low viscosity matrix

have been widely investigated [100–106]. Figure 12 shows a schematic representation of the different rheological models used to describe polymer and polymer concrete (PC).

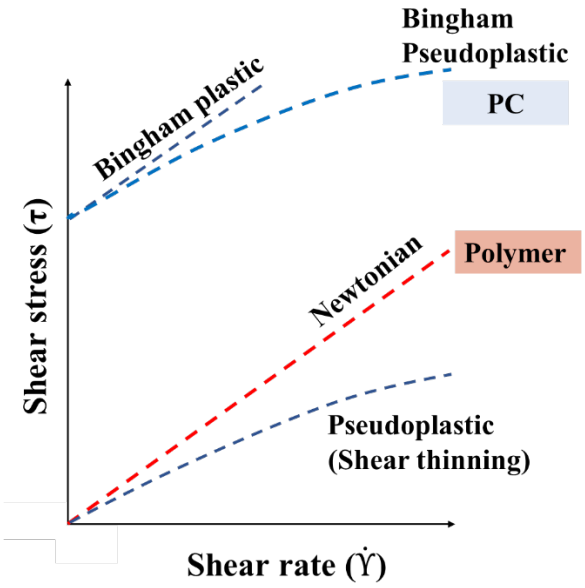

Figure 12. Schematic representation of the rheological behavior of polymer and PC.

Polymers usually do not display initial shear stress (required to start the flow). The relation between shear stress and shear rate for polymers can be linear (Newtonian) or non-linear (pseudoplastic). The pseudoplastic model describes a reduction in the viscosity (coefficient between shear stress and shear rate) over time. This is identified in the literature as shear-thinning behavior [100,101,104]. For PC, on the other hand, initial shear stress is required for the material to flow (Figure 12). The Bingham models describe this. If the material displays a constant viscosity as the shear rate increases, it is called Bingham plastic. If the material experiences a shear-thinning behavior, the material is described by a Bingham pseudoplastic. The properties of both the particles and the matrix and their interaction influence the flow properties of PC. The main factors affecting the rheological properties of PC are schematically summarized and illustrated in Figure 13**.** The figure depicts that the rheological properties of PC are a function of the interaction between the particles and the matrix, the

`

aggregate packing fraction, which depends on the particle size distribution and shape of the particles. The type of polymer also influences the rheology of the PC system through the viscosity evolution over time. The rate of polymerization controls the polymer viscosity change. The polymer matrix surrounds the inert materials that are dispersed without significantly affecting the molecular structure of the polymer [106]. By controlling the aggregate particle packing fraction, the properties of the fillers, and the rate of polymerization, PC rheology can be engineered.

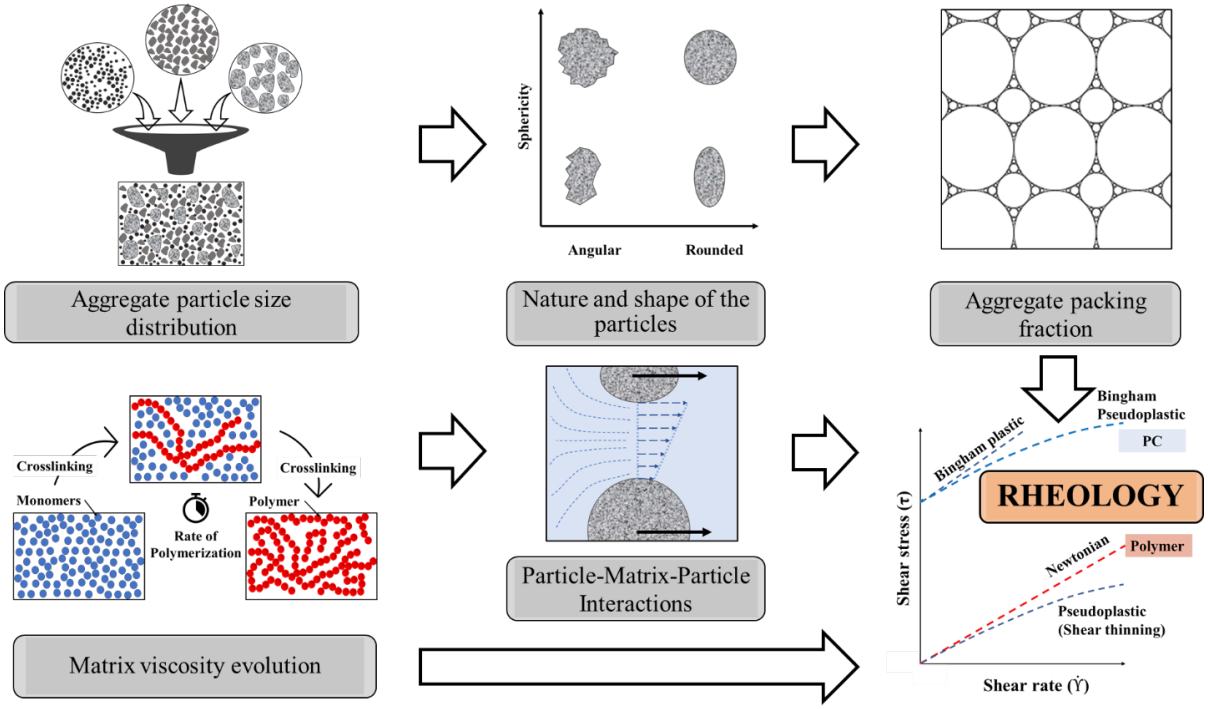

Figure 13. Leading factors affecting the rheology of PC.

The composite PC fluid comprising polymer and aggregate behaves as a non-Newtonian fluid that does not flow unless the applied stress (τ) exceeds minimum static yield stress, τ_s and then the relation between shear stress and shear strain ($\dot{\gamma}$) is non-linear (*pseudoplastic*). Figure 12 shows the rheological behavior of the PC as a Bingham pseudoplastic material. PC thus shows a dualistic rheological character. When the microstructure is undisturbed and well

`

connected (material at rest), it behaves as solid when the stress applied is smaller than the static yield stress, keeping its original shape while moving like a viscous liquid when shear stress above the static yield stress is maintained. Once the material has been disturbed (pre-sheared at higher shear stress than the static yield stress), the minimum stress to sustain or terminate the flow of the material is defined as the dynamic yield stress. This characteristic behavior of PC is crucial for additive manufacturing since concrete is shaped without a traditional formwork. PC also shows a time-dependent behavior called thixotropy, meaning that PC resistance to flow grows as the time at rest increases. Thixotropic materials, when at rest, develop intermolecular forces that increase the fluid's viscosity, also known as flocculation. The thixotropy nature of PC is represented by its ability to build up an internal structure at rest, which is another crucial feature for 3D printing applications [51]. For the material to flow, considerable external energy is required to break these binding forces. After deposition, when at rest, PC shows initial static yield stress and static shear strain (τ_{s0} and γ_{s0}). If the material is kept at rest, those parameters will change with time. The static shear stress and the elastic shear modulus (G) increase, while the static shear strain decreases with time. The material then becomes stronger and stiffer compared with its characteristics at deposition time [53].

The time-dependent rheological properties of PC are closely related to the printing process. The main factors relating to the material rheological properties with the 3D printing variables are illustrated in Figure 14**.** The rate at which the static yield stress increases with time is usually linear and defined in the literature as structuration rate A_{thix} (Pa/s). This rate is attributed to the thixotropic nature of the PC (Figure 14). Although the structuration rate is a material property, it strongly affects the 3D printing process. As depicted in Figure 14, the

`

required structuration rate is expected to scale as 3D printing variables such as contour length (S), the layer height (h_0), the printing speed (V), and the vertical build-up rate ($\dot{H}$) change. The static yield stress (τ_s) at a given time after deposition ($t_0 + \Delta t$), assuming a linear (constant rate) increase, can be written as:

Equation 2. Static yield stress at a given time after deposition ($t_0 + \Delta t$)

$$\tau_s(t_0 + \Delta t) = \tau_s(t_0) + A_{thix}\Delta t \quad \text{(Equation 2)}$$

It must be noted that assuming a constant structuration rate (linear evolution of the static yield stress) does not seem to characterize all materials [52].

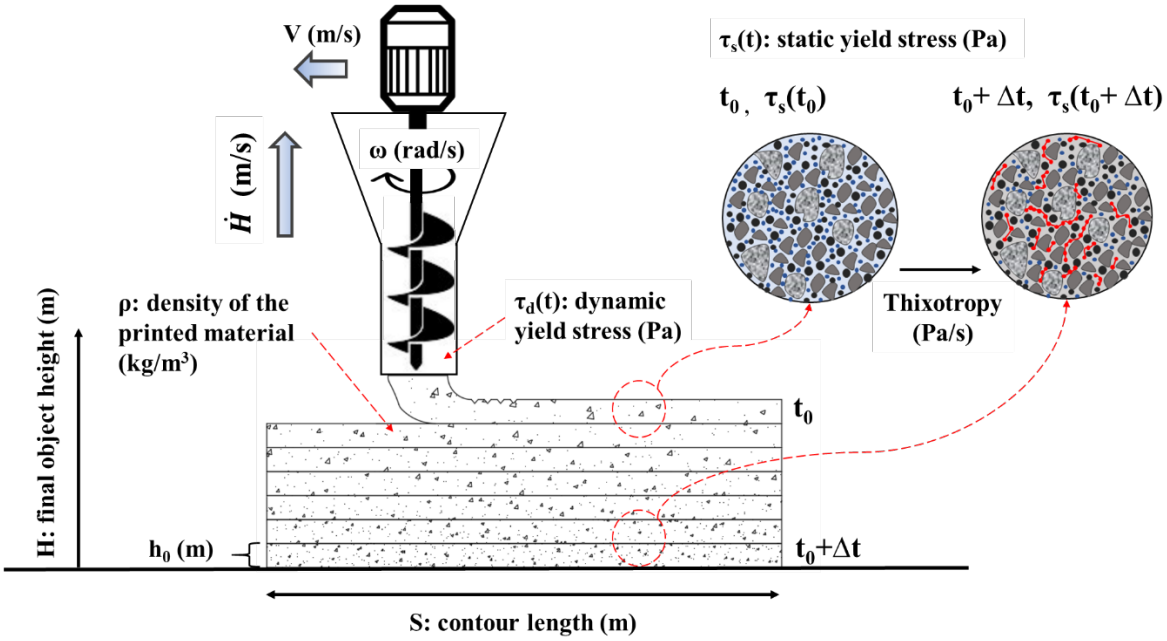

Figure 14. Relationship between rheological properties and 3D printing variables in PC.

After deposition, the stresses at the first layer of material must be limited so that the printed layers remain at a solid state preventing failure. The gravitational induced extensional stresses at the bottom layer assuming pure elongational flow [45,107] can be quantified as $\rho gH/\sqrt{3}$ where ρ is the density of the printed material, as shown in Figure 14**.** This stress needs to be kept below the static yield stress, also known as green strength $\tau_s(t_0 + \Delta t)$

`

(Equation 2) at any given time to prevent the collapse of the structure. Then, the equilibrium equation for the bottom layer at a given time after deposition ($t_0 + \Delta t$) can be rewritten as:

Equation 3. Static yield stress equilibrium equation for the bottom layer at a given time after deposition ($t_0 + \Delta t$).

$$\tau_s(t_0) + A_{thix}\Delta t = \rho g H/\sqrt{3} \quad \text{(Equation 3)}$$

Leading to the condition:

Equation 4. Structuration rate equilibrium criteria.

$$A_{thix} > \dot{H}(\rho g/\sqrt{3} - \tau_s(t_0)/H) \quad \text{(Equation 4)}$$

It is important to note how the build-up (rising) speed ($\dot{H}$) is dependent on the geometry of the printed object (contour length, *S*) and on printing parameters such as printing speed (*V*), layer height (h_0). Equation 4 relates the rheological properties with the 3D printing variables (Figure 14) and ultimately leads to the stability of the printing object (also referred to as green strength). The required structuration rate is expected to scale with the various object length scales and extrusion length scales of the process, and, although being a material requirement, it is entirely dependent on the process. It is important to note that as the structure height increases, stability issues due to increased slenderness ratio and potential buckling might arise. This issue is not considered in Equation 4 but might be considered by conducting finite element modeling of the printing process [54].

The dynamic yield stress (τ_d), as depicted in Figure 14, is related to the integrity of the printed filament (extruded at a rotational rate ω). It can be observed that the relation between the mix design and the rheology is critical to achieving a satisfactory 3D printed product. By understanding the rheological behavior of PC and how it can be tuned by altering the mix design, satisfactory fresh and harden mechanical properties can be achieved.

`

The hardened properties of PC depend upon many factors such as the type and content of the polymer resin, composition and particle size distribution of aggregates and fillers, the aggregate to polymer ratio, curing temperature, manufacturing process, and loading rate [89,108,109]. The compressive strength of PC incorporating different polymer resins was found to be improved when the polymer matrix volume fraction is less than 20% [108]. However, a balance needs to be made in the PC mix design to achieve acceptable rheological and mechanical properties. Optimal conventional (i.e., not for 3D printing) PC mixtures with good workability require a polymer matrix volume fraction higher than the 20% mentioned above. The size distribution and surface area of the aggregate used in the mix also greatly influence the required polymer resin content. Some researchers [110] indicated that Fuller's aggregate gradation could be used to lead to a PC with high compressive strength. The optimum polymer resin content will increase when fillers with a high surface area are used [111–113]. The printing path and the rheology of PC (dependent on the mix design) can significantly influence the bulk density of the hardened product by a process called under-filling [16] as depicted in Figure 10. The bulk density of the 3D printed concrete primarily affects its mechanical properties [114].

Reinforcement of 3D Printed Concrete Structures

Concrete as a construction material has some inherent limitations due to its low tensile strength capacity and ductility for some applications. Tensile strength for most concrete mixes is in the 10% of the compressive strength range, and most of the time, it is neglected in design. This limitation is overcome by implementing tensile steel reinforcement. Typical reinforcement techniques for casting concrete structures can be classified as internal or external, active or passive, and metallic or non-metallic [115], being the most common

`

internal, passive, and metallic reinforcement. Also, metallic reinforcement systems are prone to corrosion exposure resulting in a degradation of the structure. Fiber reinforcement has also been used for reinforcing concrete but with limitations regarding strength and ductility. Installation of internal, passive metallic reinforcement is typically done by placing the reinforcement grids in the mold that is then cast. As it is cast, the material flows between the reinforcement, and it is vibrated to ensure proper adhesion to the reinforcement. Reinforcement in traditional concrete design is required to provide structural capacity and ensure that no brittle failure, cracks or excessive deformations, or lack of ductility will happen. For this reason, a minimum amount of reinforcement is typically included. The reinforcement configurations and procedures traditionally used in construction are not amenable for additive manufacturing techniques. Consequently, there is the need to change the status quo in terms of reinforcement for 3D printing. Efforts to incorporate the traditional reinforcement techniques into concrete 3D printing have been made [115]. Nonetheless, they might not be profitable in most cases but detrimental to the technology from an economic and efficiency perspective.

Reinforcement integration into 3D printing technology is undergoing many challenges due to inference between the in-plane layer by layer manufacturing process and the presence of vertical reinforcement [116]. Although the knowledge and interest in extrusion 3DcP technologies are rapidly progressing, there is still an overreaching limitation of effectively incorporating reinforcement in the manufacturing process [117]. The scarce adaptability of these traditional reinforcement techniques with the AM process and the design of geometrically complex forms make alternative reinforcement techniques desirable

`

alternatives [116]. To make 3DCP a feasible and practical alternative to conventionally cast concrete, efficient methods of incorporating reinforcement must be developed.

The recent developments in robotics, digital design, material engineering, and modeling have introduced innovative construction methods [115]. These advances present much potential to increase design freedom and the degree of automation in construction. Nonetheless, these new technologies (including concrete 3D printing) require new reinforcement systems and configurations amenable to the manufacturing techniques.

There is currently an emphasis on studying different reinforcement methods and technologies compatible with concrete additive manufacturing [115,117]. Most of these methods reinforce the interfilamentous plane, but few have studied the reinforcement in the printing direction (interlayer plane). Based on the classifications of Marchment et al. [117] and Asprone et al. [115], most reinforcement techniques can be classified into one of the following groups:

1. Pre-installed reinforcement method

There have been precedents of using pre-installed vertical and horizontal reinforcement on a large scale by HuaShang Tengda Ltd. A robotic 3D printer with two nozzles would print the material on both sides of the vertical reinforcement or over the horizontal one [117], as depicted in Figure 16 (b). This method requires pre-building the reinforcement mesh structure, placing it, and keeping it in place before and while printing. Also, design is limited to the presence of just vertical or horizontal reinforcement.

2. Post-installed reinforcement methods

Typically, large-scale 3D printed structures incorporate the reinforcement after the printing is performed [117]. To do this, use a 3D printed shell structure as a “structural formwork” to then include the reinforcement and cast regular concrete inside, as depicted in Figure 16 (a).

`

Some companies [61] and researchers have implemented and investigated this method [29,118]. Other approaches such as placing reinforcement after printing grouting it to the printed structure by leaving holes in the printed structure [23] or fixing truss-like external reinforcement structures to the printed element [116], as shown in Figure 16 (c), have been studied. These methods show great potential, but they are still very labor-intensive and hard to automize.

There are also cases of structures with post-installed active reinforcement methods (post-tensioned reinforcement). Some 3D printed pedestrian bridges have been designed with these methods [119,120]. Some methods of making for the production of 3D printed segmental concrete structures have been patented by Reda Taha et al. [121]. Details of the patented work are included in Figure 15. This issue is not explicitly covered in this thesis.

3. Short fiber reinforcement method

Short fiber inclusion in the mix design to reinforce the 3D printed mix has been widely studied by researchers [69,107,122–126]. The addition of these fibers in the mix has proven to improve the material's tensile strength but not significantly improve the toughness and ductility. Also, these fibers only reinforce in the layer plane and not in the interfilamentous plane. An SEM image of a 3D printed mix including polyethylene fibers is depicted in Figure 16 (d).

4. In-layer direction reinforcement

Numerous researchers have investigated the use of wire reinforcement systems embedded in the material filament since its conception by Khoshnevis [34]. Khoshnevis investigated the use of a steel coil. More recently, researchers have investigated the use of high tensile steel cables embedded in the filament to provide confinement [127,128], as depicted in Figure 16

(e). Furthermore, the printer head was developed to embed a single or multi-strand cable and even a chain [129,130]. This method was proven superior to the inclusion of short fibers in the mix, but it still faces the challenge of reinforcing the interfilamentous interface.

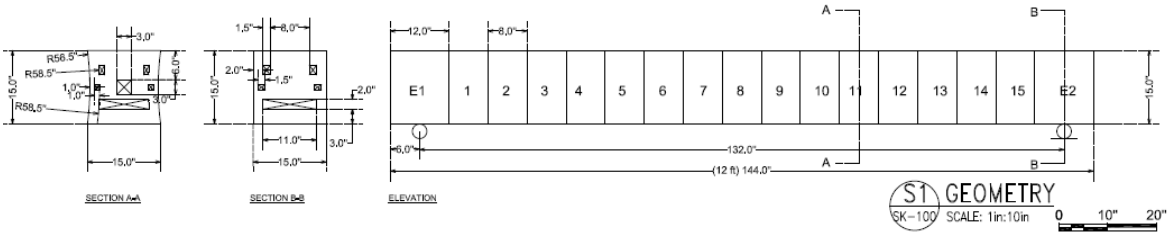

(a)

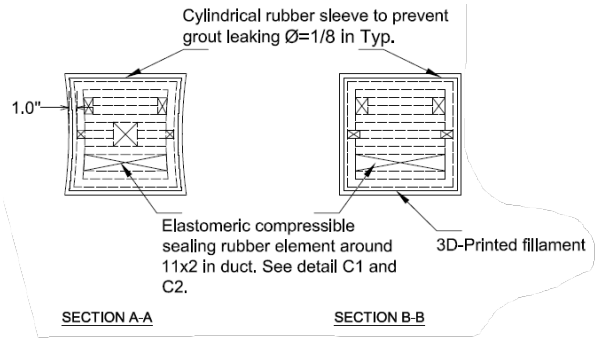

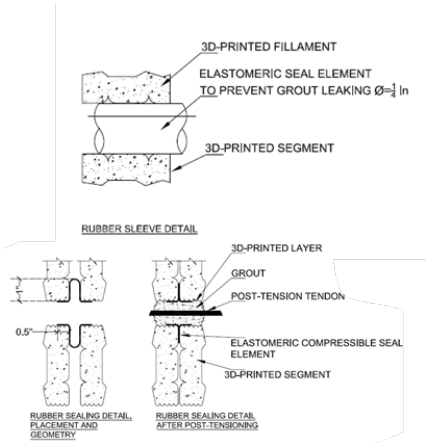

(b) **(c)**

Figure 15. Methods of making for 3D printed segmental concrete structures. Adapted from [121] (a) Elevation and sectional view of the geometry. (b) Sectional view of the printing path. (c) Details for the implementation of the post-tensioning reinforcement and grouting.

`

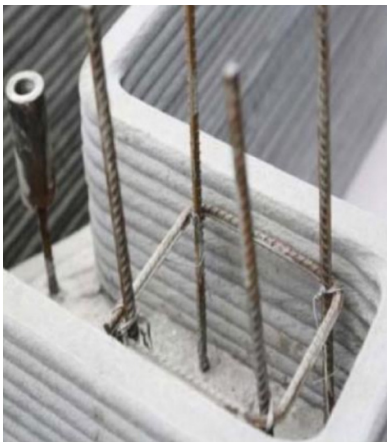

(a)

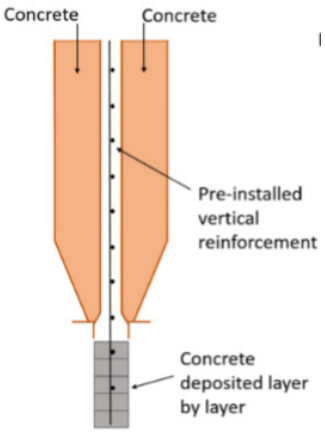

(b)

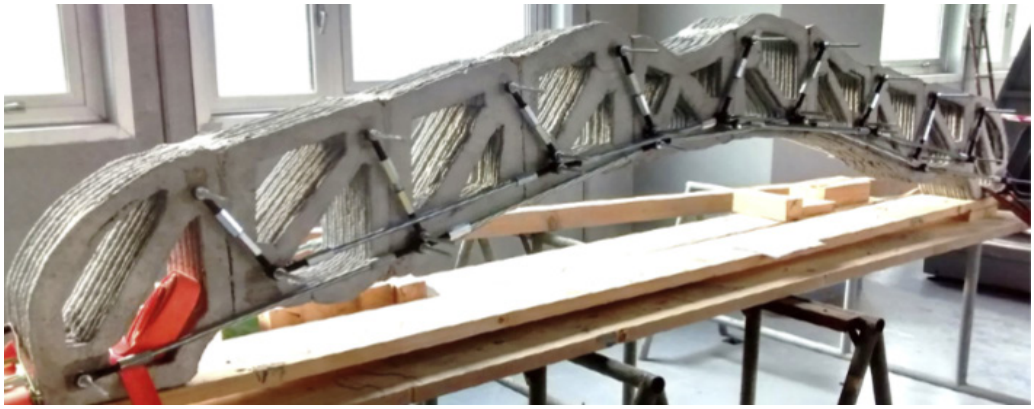

(c)

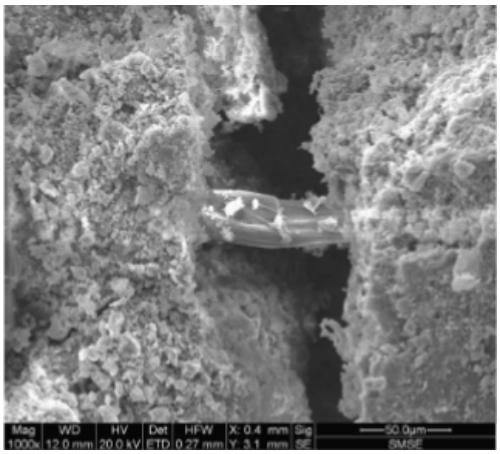

(d)

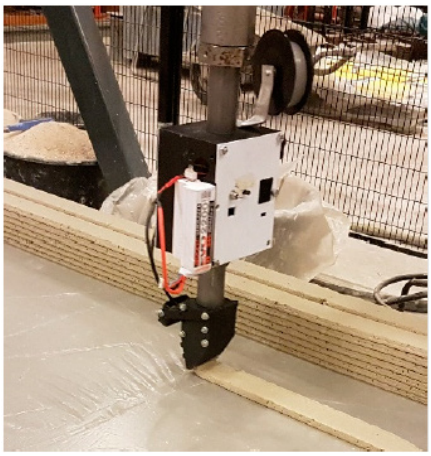

(e)

Figure 16. Reinforcement techniques for 3D printed concrete. (a) Passive post-installed reinforcement method in a concrete 3D printed formwork. Extracted from http://www.winsun3d.com. (b) Schematic of a pre-installed mesh reinforcement method. Extracted from [117]. (c) Active post-installed external reinforcement method. Extracted

`

from [116]. (d) SEM image of short polyethylene fiber reinforcement at a micro-scale. Extracted from [131]. (e) Active reinforcement for filament embedded cable reinforcement. Extracted from [128].

Textile Reinforcement of Cement Composites

Textile reinforced concrete (TRC) is a cementitious composite that has been recently introduced to civil infrastructure to reinforce precast elements and strengthen deteriorated structures due to its lightweight, durability, design and installation flexibility, and in- and out-of-plane structural performance [132–137]. Typically, TRC is created by incorporating high-performance textile reinforcement made of continuous multi-filament yarns (e.g., glass, polypropylene, polyamides) into a matrix comprised of cement as a binder and small-size, well-distributed aggregate [138,139]. Planar (2D) or spatial (3D) textile reinforcement can be used in TRC depending on the load application [134–136,140]. Potential applications for TRC include architecture façade, noise/water protection panels, sandwich walls, load-bearing shell structures, and storage units (e.g., tanks and silos) [132,141], and for the strengthening of existing reinforced concrete structures [137,142–146]. Studies showed that TRC could replace fiber-reinforced polymer (FRP) composites for flexural and shear retrofitting with similar capacity enhancement but improved durability [147].

Despite its unique structural performance, research has unveiled a few challenges related to the failure behavior of TRC structural elements. Specifically, the potential for premature debonding between the textile yarns and the cement matrix at low strains. Organic coats were suggested to improve the bond behavior between the fibers and the mortar [148]. Previous research showed that such early debonding could be attributed to the cementitious matrix's improper impregnation of the fiber fabrics. Microscopic images showed that the degree of

`

fiber impregnation varies within fiber filaments, with outer (sleeve) filaments being fully impregnated and fiber impregnation decrease toward the central (core) fibers [149,150]. The cement slurry's high viscosity contributes to the cement matrix's low penetration into narrow spaces in the textile yarn. However, stresses can still transfer to the core fiber layers via frictional contact with the adjacent outer fiber layers [151,152]. When TRC is subjected to high loading rates (e.g., impact or dynamic), further debonding between the reinforcement textile layers and the cement matrix occurs. Debonding may lower the load-carrying capacity and ductility, potentially altering the failure mode of the TRC structure [152].

Several types of textile reinforcement materials have been used in TRC, including polypropylene, alkali-resistant glass, carbon, and basalt. Basalt fibers can be produced from natural resources (volcanic rocks); they require low energy for manufacture, are recyclable, and have high performance while relatively inexpensive compared with other types of fibers [153]. Due to these advantages, basalt fibers have positioned themselves as a promising material for textile reinforcement and fibers in cement composites.

On the other hand, polymer concrete (PC) is a composite material developed by combining a polymer resin that fully substitutes the cement as a binder and well-graded aggregate particles as a filler [154]. Polymers such as epoxy, polyester, vinyl ester, and methyl methacrylate (MMA) are commonly used in the construction industry [84]. The PC mixture typically contains an initiator to promote polymerization and to control the hardening time. Combining a polymer matrix and aggregate enables researchers and contractors to engineer specific desired properties due to its physicochemical properties such as low permeability, high ductility, high durability, chemical resistance, and good mechanical strength [24, 25]. Aggregate type is chosen to achieve desired characteristics such as high strength [92,93,156],

`

thermal stability [94–96,157], fire resistance [97,158,159], electrical conductivity [95,96,98], or electromagnetic shielding [99]. Polymers are also known for their significantly high bond strength to many surfaces compared with cement. PC is, therefore, favorable when a strong bond to the reinforcement is required.

`

Chapter 3. Examining the Significance of Infill Printing Pattern on the Anisotropy of 3D Printed Concrete

This study examines how the combined presence of both interfaces within the same bulk specimen can affect the overall anisotropic mechanical behavior of the specimen. Besides, the potential effect of the printing infill pattern on the mechanical properties of bulk specimens and the anisotropy remains uninvestigated. This work examines the significance of infill printing patterns on the hardened properties (density and compressive strength) of 3D printed concrete. Concrete specimens were printed with three different infill patterns, and the performance of those specimens was compared with conventionally cast concrete ones. The anisotropy of the 3D printed concrete associated with the infill printing patterns and testing directions was analyzed and reported herein through compression testing.

The significance of infill patterns on the anisotropic properties of 3D printable concrete and how those mechanical properties compare to conventionally cast concrete was investigated. The rheological properties of the concrete mix were characterized, and the compressive and interlayer bond strengths of the 3D printed concrete were determined experimentally. The experimental results show that there is a directional dependence on all the printing patterns. However, no significant difference in the mechanical properties was observed or attributed to the printing patterns. The results show that the 3D printed concrete specimens show higher compressive strength than conventional cast concrete for some testing directions due to the compactness associated with the printing process

`

Experimental Methods

Materials and Mix Design

A high-performance 3D printable concrete mix was designed. Fresh-state properties such as rheology, extrudability, and buildability were considered. High compressive strength in the hardened state was addressed by selecting a high content of pozzolanic materials with respect to aggregate [43]. A well-graded aggregate with a maximum nominal aggregate size of 2.36 mm and a predominant range comprised of between #20 to #50 (0.8-0.3 mm) was used. Figure 17 shows the particle size distribution of the aggregate used in producing 3D printed concrete. This maximum aggregate size ensures proper printing resolution for the 20 mm nozzle diameter used in printing.

Type I-II Portland cement, type-F fly ash, and silica fume (Rheomac SF 100, BASF group) were used. The binder (cement, silica fume, and fly ash) to aggregate ratio and the pozzolanic material's content (cement and silica fume) to the total binder weight were adopted based on the recommendations by Le et al. [43]. The mix also included a polycarboxylate-based high-range water-reducer (HRWR) admixture (MasterGlenium 3030, BASF group). This HRWR meets ASTM C494/C 494M requirements for Type F, high-range water-reducing, admixtures [160]. It was added in a dosage of 1.05% to the binder by weight. Previous researchers showed that such content is adequate to reduce the water-binder ratio and achieve satisfactory rheological properties [43,161]. The water to binder ratio was kept at 0.28. Concrete mix design proportions used in the 3D printed concrete are presented in Table 1.

.

`

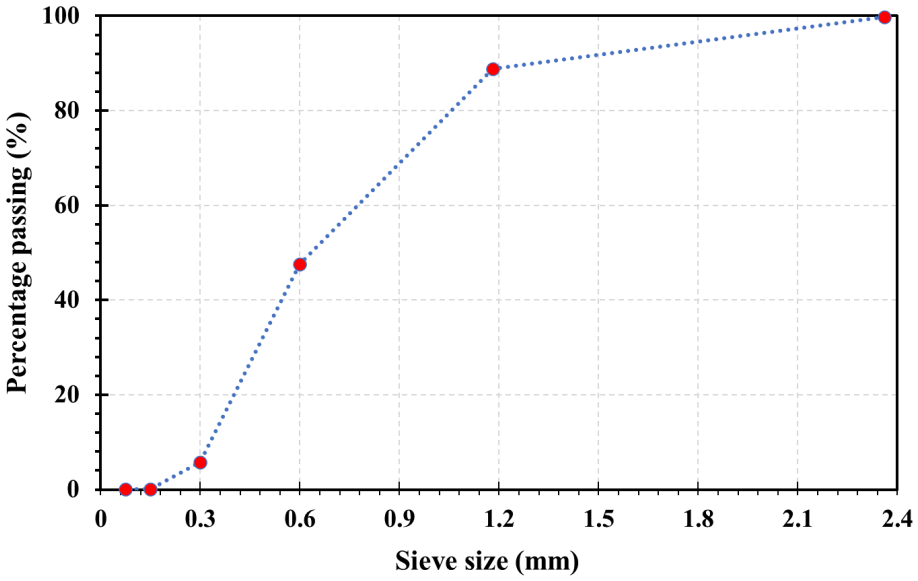

Figure 17. Particle size distribution of the aggregate used to produce 3D printed concrete.

Table 1. Concrete mix proportions used for 3D printed concrete.

Component	Quantity (kg/m^3)
Cement	546
Fly ash	156
Silica Fume	78
Sand	1171
Water	219
HRWR	8.20

Mixing and Pumping

A shear mixer was used to mix the concrete. Binder materials (cement, silica fume, and fly ash) were added together to the mixer. Then, a mix of water and HRWR agent was added and mixed for 30 seconds. The paste was continuously mixed for an additional 30 seconds. The aggregate was then added and mixed for 2 minutes. The concrete was pumped using a

`

positive displacement pump to the tool head. The concrete was extruded (and therefore sheared) at the nozzle before deposition using a helicoidal extruder.

Printing and Curing 3D Printed Concrete Specimens

A gantry robot 3D printer with 3 degrees of freedom and a printable area of 2x2x2 m was used. Cube specimens of 160x160x160 mm were printed by using a 20 mm diameter nozzle, 10 mm layer height, and 50 mm/s linear printing speed. These printing settings were chosen based on the rheological properties of the mix, the printing system and work reported by other researchers [21,161]. The temperature during the printing process was kept at 23±2℃. The specimens were cut after curing, using a wet brick saw, into 120x120x120 mm cubes to obtain surfaces smooth enough for mechanical testing. The gantry robot, extrusion of the cubes, and the 3D printed concrete cubic specimens are shown in Figure 18.

(a) **(b)** **(c)**

Figure 18. (a) 3D printer gantry robot. (b) Nozzle, extruding system, and detail of the printing process. (c) 3D printed concrete cubic specimen after surface preparation in the X and Y planes (all planes were cut).

The extrusion rate represents the rotational speed of the helicoidal extruder that pushes the material through the nozzle. In order to print the cubic specimens, it was adapted to the

`

rheological properties of the mix at each time, varying from 0.6 rad/s to 2.2 rad/s (2.88 L/min to 10.68 L/min). The extrusion rate is also related to the printing speed. For a given printing speed (in the layer plane), the extrusion rate should be accounted for so that the filament is not over extruded or under extruded (causing filament interruption). All concrete specimens were 3D printed in 16 layers following three different infill printing patterns (depicted in Figure 19 c,d,e). A pictorial description of the infill printing patterns (for the 12 layers tested) is shown in Figure 19a.

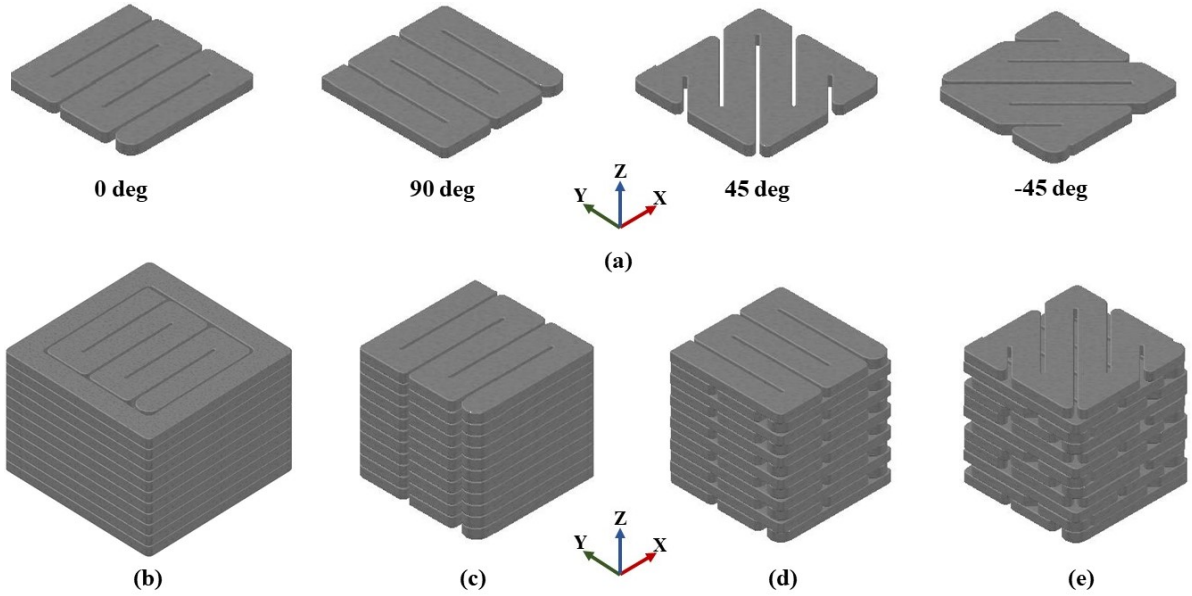

Figure 19. Schematic description of the printing patterns. (a) Layer orientations. (b) [0]12 specimen before cutting the perimeter. (c) $[0]_{12}$ specimen after cutting. (d) $[0,90]_6$ specimen after cutting. (e) $[0,45,90\text{-}45]_3$ specimen after cutting.

An outline perimeter (Figure 19b) was printed first, followed by the core. The outline perimeter was cut before testing, as shown in Figure 19c, d, and e, so that the surfaces would be smooth enough for mechanical testing. The nomenclature used to describe the infill printing patterns is as follows $[\phi_1, \phi_{2...}, \phi_i]_n$, where ϕ_1, $\phi_{2,...}$, ϕ_i are the different layer

`

orientations for one sequence (as shown in Figure 19a) and "n" is the number of times this sequence is repeated vertically. For instance, $[0,90]_6$ represents a concrete specimen with alternated 0- and 90-degree layers printed six times in the Z direction. Five reference specimens were conventionally cast using the same concrete mix and standard 150x150x150mm cubic molds per BS EN 12390-3:2019 [162]. The casting and consolidation protocols were performed following ASTM C192/C192M [163]. Consolidation of the cast cubes was accomplished by casting three layers of equal depth and tamping 25 times per layer with a 16mm diameter rod [163]. The specimens were cut after curing, using a wet brick saw, into 120x120x120 mm cubes.

A total of 50 cubes were printed. Fifteen cubes were printed following each pattern (shown in Figure 19), and then five specimens were selected for testing in the X, Y, and Z directions, respectively, forming a matrix of 45 3D printed concrete specimens. All the specimens were cured in standard curing water at 70°C for seven days to expedite the curing process according to the maturity method as per ASTM C1520/C1074-19 [164].

Rheological Measurements, Initial Setting Time, and Slump

Rheology measurements were performed using a Brookfield RST soft solid tester rotational rheometer (Figure 20). The shear vane spindle had a diameter of 20 mm and a length of 40 mm [165,166]. For this spindle geometry, the range of the apparatus in terms of shear stress is 5.2 Pa to 3.4 kPa. The test performed is a hysteresis technique introduced by Weltmann and Green [167]. It is widely used for thixotropic particulate suspensions, including cementitious mixes [21,161,168]. The shear rate was ramped up from $0s^{-1}$ to 100 s^{-1} in 60 s and then down from 100 s^{-1} to 0 s^{-1} in 60 s, as shown in Figure 20. The samples were not pre-sheared prior to the test so that the static yield stress could be quantified. The material was

`

mixed, as indicated in section 2.2, and then collected from the mixer. Concrete samples were tested at different resting times (0,15,30 and 45 min). Each sample was left undisturbed until testing time and tested only once to prevent the material from having ashear history (besides the mixing). Four samples were tested at each time, leading to a total of 16 samples. Time "0" was considered immediately after the mixing process was concluded. The temperature during the test was kept at 23±2℃. A visco-plastic Bingham material model was assumed. This means the fresh material will only flow when submitted to stresses higher than its static yield stress. Once it does, the relationship between the shear stress and the shear rate will be linear through a constant called plastic viscosity.

Using the standard test method for hydraulic cement by Vicat Needle ASTM C191−18a [169], setting time testing was determined using the standard test method for hydraulic cement. The slump at time zero was measured using the ASTM C143-15a [170] with a cone height of 50.8 mm. Both tests were performed after mixing the material, as specified in section 2.2.

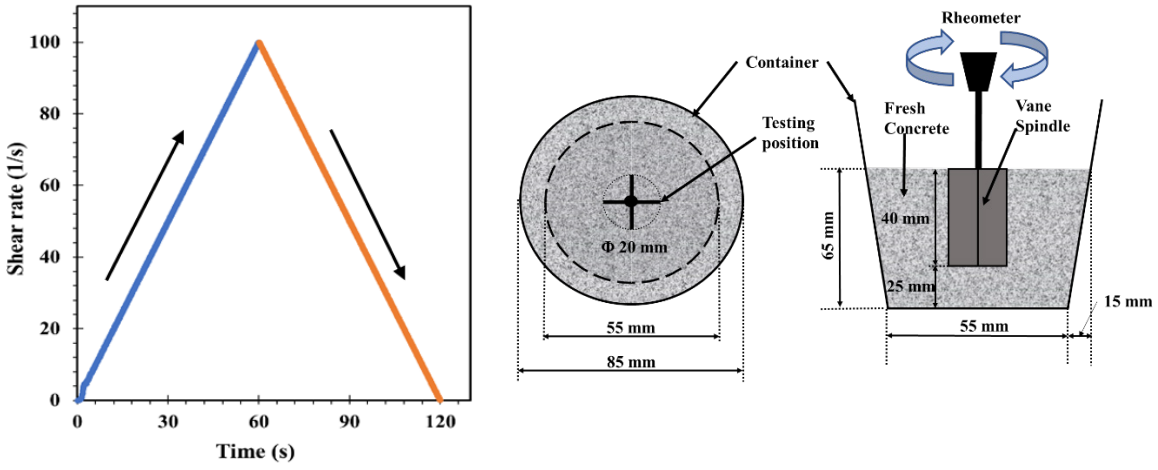

(a) **(b)**

Figure 20. Rheology test (a) Hysteresis loop test adopted from[21,161]. (b) Shear vane test with measurement positions modified from [43].

`

Buildability Test

The buildability test is used to determine the number of filaments that can be stacked on top of each other without having any collapse of the printed structure. The buildability test method used here was reported in the literature [11]. A 20 mm circular nozzle was used with a layer height of 10 mm. The number of adjacent filaments was changed from 1 to 3, and the vertical number of stacked layers up to failure was recorded, as shown in Figure 21. The test was performed at a constant extrusion rate of 1 rad/s (4.86 L/min). The filament length was 300 mm, and the printing speed 50 mm/s.

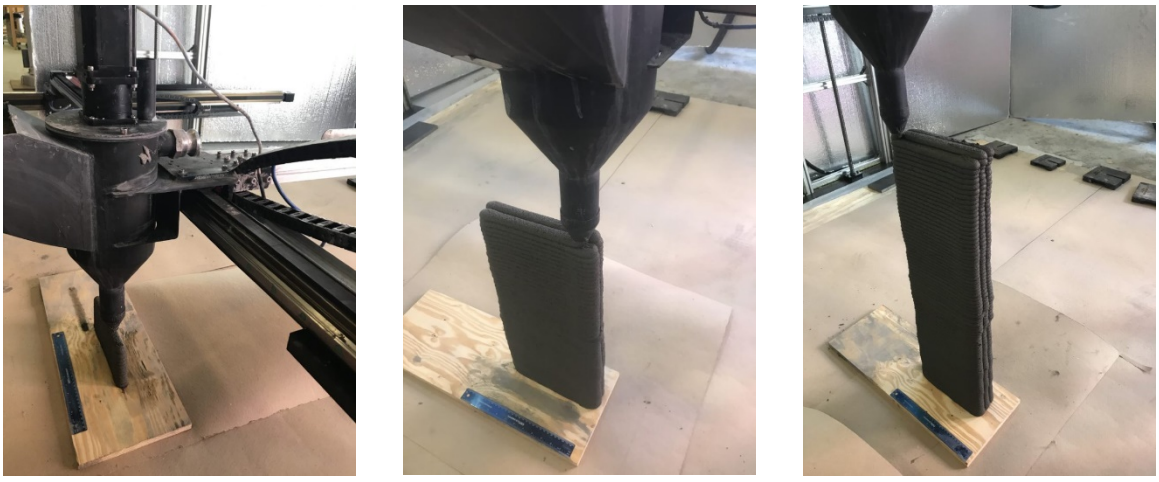

(a) **(b)** **(c)**

Figure 21. Buildability test: (a) one-layer test, (b) two-layer test, and (c) three-layer test.

Compression and Shear Tests

The compression test of the 3D printed concrete cubes was performed using a Tinius Olsen universal testing machine with a resolution of 1 lbf (4,45 N) and a maximum capacity of 400 Kip (1779 kN). Five specimens were tested for each direction and printing pattern (a total of 45 3D printed concrete specimens and five regularly cast ones). A displacement rate of

`

1mm/min was used during the test. Short beam shear tests were performed parallel to the interlayer and interfilamentous planes to determine whether failure would occur as a typical shear failure (Figure 22c) or as an interface failure (Figure 22d). Shear strength between both interfaces (interlayer and interfilamentous) was compared to conventionally cast samples. The specimen extraction procedure and the test setup are shown in Figure 22. The specimen's dimensions were 15 mm wide x 30 mm span x 20mm depth. The low span to depth ratio (less than 4:1 as specified per ASTM D 2344 [171]) would ensure shear failure. Three specimens were tested for each configuration. Specimens were extracted from different locations of the same large cube. The test was performed using a Bionix universal testing machine with a resolution of 1N and a range of 1N-25KN. A displacement rate of 0.5mm/min was used during the test.

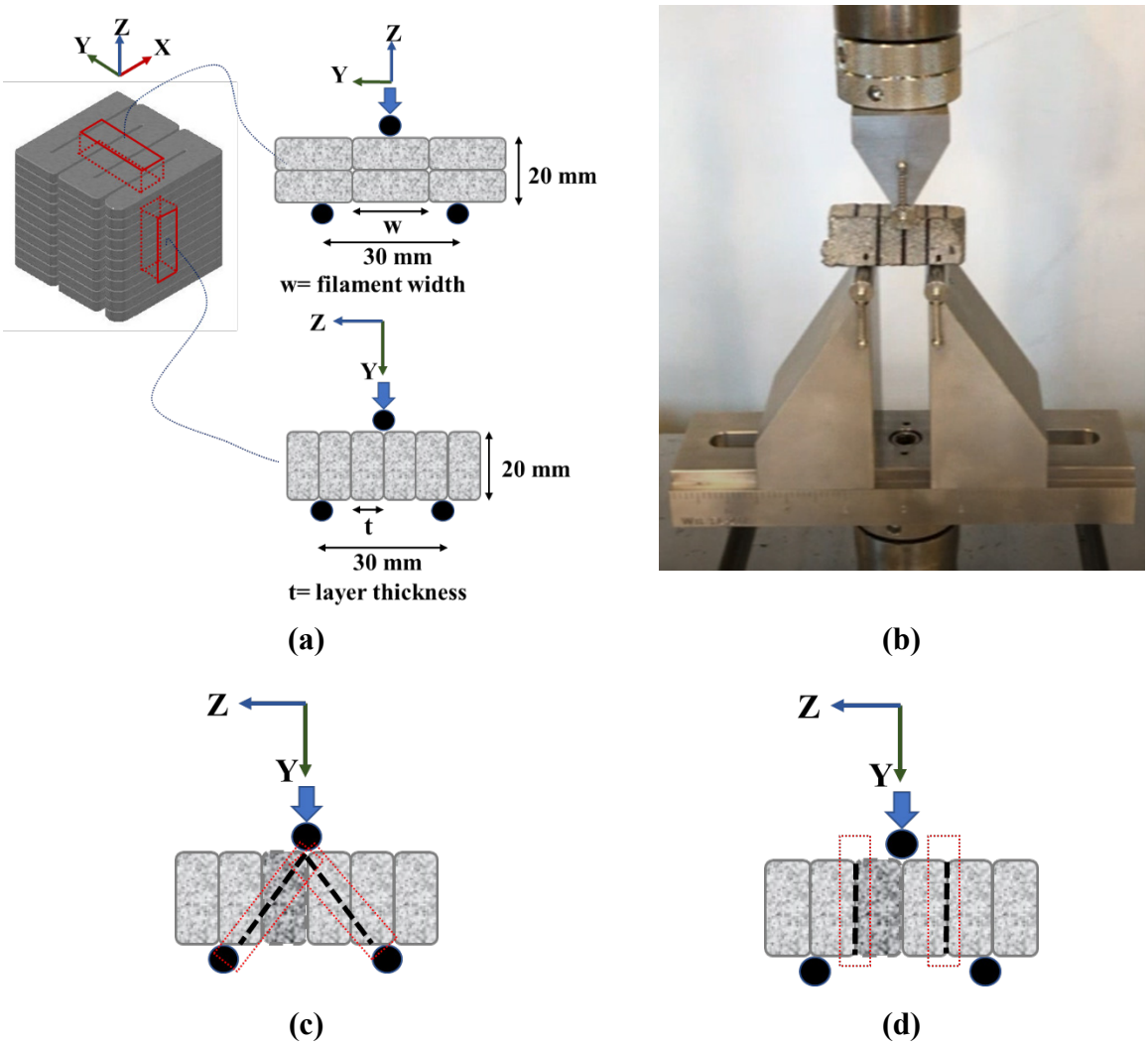

Figure 22. Short beam shear test. (a) Specimen extraction and testing schematic for interfilamentous (top) and interlayer (bottom) shear test, (b) Specimen during testing, (c) Shear failure mechanism through the concrete matrix, (d) Shear failure mechanism through the interlayer interface.

Results and Discussion

Rheological Measurements, Initial Setting Time, and Slump

The hysteresis curves of the 3D print concrete mix were obtained at 0, 15, 30, and 45 minutes and are shown in Figure 23a. The yield stress, viscosity, thixotropy and their evolution with

time are shown in Figure 23b, c, and d, respectively. Trendlines based on mean values are also shown in Figure 23.

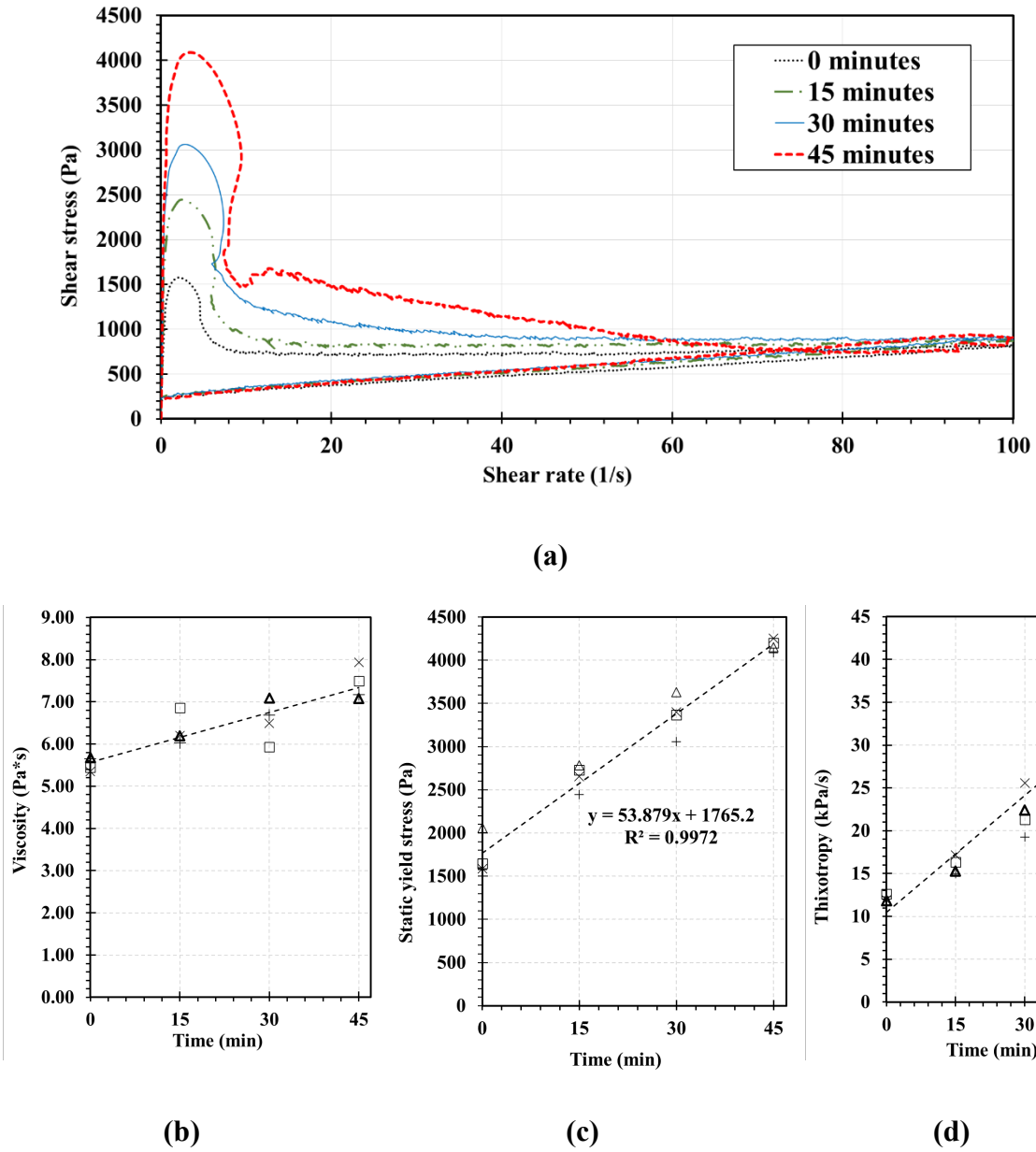

Figure 23. Rheological behavior of the fresh concrete used for 3D printing. (a) Hysteresis loop test. (b) Viscosity. (c) Static yield stress. (d) Thixotropy. The trendline is based on mean values.

`

Initial static yield stress of 1765 Pa was observed at time "0". This value increased with time, as expected for a colloidal paste. The initial yield stress falls above the minimum range for a single 10 mm thickness layer extrusion reported in the literature [51,53] to prevent gravitational flow from happening. The space between aggregate particles, saturated with the binder paste, governs the yield stress of the mix. Attractive forces between cement grains (flocculation) and the development of the hydration process at the contact points result in an increase of the yield stress over time [51]. The structuration rate is defined as the rate at which the static yield stress evolves with time [55]. High structuration rates, in addition to long interlayer printing times, can lead up to the formation of cold joints [55,64,71]. For this mix, the structuration rate was 53.88 Pa/min. Viscosity values were observed to slightly increase with time. The measured values were similar to those reported by others [172]. Concrete thixotropy represents the continuous reduction of viscosity with time when a concrete sample that has been at rest is subjected to flow and the recovery of viscosity as a function of time when this flow is interrupted [173]. Thixotropy is closely associated with the ability of the colloidal material to create an internal structure at rest, and it is of paramount importance for printing applications [53]. Concrete thixotropy of the 3D printed concrete is reported in Figure 23.d and shows a significant increase with time, as reported by others [21,161]. The initial setting time results show a setting time of 240 min for the 3D printed concrete mix. The setting time is closely related to the green strength of the mix. For this reason, a long setting time is required. However, too long of a setting time can affect the buildability of the mix. 3D printed concrete showed a slump of 8.5 ± 1.8 mm.

`

Buildability Test

The buildability results are presented for 1, 2, and 3 adjacent filaments (Figure 24). No signs of local instability of the filaments were observed in contrast to the observations made by others [11]. All the buildability specimens failed due to global buckling, as shown in (Figure 24b). For a given layer to be stable, the static yield stress of the subsequent layer must be at least equal to the gravitational forces exerted on those layers due to the self-weight. This means that the vertical stress acting on a layer is given by:

Equation 5. Stress buildability criteria under the consideration of gravitational stresses

$$\sigma_V(t) = \rho g h(t) = \rho g \dot{H} t \qquad \text{(Equation 5)}$$

Where ρ and g are the density of the printed material and the gravity constant, and h(t) the height of the structure above the studied layer at a given time. This height can also be defined as the printing build-up speed "$\dot{H}$" multiplied by the time since deposition of the studied layer "t".

The printing build-up speed is critical for this process since the yield stress evolution is time-dependent. The main factors affecting the buildability test are shown in Figure 24.c. Furthermore, the strain of the bottom layer must remain below the critical failure strain. These criteria were satisfied with the concrete mix and printing parameters reported herein.

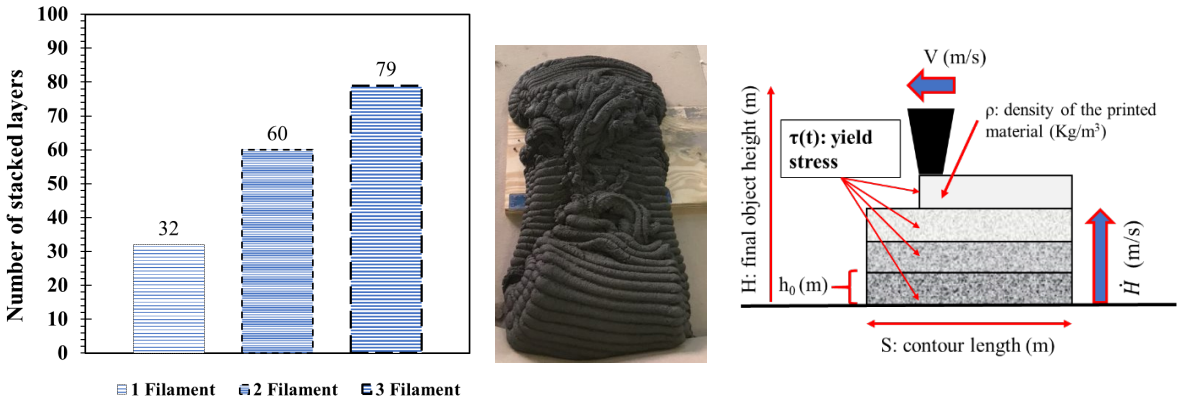

(a) **(b)** **(c)**

Figure 24. Empirical buildability test. (a) Relation between the number of horizontal filaments and the stacked layers before collapse for the printing and geometrical configuration shown in Figure 21. (b) Specimen with three adjacent filaments after a collapse. (c) Factors affecting the buildability test.

Density

The density of the dry cut 120x120x120 mm specimens was measured. 3D printed concrete showed an average dry density of 2201 kg/m^3 compared with 2114 kg/m^3 for conventionally cast concrete specimens produced using the same mix (Figure 26a). The difference is statistically significant (T-test, α=0.05), and it can be attributed to the compaction of the 3D printed concrete due to the filament extrusion process. This printing configuration increases the density of the extruded material by reducing the total porosity. Similar findings were reported by other researchers [16,17,20]. However, T-tests (α=0.05) among the specimens printed with different infill printing patterns showed no significant difference in 3D printed concrete density.

`

Compression and Shear Tests

The stress-strain graphs for the selected median curves are shown in Figure 25. The compressive strength, compression strain at failure, and Young's modulus of elasticity of the 3D printed concrete specimens are shown in Figure 26b, c, and d, respectively.

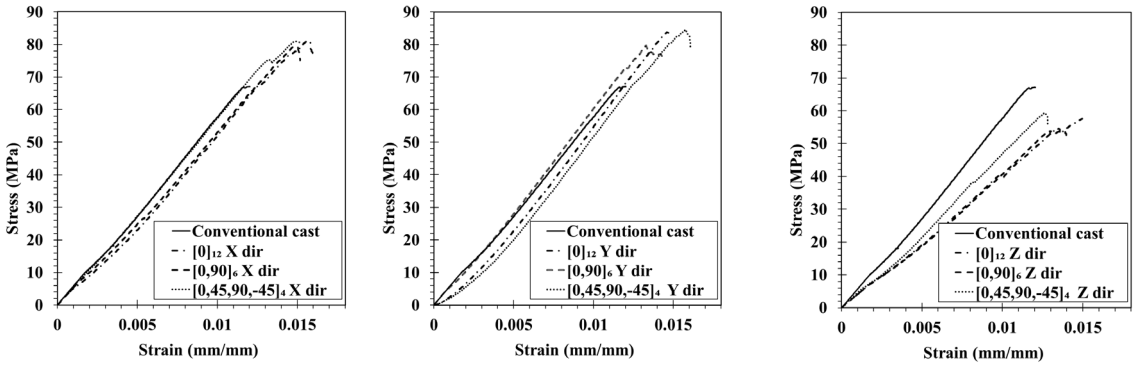

(a) **(b)** **(c)**

Figure 25. Comparison between stress-strain graphs for the selected median curves using conventional cast specimens as a reference. (a) X-direction testing. (b) Y-direction testing. (c) Z-direction testing

The properties of hardened 3D printed concrete for the different testing directions and for all the infill printing patterns were compared. It can be observed that the Z direction (printing direction) is significantly weaker than the X and Y directions (T-test, α=0.05) in terms of ultimate compressive strength (60 MPa for Z direction and 80 MPa for X and Y directions – Figure 26b) and shows a lower modulus of elasticity (3.7 GPa for Z direction and 5.5 GPa for X and Y directions – Figure 26d). However, the strains at failure and the densities are not significantly different in the three directions (Figure 26c). This can be attributed to the difference between the interfilamentous shear strength (shear strength at the interface between filaments) and the interlayer shear strength (shear strength between layers). Similar strains at failure for 3D printed specimens have been reported by others [107].

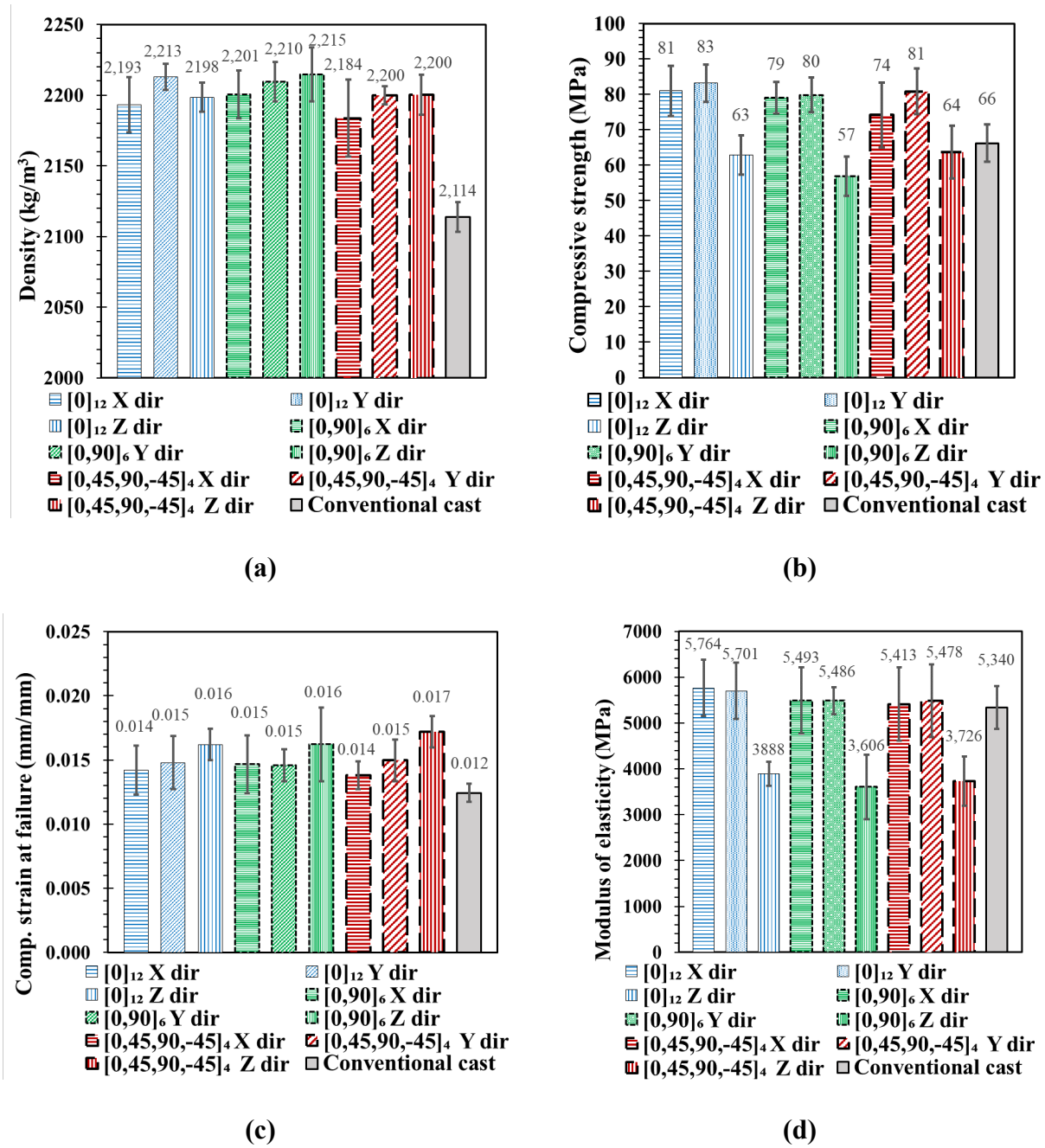

Figure 26. Properties of hardened 3D printed concrete compared with conventionally cast concrete: (a) Dry density, (b) Compressive strength, (c) Compressive strain at failure, and (d) Modulus of elasticity.

We argue that the interfilamentous shear strength is weaker than the interlayer shear strength. This phenomenon might be attributed to the presence of a selective macro-porosity at the

`

interfilamentous interface due to underfilling. Other researchers have reported on the presence of this type of porosity [16,20,21]. The phenomenon as described in the literature is depicted in Figure 10. The improved interlayer shear strength (Figure 28b) can be attributed to the high vertical pressure generated by the printing process compared with the pressures exerted between the filaments on the same layer. This pressure enhances the interlayer adhesion to the previous layer independently of the printing pattern. As depicted in Figure 26, the voids between the filaments create weak vertical planes and potential cracks under vertical (Z direction) loading. Such vertical weak planes will result in weaker mechanical behavior (strength and stiffness) in the vertical Z directions compared with the in-plane X and Y directions, thus creating an anisotropic behavior of 3D printed concrete. The size and, consequently, the effect of these voids at the filament interface is a function of the thickness to width ratio of the filament, the material rheological properties, and the printing path configuration and process.

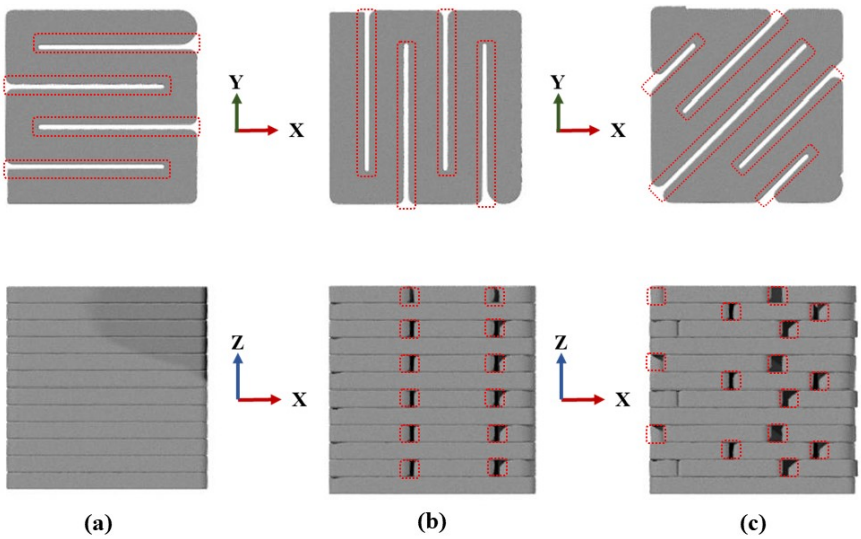

Figure 27. Schematic of 3D printed concrete showing potential formation of voids at the inter-filament vertical planes for the different infill printing patterns. (a) $[0]_{12}$. (b) $[0,90]_{6}$. (c) $[0,45,90\text{-},45]_{3}$.

`

The significance of infill printing patterns on the hardened 3D printed concrete behavior was analyzed in all the testing directions. No significant differences (T-test, $\alpha=0.05$) were found while comparing the ultimate compressive strength, strain at failure, or modulus of elasticity among all infill printing patterns for each testing direction. This means the infill printing patterns might have very little to no effect on 3D printed concrete anisotropy. Furthermore, comparing the 3D printed concrete specimens with the conventionally cast concrete, it can be observed that the mechanical properties of 3D printed concrete in the X and Y directions are higher than conventional cast concrete. 3D printed concrete showed a 20% increase in ultimate compressive strength and a 20% increase in ultimate strain compared with conventional cast concrete. No significant (T-test, $\alpha=0.05$) difference was observed in terms of modulus of elasticity in the X and Y directions for 3D printed concrete compared with conventional cast concrete.

The improvement in the mechanical properties of 3D printed concrete in the X and Y directions compared to conventional cast concrete is related to the compaction of the material during the extrusion process. The filament pressing creates an overall denser structure [17,58] (the total porosity is lower and the density higher). However, there is selective distribution of the macro-scale porosity induced by the printing process. These size range pores can influence overall mechanical performance by acting as stress concentration discrete areas. The presence of macro-scale pores at the interlayer interface (parallel to the X and Y directions) is lower while comparing to conventional cast concrete due to the filament pressing. This would explain the improvement in the mechanical properties of 3D printed concrete in the X and Y testing directions compared to conventional cast concrete. However, most of these macro-scale pores are distributed at the interfilamentous interface (parallel to

`

the Z-direction). This happens because the pressure and contact between filaments while printing (especially changing the direction) is not uniform.

Short beam shear tests were performed to demonstrate the difference between the interfilamentous shear strength and the interlayer shear strength. Three different types of specimens (interlayer, interfilamentous interfaces, and regular cast concrete) were tested, as shown in Figure 22. The failure modes and shear test results are shown in Figure 28. It can be observed that the interfilamentous shear strength with (mean value of 1.47 MPa) and the shear strength for conventionally cast concrete (mean value of 1.38 MPa) are statistically significantly weaker (T-test, $\alpha=0.05$) than the interlayer shear strength (mean value of 1.86 MPa). No significant difference (T-test, $\alpha=0.05$) was found between the interfilamentous shear strength and shear strength of conventionally cast concrete. It is important to note that cracks do not propagate through the interface in all interlayer and interfilamentous shear tests but rather in the adjacent concrete, as shown in Figure 28. Studying crack propagation patterns is beyond the scope of this study.

`

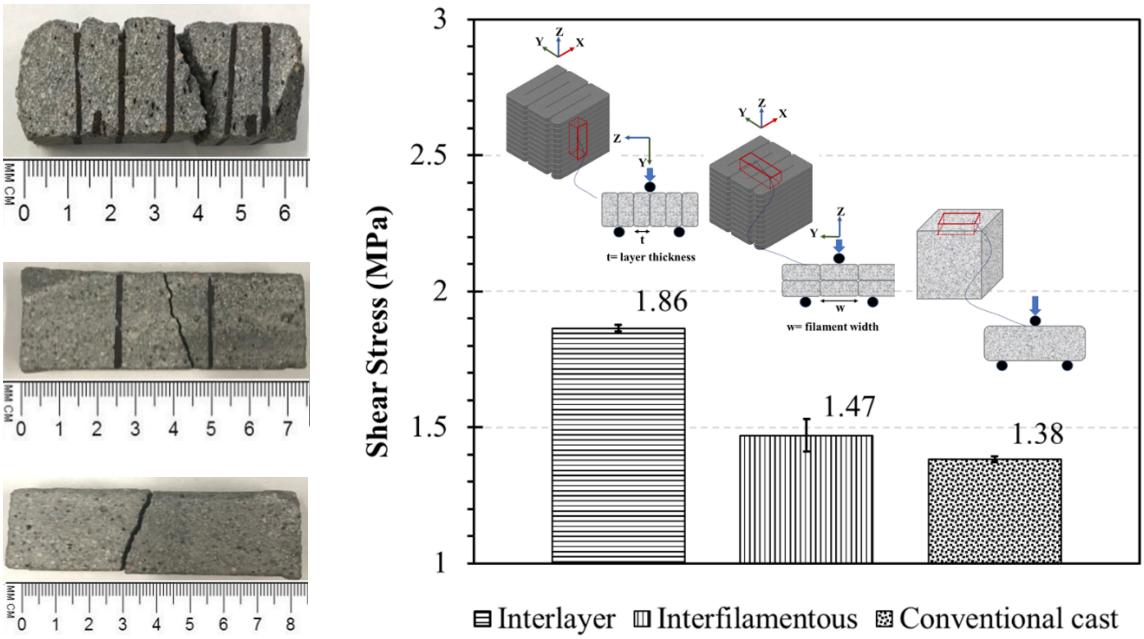

(a) **(b)**

Figure 28. Short shear beam testing of 3D printed concrete and regularly cast concrete. (a) The shear failure mode of both 3D printed concrete and conventionally cast concrete. (b) Shear strength of interlayer interface, interfilamentous interface, and convention

Macroporosity

To further explain the described mechanism, we examined the macroporosity of 3D printed concrete at the interfaces. Light microscopic images were taken from three cuts of concrete surfaces, as shown in Figure 29.

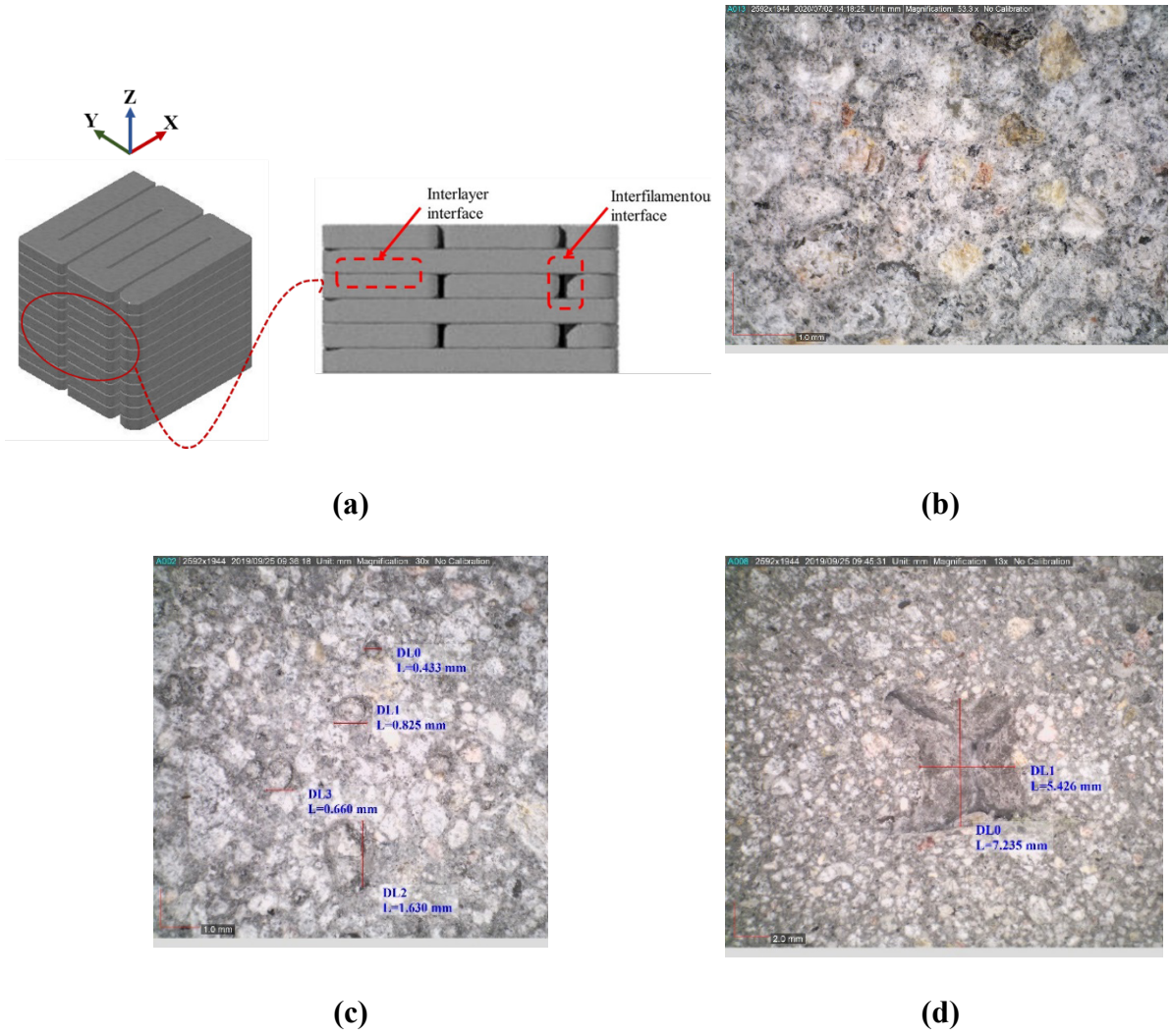

Figure 29. Macroscopic porosity observed in 3D printed concrete. (a) Schematic showing locations investigated for 3D printed specimens. (b) Light microscope photo of conventional cast specimen where no macropores can be observed. (c) Light microscope photo showing pores at the interfilamentous interface.

Images of cuts at the interlayer interface, the interfilamentous interface, and a conventionally cast specimen are shown in Figure 29b, c, and d, respectively. While macropores at the submillimeter scale (i.e., micropores) were observed in cuts at the interlayers' interface (Figure 29c), relatively large macropores were observed at the interfilamentous interface

`

(Figure 29d). The above observations support the argument that pressure exerted during the printing process reduces the overall porosity of 3D printed concrete. This pressure could be purposefully used in design modify the final printed properties of the product. However, significant macro-scale porosity exists at the interfilamentous interface creating weak planes and significant anisotropy that seems to be independent of the infill printing pattern.

`

Chapter 4. Rheological and Mechanical Characterization of 3D Printed Polymer Concrete

Whereas extensive research has been focused on investigating cement-based 3D printable concrete, less attention has been made to investigating 3D printed PC. The composition of PC makes it an excellent alternative for 3D printing. Furthermore, the numerous industrial PC applications and their vast manufacturing possibilities as precast elements make 3D printing and automation of PC manufacturing of high relevance. Rheological characterization is an essential step to produce 3D printed PC. The work presented herein provides a systematic method to characterize PC's rheology and evaluate the significance of the critical parameters of PC mix on its rheological properties.

This chapter reports on the potential use of PC for 3D printing applications. The influence of mix design parameters, specifically rheology modifier content, filler to polymer ratio, and aggregate to polymer ratio on the rheological properties of a 3D printable PC, are investigated. The rheological properties of seven PC mixes are tested and characterized. PC can be described as a Bingham pseudoplastic material, and a Herschel-Bulkley model can accurately describe its rheological behavior (dynamic shear stress) over time. The evolution of the static yield stress over time was found to follow an exponential trend. Using these models to predict PC's dynamic and static yield stress shall enable the design of efficient and stable 3D printing. Finally, 3D printed PC shows good mechanical performance with compressive strength above 30 MPa (4351 psi) at seven days of age. Automation of the PC precast industry using 3D printing will create new opportunities for the use of PC in civil infrastructure.

`

Rheological Characterization

Materials

A Novolac epoxy resin (Euclid Chemical, Cleveland, OH) was mixed with 44% Benzyl alcohol hardener (Euclid Chemical, Cleveland, OH) as weight ratio per the manufacturer's recommendation. Pyrogenic fumed silica (Cabot Corporation, Alpharetta, GA) with a hydrophobic surface treatment, a specific surface area of 120 m^2/g, and a density of 2.2 g/cm^3 was mixed with the resin to modify its rheological properties. Medium-graded silica sand with a nominal maximum size of 2.36 mm was used. Figure 30 shows the size distribution of the aggregate used in producing 3D printed PC. This maximum aggregate size was selected to ensure proper printing resolution for the 40 mm nozzle diameter**.**

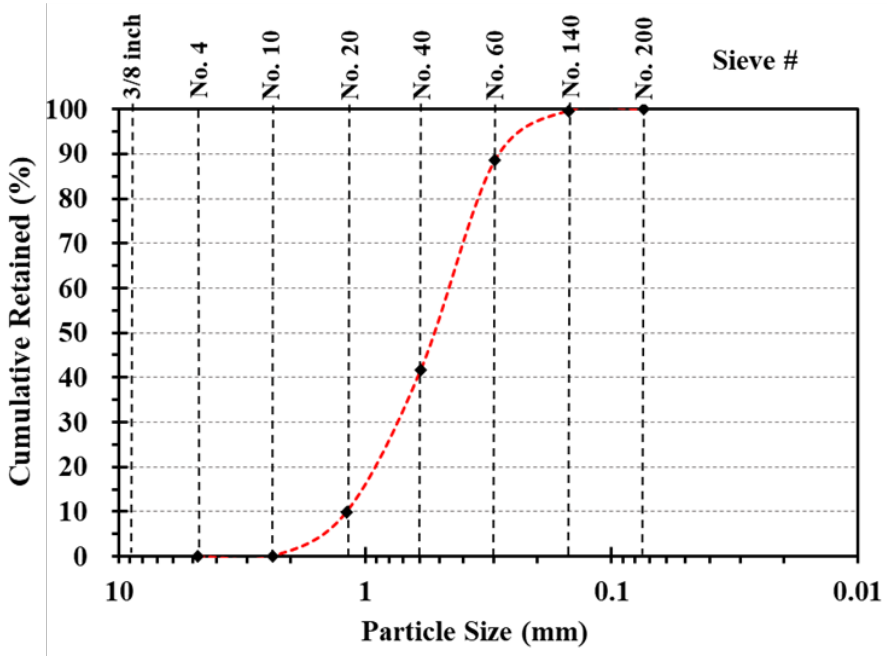

Figure 30. Sieve size distribution of the sand.

Class-F fly ash (Salt River Materials Group, Scottsdale, AZ) compliant with ASTM C618-19 [174] with a density of 2.3 g/cm^3 and silica fume (BASF, Florham Park, NJ) with a density of 2.2 g/cm^3 were also used as fillers to increase the packing fraction and consequently the

`

mechanical performance. The fly ash to silica fume weight ratio was kept constant at 2:1 for this investigation. Higher fly ash content was used since it has been proven to yield better compressive strength for PC [89]. Different proportions of rheology modifiers (fumed silica), fillers (silica fume and fly ash), and aggregate (sand) were studied to investigate their effect on the rheological properties of PC. The changes in the PC mixes were made such that the polymer (resin and hardener) volume fraction of all the mixes were kept between 41–44%. Seven mix proportions, denoted PC1 to PC7, were investigated and are presented in Table 2**.** The effect of each component on the expected rheology of PC was investigated.

Table 2. Mix design and proportions (kg/m3) for 7 PC mixtures.*

	Reference	Group 1		Group 2		Group 3	
	PC1	PC2	PC3	PC4	PC5	PC6	PC7
Resin	305.0	305.4	304.6	311.0	299.2	315.4	295.5
Hardener	135.5	135.7	135.3	138.2	132.9	140.2	131.3
Fumed Silica (FS)	21.4	18.3	24.3	21.8	20.9	22.1	20.7
Silica Fume (Filler 1)	73.4	73.5	73.3	59.9	86.4	75.9	71.1
Fly ash (Filler 2)	146.8	147.0	146.6	119.9	172.9	151.9	142.3
Sand	1256.6	1258.4	1254.9	1281.5	1232.7	1207.2	1301.6
FS/ Resin (%)	7	**6**	**8**	7	7	7	7
Filler/Resin (%)	72	72	72	**58**	**87**	72	72
Resin /Aggregate (%)	24	24	24	24	24	**26**	**23**
Polymer Volume Fraction (%)**	43	43	43	44	42	44	41

* 1kg/m^3 = 1.6856 lb/yd^3; **Polymer = resin + hardener.

The first mix (PC1) is based on two-year research investigations of 3D printed PC and is denoted herein as the reference mix [175]. Changes were introduced to the reference mix (PC1) to investigate the significance of the different PC mixture constituents on the

`

rheological behavior of 3D printed PC and to develop rheological behavior models to predict the critical rheological parameters necessary for 3D printing of PC as described in Figure 12**.** The mixes PC2 to PC7 were divided into three groups (Group 1, Group 2, and Group 3). Group 1 includes mixes PC2 and PC3 with varying contents of the rheology modifier (fumed silica) than the reference mix (PC1). Group 2 includes mixes PC4 and PC5 with varying content of fillers (silica fume and fly ash) compared with the reference mix (PC1) to investigate the effect of the filler to polymer ratio. Group 3 includes mixes PC6 and PC7 with varying content of aggregate compared with the reference mix (PC1) to investigate the significance of the aggregate to polymer ratio.

PC Mixing and Rheology Characterization

A 4.7-liter bowl-lift standard mixer was used for mixing the PC. The stepwise mixing protocol is presented in Table 3**.** Rheology measurements were performed using a Brookfield RST soft solid tester rotational rheometer (AMETEK Brookfield, Middleboro, MA)**.**

`

Table 3. Stepwise mixing protocol and rheology testing of PC.

Time (min)	Procedure
-	Mechanical mixing of the fumed silica in the polymer matrix
0:00	Mixing the polymer resin and hardener at low speed for 1 minute
1:00	Stop mixing. Scrap the bowl. Add the fine fillers and mix at low speed for 1 minute
2:00	Stop mixing. Scrap the bowl. Add the aggregate while mixing at low speed for 1 minute
3:00	Mixing the PC at high speed for 3 minutes
6:00	End of mixing and casting rheology samples for different times [0, 15, 30, and 45 min]
7:00	Rheology testing at 0 min from casting
22:00	Rheology testing at 15 min from casting
37:00	Rheology testing at 30 min from casting
52:00	Rheology testing at 45 min from casting

For the PC, a shear vane spindle with a diameter of 20 mm, a length of 40 mm, and a shear stress range of 5.2 to 3400 Pa was used (Figure 31). The test performed is a hysteresis technique introduced by Weltmann and Green [167] and is widely used for thixotropic particulate suspensions, including cementitious mixes [21,161,168]. The shear rate was ramped up from 0 s^{-1} to 100 s^{-1} in 60 s and then down from 100 s^{-1} to 0 s^{-1} in 60 s, as shown in Figure 31**.** The rheological behavior of the polymer (mixed resin and hardener) with no fillers was studied following the same procedure but using a coaxial spindle (40 mm diameter). The measurement values (Torque and rotational speed) were converted into rheological parameters (Shear stress and shear rate) using the conversion factors: k & B depicted in ASTM D4648/D4648M−16 [176].

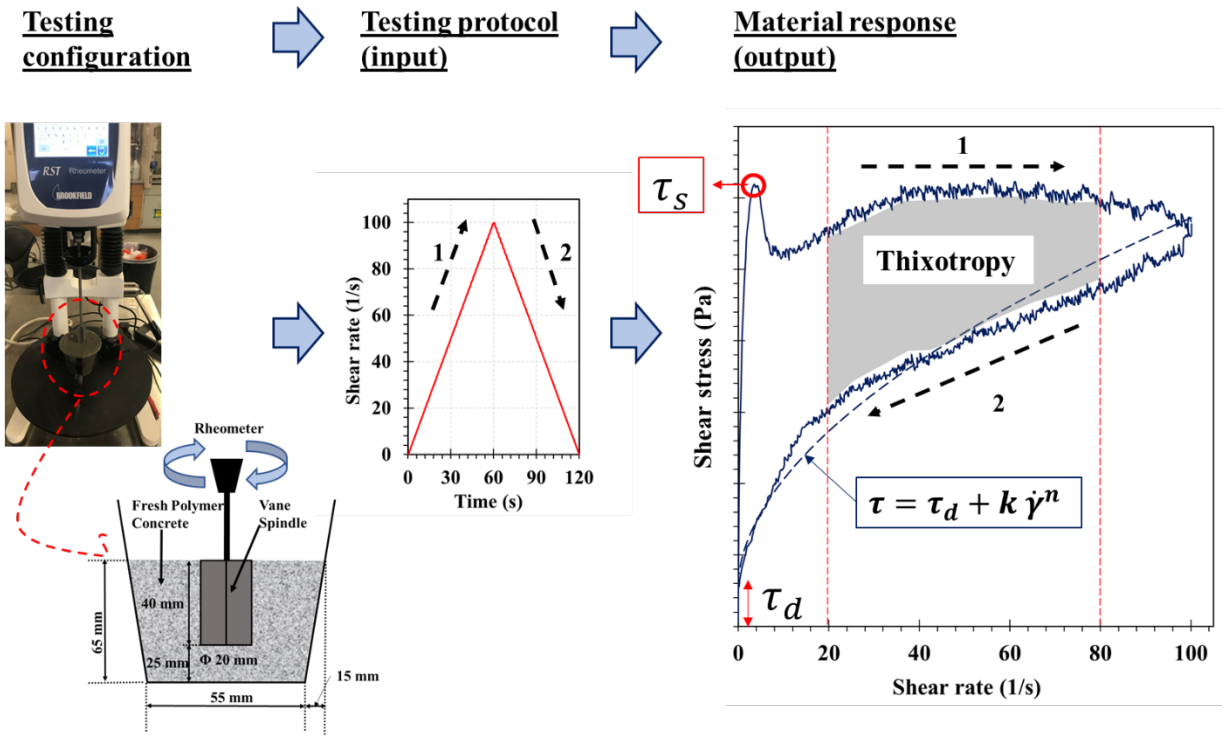

Figure 31. Rheology test. From left to right, testing configuration, shear rate input over time, and typical material response for PC. Arrow 1 indicates an increase in shear rate, while arrow 2 indicates a reduction in shear rate. τ_d is dynamic yield stress, and τ_s is static yield stress.

Five (5) specimens of 68.5 ml volume were tested for the polymer resin at different testing times (0, 15, 30, 45 min). Limiting the test time to 45 minutes was based on prior published work suggesting 30 minutes as the limit for assessing 3D printed concrete [161]. The PC mix reported herein was designed to be printable for up to 45 minutes. The concrete samples were not pre-sheared before the test to quantify the static yield stress. The material was mixed, as indicated in Table 3, and then collected from the mixer.

Five (5) specimens were tested at each time interval (0, 15, 30, and 45 min) for each of the 7 PC mixes, leading to a total of 5*4*7= 140 specimens. The specimen's geometry for the rheological test of PC is shown in Figure 31. Each sample was left undisturbed until testing

`

time and tested only once to prevent the material from having a shear history (besides the mixing). Time '0' denotes the time immediately after the mixing process was concluded, as specified in Table 3. The temperature during the test was kept at 23 ±2ºC. The typical hysteresis loop response for the PC is shown in Figure 31.

Rheology Modeling

The typical hysteresis loop response (represented schematically in Figure 31) shows that the static yield stress τ_s is obtained as the peak shear stress in the first part of the hysteresis loop (increasing shear rate). Thixotropy was calculated as the area under the two curves, integrated between 20 s^{-1} and 80 s^{-1} as described by other authors [21,161]. The shear stress at a zero-shear rate in the loop's descending part is defined as dynamic yield stress, τ_d.

To model, the rheological behavior of PC, a Bingham pseudoplastic material (Figure 12) was assumed. This implies that the material behaves as a rigid body up to a defined shear stresses threshold, then it will flow after a shear stress threshold (dynamic yield stress, $\tau_{d.}$). After this point, the relationship between shear stress and shear rate is not linear (pseudoplastic). This behavior is shown in Figure 31 for the descending part of the hysteresis loop (depicted as 2). A Herschel-Bulkley [177] generalized model was proven to provide an excellent correlation to explain the non-linear relationship between the shear rate and the stress experienced by the material. The Herschel-Bulkley model showed better adherence to the experimental data for cement pastes compared with Bigham and modified Bigham models at shear rates up to 100 s^{-1} [178]. This Herschel-Bulkley [177] model can be written for a pre-sheared material as described by Equation 6 and Equation 7.

Equation 6.Time-dependent Herschel-Bulkley model. Liquid-state.

$$\tau > \tau_d \xrightarrow{Then} \tau = \tau_d + k(t)\dot{\gamma}^{n(t)} \quad \text{(Equation 6)}$$

`

Equation 7. Time-dependent Herschel-Bulkley model. Solid-state.

$$\tau < \tau_d \xrightarrow{Then} \dot{\gamma} = 0 \quad \text{(Equation 7)}$$

in which *k(t)* and *n(t)* are time-dependent material parameters named consistency and flow index, respectively, and τ_d is the dynamic yield (shear) stress representing the stress required in a pre-sheared sample to start the flow. In this model, the consistency (*k*) is a constant of proportionality for a given time. A flow index (*n*) equal to 1 represents a Newtonian material. Flow indexes (*n*) diverging from 1 represent the degree to which materials diverge from the Newtonian hypothesis (<1 shear-thinning material and >1 shear-thickening material), as shown in Figure 12. A schematic representation of the model is presented in Figure 31. The material's response for the decreasing part of the loop (between $80s^{-1}$ and $0s^{-1}$) was fitted into a Herschel-Bulkley model as specified in Equation 6 and Equation 7. The wall shear stress, widely known as the shear slip effect, was neglected. Other researchers showed using the finite element method that for a Herschel-Bulkley (Bingham) material, a local area extends along the imaginary circle around the tips of the blade. Apart from the region around the tips or within the circle itself, the shear stress rapidly decreases radially to a value less than the yield stress of the material [179]. Therefore, the shear stress of the container can be neglected.

PC Printing, Curing, and Compression Testing

A gantry robot 3D printer with 3 degrees of freedom and a printable area of 2.0 x 2.0 x 2.0 m was used. Cube specimens of 1.8 in x 1.8 in x 1.8 in (45 x 45 x 45 mm) were printed for the reference mix PC1 by using a 40 mm diameter nozzle, 10 mm layer height, and 50 mm/s linear printing speed. The temperature during the printing process was kept at 23 ±2 ºC. The extrusion rate represents the rotational speed of the helicoidal extruder that pushes the

`

material through the nozzle (depicted as ω in Figure 14). To print the specimens, it was kept constant at 4 rad/s (19.2 L/min). For the geometry printed and the printing settings reported herein, the build-up rate ($\dot{H}$), defined schematically in Figure 14, is 0.05 cm/s.

Curing of PC differs from cement concrete [84]. PC is not cured in a humid environment since there is no hydration process taking place but is typically cured in a dry air environment at ambient temperature. This is attributed to the fact that curing aims to allowing the polymerization process to continue and be completed. Studies reported that PC achieves compressive strength in the range of 70-75% of its target compressive strength after one day of age [180–182] and most of its strength after seven days of age if cured at ambient conditions (i.e., 21-24 ºC) [183]. Following these recommendations, specimens were air-cured for 7 days at controlled ambient conditions of 23 ±2 ºC and then tested. The compression test of the 3D printed concrete cubes was performed using a Tinius Olsen universal testing machine with a resolution of 1 lbf (4,45 N) and a maximum capacity of 400 Kip (1779 kN). 5 cubes 2.0 in x 2.0 in x 2.0 in (51 x 51 x 51mm) were cast as per ASTM C109/C109M-20b [184]. The compressive strength of standard cubes is compared to the compressive strength of 3D printed cubes of 1.8 in x 1.8 in x 1.8 in (45 x45 x 45 mm) cut from the continuously printed filament and tested in the vertical (Z) direction. The difference in size between the two cubes is negligible, and both specimens satisfy the nominal maximum aggregate size requirement by ASTM C109/C109M-20b [184]. A displacement rate of 0.04 in/min (1 mm/min) was used throughout the test. The compressive strength was calculated as the maximum load obtained during the test divided by the initial cross-sectional area of the specimen. Figure 32 shows the printing process and the specimens prior to testing.

`

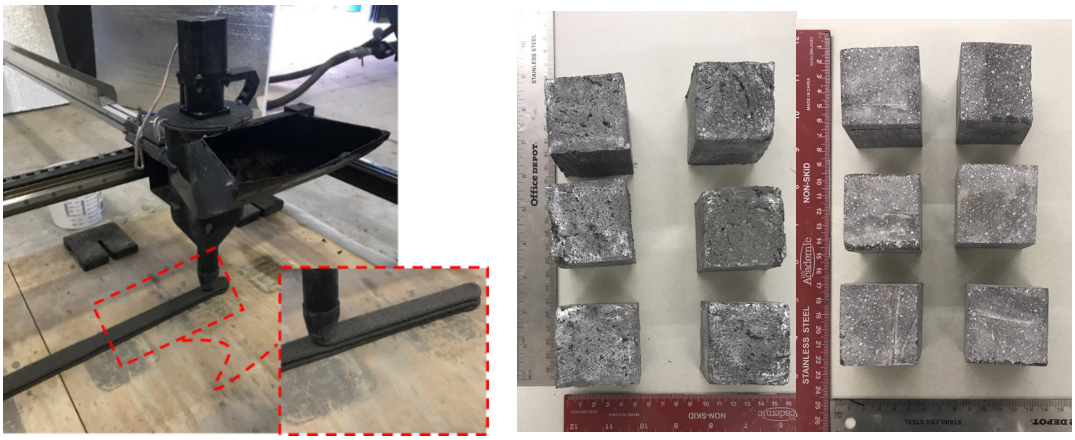

(a) **(b)**

Figure 32. (a) 3D printing of the PC1 mix, (b) conventional cast cubes (left) and 3D printed cubes after saw cutting from 3D printed filaments (right).

Results and Discussion

The flow properties of the Novolac epoxy polymer (resin and hardener) and its evolution over time are presented in Figure 33**.**

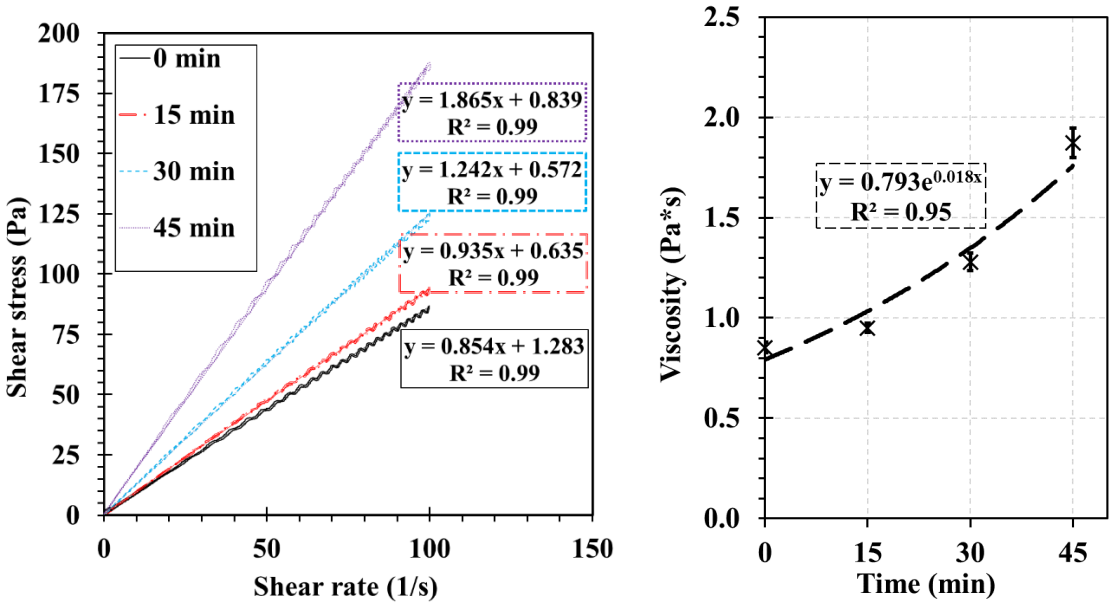

(a) **(b)**

Figure 33. Rheological time-dependent properties of Epoxy Novolac polymer; (a) Newtonian behavior of the polymer with time; (b) viscosity evolution of the polymer with time.

`

It can be observed how the polymer shows a Newtonian flow behavior (schematically presented in Figure 12). The curves up and down almost match, leaving an area under the curve close to zero, which means the polymer itself does not show a significant thixotropic nature. This behavior of Novolac epoxy was reported in the literature [185]. Moreover, the dynamic yield stress of Novolac epoxy is almost zero. Since the material abides a Newtonian behavior, the viscosity can be inferred as the slope of the shear stress-shear rate data. The viscosity evolution over time is apparent in Figure 33b, and it follows an exponential trend (R^2=0.95).

For the PC, as explained above, the shear stress versus shear rate data in the decreasing part of the hysteresis loop was fitted to a Herschel-Bulkley model. The average coefficient of determination (R^2) of the seven (PC1 to PC7) mixes at time 0, 15, 30, and 45 min was determined using the least-squares method. The values obtained are 0.97 ± 0.02, 0.97 ± 0.01, 0.94 ± 0.04, and 0.76 ± 0.06 respectively. It should be noted that the model fits very well up to 45 min, after which the model starts to diverge. The model divergence from the pseudoplastic behavior at 45 min is attributed to the nature of the polymer. When the resin is mixed with the hardener, the monomers start to crosslink into polymers (Figure 13) at a specific rate (polymerization rate). At a given time, the number and length of the polymer chains start preventing the material from flowing, and the relationship between the shear stress and the shear rate starts showing instabilities. The consistency (k), flow index (n), and dynamic yield stress (τ_d), the static yield stress (τ_s), and the thixotropy (A_{thix}) are presented in Figure 34, Figure 35, and Figure 36. Figure 34 shows the data for Group 1 (varying content of rheology modifier), Figure 35 shows the data for Group 2 (varying filler content), and

Figure 36 for Group 3 (varying aggregate content). For all the figures, the comparison is made to the reference mix (PC1).

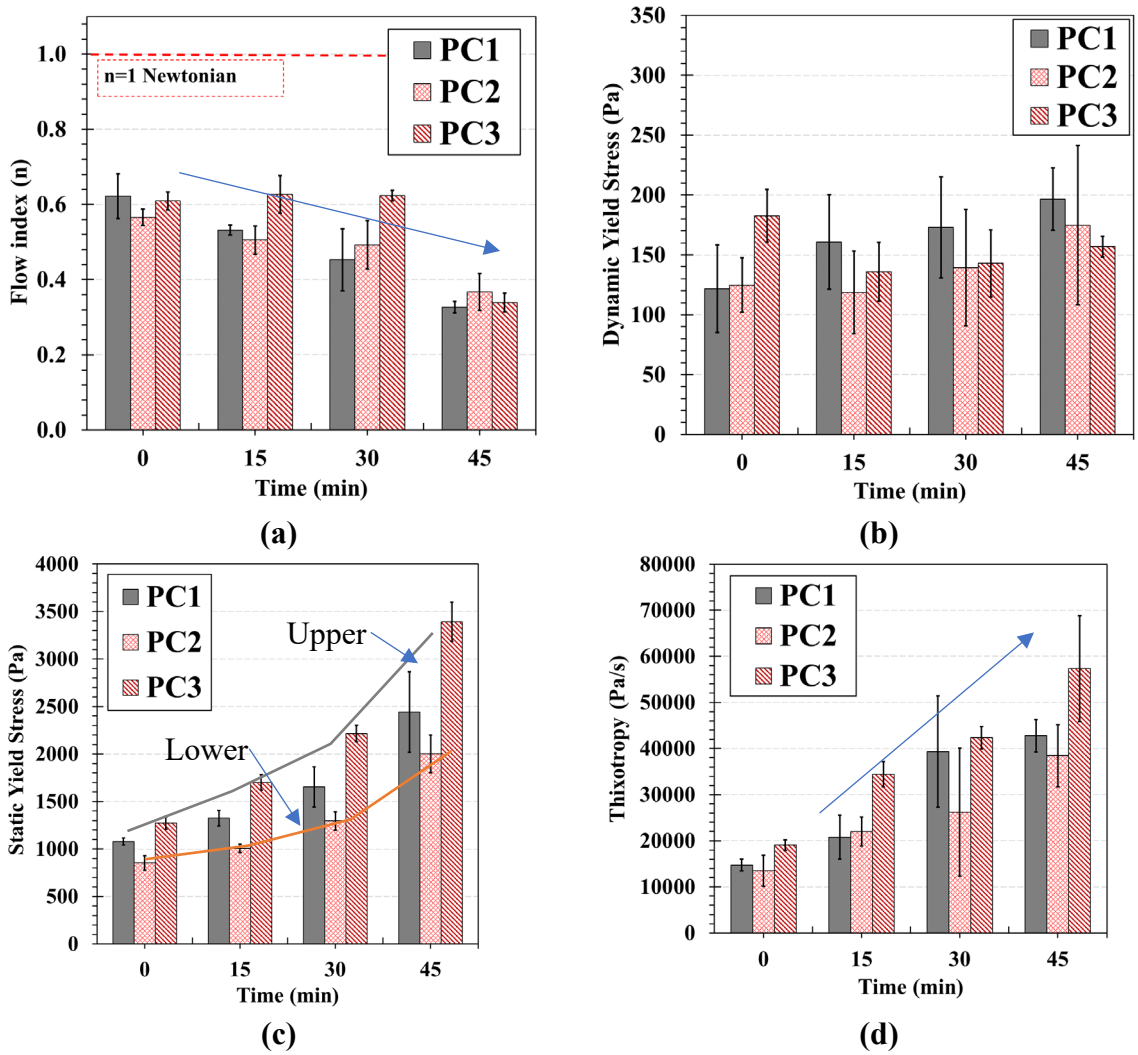

Figure 34. Effect of rheology modifier (Group 1): on (a) flow index (n); (b) dynamic yield stress (τd); (c) static yield stress (τs); (d) thixotropy.

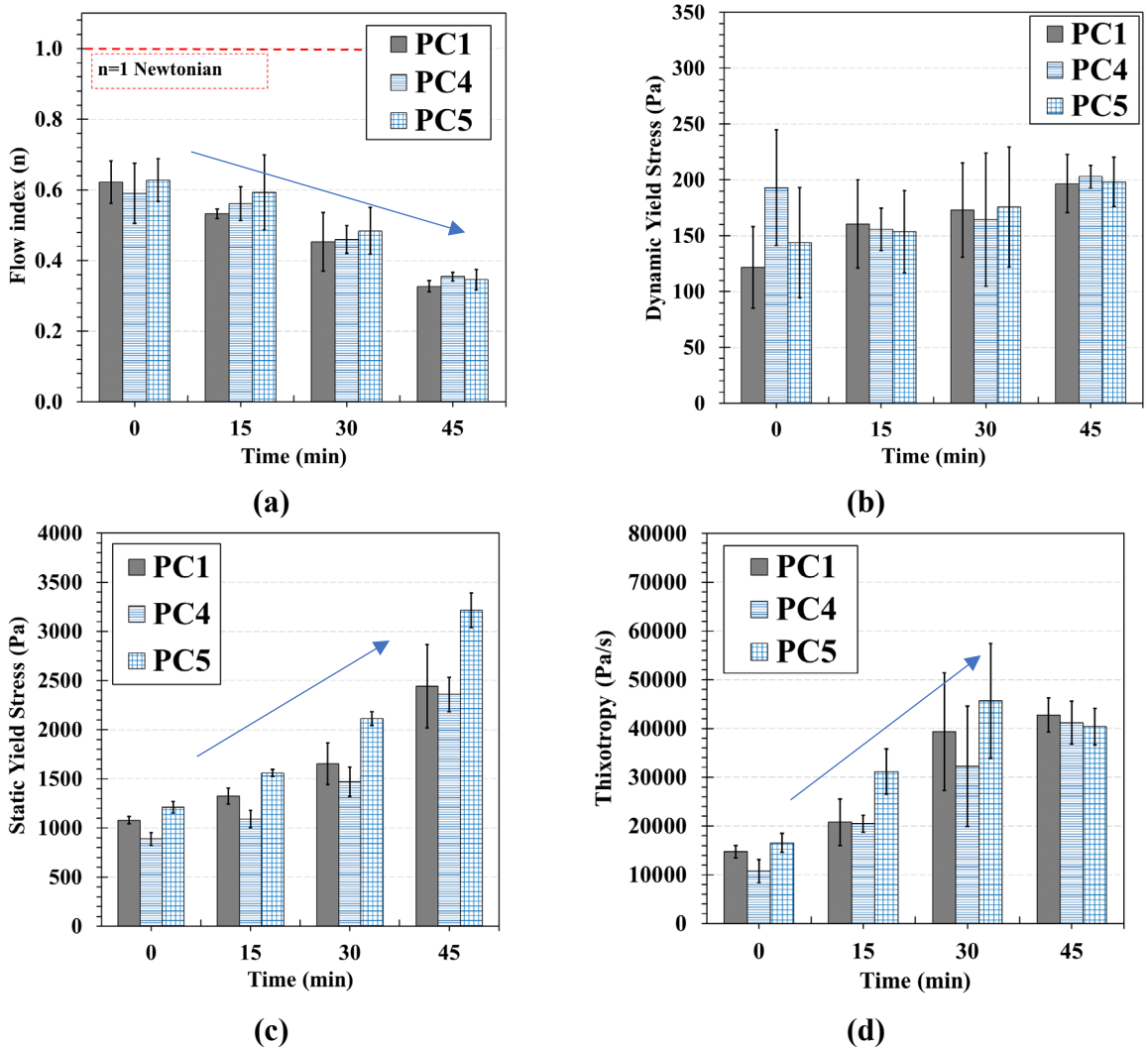

Figure 35. Effect of fillers (Group 2) on: (a) flow index (n); (b) dynamic yield stress (τd); (c) static yield stress (τs); (d) thixotropy.

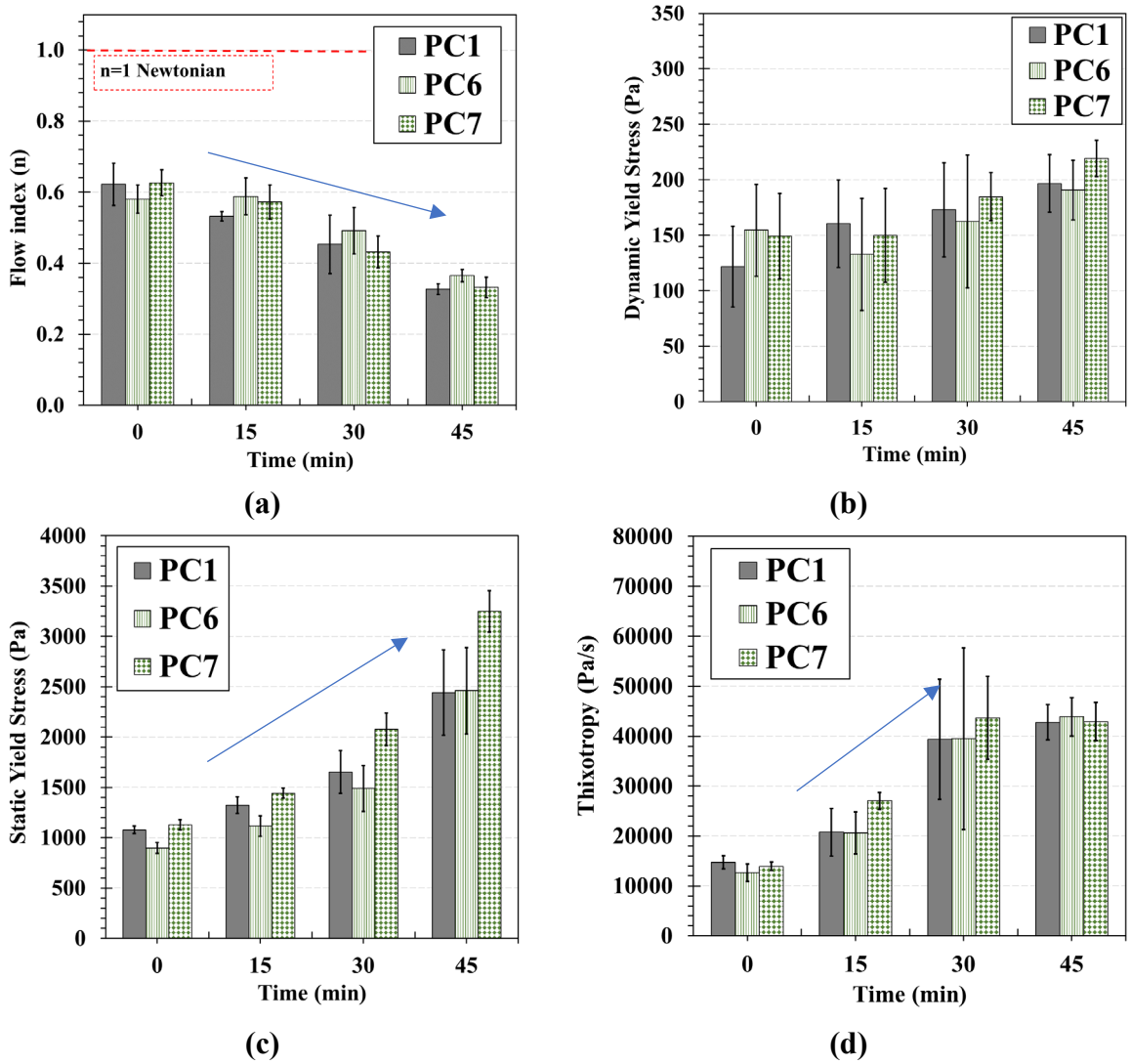

Figure 36. Effect of aggregate (Group 3) on: (a) flow index (n); (b) dynamic yield stress (τd); (c) static yield stress (τs); (d) thixotropy.

The time-dependent evolution of the consistency, *k(t)*, and flow index, *n(t),* was found to be linear. Equation (6) and (7) describe the regression models and their nomenclature.

Equation 8. Linear fitting model for the time-dependent evolution of the consistency, k(t), for 3DPPC

$$k(t)=A*t + B \qquad \text{(Equation 8)}$$

`

Equation 9. Linear model for the time-dependent evolution of the flow index, n(t), for 3DPPC

$$n(t)=C*t + D \quad \text{(Equation 9)}$$

The linear regression variables A, B, C, D, are presented in Table 4**.**

Table 4. Time-dependent linear regression for Herschel-Bulkley's parameters 'k' and 'n' to predict the dynamic yield stress of PC.

	PC1	PC2	PC3	PC4	PC5	PC6	PC7
A	2.042	1.983	2.034	2.217	2.579	2.067	2.928
B	60.2	70.6	46.1	56.2	53.3	56.4	51.6
R^2	0.99	0.95	0.94	0.94	0.97	0.91	0.99

* k(t)=A*t + B

	PC1	PC2	PC3	PC4	PC5	PC6	PC7
C	-0.00643	-0.00406	-0.00543	-0.0054	-0.00637	-0.00494	-0.00682
D	0.63	0.57	0.67	0.61	0.66	0.62	0.64
R^2	0.99	0.89	0.56	0.95	0.94	0.85	0.98

* n(t)=C*t + D

No significant difference was found at any given time for the flow index (*n*) for all the different mixes. This behavior is depicted in Figure 34(a), Figure 35(a), and Figure 36(a) for Groups 1 to 3, respectively. The shear-thinning behavior of the PC can be attributed to the disentanglement of the polymer chains and alignment in the direction of the flow. This rearrangement would facilitate shearing by reducing the particle-matrix interactions (Figure 13), decreasing the apparent viscosity.

The dynamic yield stress is shown in Figure 34 (b), Figure 35 (b), and Figure 36 (b) for Groups 1 to 3. It seems to be time-independent of the mix design variables studied. This

`

means it is entirely dependent on the resin type rather than other PC mix characteristics such as particle surface area, particle size, and distribution. The range of values observed was similar to the one reported by others for cement-based 3D printing concrete [114,161]. The evolution of the static yield stress with time is shown in Figure 34 (c), Figure 35 (c), and Figure 36 (c) for Groups 1 to 3, respectively. Traditionally, for cement-based materials, the rate is constant with time, as suggested by [55,56], and the static yield stress of the material after a resting time '*t*' can be calculated using Equation 6. For PC, the static yield stress was found to grow exponentially with time. The following suggested model predicts the static yield evolution with time:

Equation 10. Time regression model for the static yield stress.

$$\tau_s(t) = E * F^t \quad \text{(Equation 10)}$$

The fitting curve parameters (*E* and *F*) for each one of the 7 PC mixes are presented in Table 5.

Table 5. Time-dependent exponential regression model for the static yield stress.

	PC1	PC2	PC3	PC4	PC5	PC6	PC7
E	1037.8	800.3	1242.8	833.7	1164.4	841.2	1070.8
F	1.018	1.019	1.022	1.022	1.022	1.022	1.024
R^2	0.97	0.96	0.99	0.97	0.99	0.96	0.98

* $\tau_s(t) = E * F^t$

The static yield stress is a physical property of the material [186]. The measured static yield stress in a specific device and protocol is only dependent on the applied torque. The shear rate at which the static yield occurs depends on the geometry and protocol used [187]. Nonetheless, E and F are independent of the shear rate, shear stress and its evolution over

`

time. Therefore, the static yield stress's proposed equation is independent of the testing device and protocol used. Researchers [52] reported a similar exponential growth of the bulk strength for self-consolidated cement-based concrete. Similar values are also reported for cement-based 3D printing concrete [43,114,161]. The upper and lower contours for all the mixes (PC1 to PC7) correspond to the high (PC2) and low (PC3) content of the rheology modifier (fumed silica). This is due to the high surface area of the fumed silica, which prevents the flow at a higher shear rate due to the high frictional forces. The time-dependent exponential growth of the static yield stress of PC is beneficial to ensure the stability of the 3D printed geometry as it allows to conduct the printing at a faster rising speed.

The above investigation of the three groups of PC mixes showed that the rheology modifier content, the filler to polymer ratio, and aggregate to polymer ratio significantly affect the rheology of PC and specifically the static yield stress and thixotropy, as apparent in Figures Figure 34 (c), Figure 35 (c), and Figure 36 (c) for the static yield stress and Figure 34 (d), Figure 35 (d), and Figure 36 (d) for the thixotropy. Furthermore, due to its high surface area, the rheology modifier (fumed silica) seems to have the most significant influence on the rheology of PC. The significance of the high filler and aggregate content on the rheology of PC can be attributed to the high volume of particles that will lead to high particle-matrix interactions, adding resistance to the flow of the PC when a shear rate is imposed. The thixotropy seems to increase with time for all mixes up to 30 min. The thixotropic behavior for all the mixes is governed by the Novolac polymerization, as depicted in Figure 14. This explains why it increases at a similar rate for all the mixes. The magnitude of the thixotropy values is similar to that reported for cement-based 3D printed concrete [114].

`

The average compressive strength of PC1 was 3913.6 ±88.4 psi (27.0±0.61 MPa) for the cast specimens and 4507.2 ±269.6 psi (31.1±1.86 MPa) for the 3D printed specimens (PC1). The difference is statistically significant (*T-test,* α=0.05), showing the 3D printed PC to have slightly higher strength than conventional cast concrete. The slight improvement in the compressive strength might be attributed to the low slump of the PC mix designed for 3D printing, making it unsuitable for conventional casting. Moreover, the nozzle pressure during the printing results in slight compaction that tends to improve the compressive strength [114]. The above investigation demonstrates the potential use of PC for 3D printing. It also illustrates the fact that the rheological properties of PC can be engineered through mix design to meet desired values necessary for 3D printing. Simple models can be developed to predict the static yield stress evolution over time to ensure efficient and stable 3D printing. Finally, the above method can be used to optimize the polymer content in the PC mix to reduce the cost of economic production.

`

Chapter 5. The Effect of Carbon Nanofibers on the Rheological and Mechanical Properties of 3D Printed Polymer Concrete

This chapter examines the effect of carbon nanofibers (CNF) on the rheological and mechanical behavior of 3D printed polymer concrete (PC). Carbon nanofibers were dispersed in the polymer resin before mixing. The rheological behavior was studied following the same methods depicted in Chapter 4. It was found that the presence of CNFs at very low concentrations (0.5% by resin wt.) has a significant effect on increasing the static yield stress over time. The mechanisms behind this phenomenon are discussed. The compressive strength for cast and 3D printed specimens is also improved by using CNFs.

Materials and Methods

A Novolac epoxy resin (Euclid Chemical, Cleveland, OH) was mixed with 44% Benzyl alcohol hardener (Euclid Chemical, Cleveland, OH) as weight ratio per the manufacturer's recommendation. Pyrogenic fumed silica (Cabot Corporation, Alpharetta, GA) with a hydrophobic surface treatment, a specific surface area of 120 m^2/g, and a density of 2.2 g/cm^3 was mixed with the resin to modify its rheological properties. Medium-graded silica sand with a nominal maximum size of 2.36 mm was used. Figure 30 (Chapter 4) shows the aggregate size distribution used in producing 3D printed PC. This maximum aggregate size was selected to ensure proper printing resolution for the 40 mm nozzle diameter**.**

Class-F fly ash (Salt River Materials Group, Scottsdale, AZ) compliant with ASTM C618-19 [174] with a density of 2.3 g/cm^3 and silica fume (BASF, Florham Park, NJ) with a density of 2.2 g/cm^3 were used as fillers to increase the packing fraction and consequently the mechanical performance. The fly ash to silica fume weight ratio was kept constant at 2:1 for this investigation. Higher fly ash content was used since it has been proven to yield better

`

compressive strength for PC [89]. Different proportions of carbon nanofibers (CNF) were studied to investigate their effect on the rheological properties of PC. The changes in the PC mixes were made such that the polymer (resin and hardener) volume fraction of all the mixes were kept constant. The carbon nanofibers (CNFs) used were supplied by Nanostructured & Amorphous Materials, Inc. (Texas, USA). The diameter rage is comprised in the 50–200 nm range and the length in the 1-15 µm range and thus an aspect ratio in the 6.3-100 range. The purity is greater than 95%, as reported by the manufacturer. A scanning electron microscopic (SEM) picture of the nanofiber provided by the manufacturer is depicted in Figure 37.

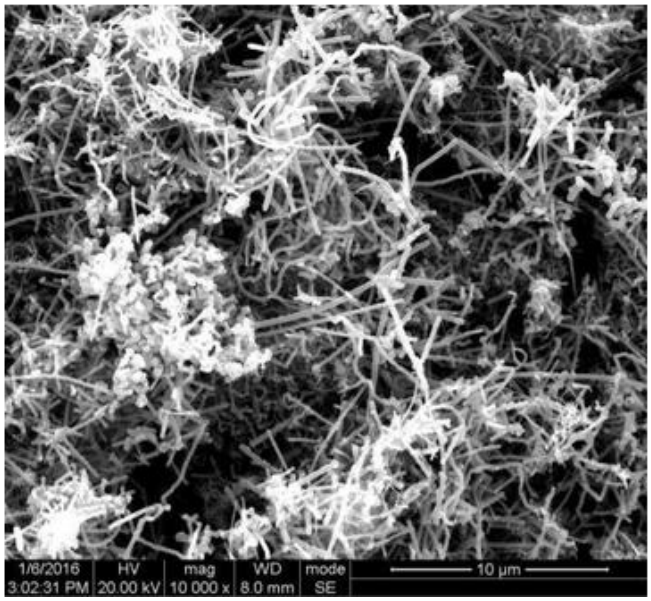

Figure 37. SEM image of carbon nanofiber. Extracted from https://www.nanoamor.com .

Three mix proportions, denoted PC, PCN1, and PCN2, were investigated and are presented in Table 6.

`

Table 6. Mix design and proportions (kg/m^3) for the PC mixtures.

	PC	PCN1	PCN2
Resin		334	
Hardener		149	
Rheology Modifier		23	
Filler		240	
Aggregate		1377	
Carbon Nanofibers (% of resin wt.)	0.0	0.5	1.0
Polymer Weight Fraction %*		23	

1kg/m^3 = 1.6856 lb/yd^3; *Polymer = resin + hardener.

The first mix (PC) is based on previous investigations of 3D printed PC and is denoted herein as the reference mix [175]. Changes were introduced to the reference mix (PC) to investigate the significance of different contents of carbon nanofibers (CNF) on the rheological behavior of 3D printed PC and to develop rheological behavior models to predict the critical rheological parameters necessary for 3D printing of PC as described in Figure 12**.**

PC mixing, CNF dispersion, and Rheology Characterization

A 4.7-liter bowl-lift standard mixer was used for mixing the PC. The stepwise mixing protocol is presented in Table 3**.** Rheology measurements were performed using a Brookfield RST soft solid tester rotational rheometer (AMETEK Brookfield, Middleboro, MA)**.**
The dispersion of the CNFs in the polymer resin matrix for all mixes was performed as follows: first, the CNF were mixed manually in the polymer matrix and then dispersed mechanically by using magnetic stirring followed by ultrasonication. The specific CNF weight (with a tolerance of 0.01g) was added to the polymer matrix. Then the resin was placed in a hot plate with a magnetic stirrer inside an oil bath and heated to 110 ℃. Once the

`

temperature was reached, the hot resin with the CNFs was stirred at 800 rpm for two hours. Then, the solution was placed in an ultrasonication bath (distilled degassed water at 60 ℃). Ultrasonic waves were applied then for two hours. Then the resin was left to cool down before use. The temperature, stirring speed, and ultrasonic length was chosen so that the polymer resin does not suffer any molecular polymer damage while reducing the viscosity to a minimum. This dispersion protocol has been applied by other authors [78,80,188] and has proven to yield a uniform dispersion of the nanoparticles.

For the rheological testing and characterization, the same methods described in Chapter 4 were applied. Five (5) specimens of 68.5 ml volume were tested for the polymer resin at different testing times (0, 15, 30 min). Limiting the test time to 30 minutes was based on prior published work suggesting 30 minutes as the limit for assessing 3D printed concrete [161]. The concrete samples were not pre-sheared before the test to quantify the static yield stress. The material was mixed, as indicated in Table 3, and then collected from the mixer. Five (5) specimens were tested at each time interval (0, 15, and 30 min) for each of the 3 PC mixes, were tested. The specimen's geometry for the rheological test of PC is shown in Figure 31 (Chapter 4). Each sample was tested only once to prevent the material from having a different shear history. Time '0' denotes the time immediately after the mixing process was concluded, as specified in Table 3. The temperature during the test was kept at 23 ±2ºC. The typical hysteresis loop response for the PC is shown in Figure 31 (Chapter 4).

Rheology Modeling

The same analysis depicted in Chapter 4 was applied to analyze the rheological response of the material. To model the rheological behavior of PC, a Bingham pseudoplastic material

`

(Figure 12) was assumed. Details on the implications of this model can be found in detail in Chapter 4.

PC printing, Curing, and Compression Testing

A gantry robot 3D printer with 3 degrees of freedom and a printable area of 6.5 x 6.5 x 6.5 ft (2.0 x 2.0 x 2.0 m) was used. Cube specimens of 1.8 in x 1.8 in x 1.8 in (45 x 45 x 45 mm) were printed for the reference mix PC1 by using a 40 mm diameter nozzle, 10 mm layer height, and 50 mm/s linear printing speed. The temperature during the printing process was kept at 23 ±2 ºC. The extrusion rate represents the rotational speed of the helicoidal extruder that pushes the material through the nozzle (depicted as ω in Figure 14). To print the specimens, it was kept constant at 4 rad/s (19.2 L/min). For the geometry printed and the printing settings reported herein, the build-up rate ($\dot{H}$), defined schematically in Figure 14, is 0.05 cm/s.

The curing of PC differs from cement concrete [84]. PC is not cured in a humid environment since there is no hydration process taking place but is typically cured in a dry air environment at ambient temperature. This is attributed to the fact that curing aims to allowing the polymerization process to continue and be completed. Studies reported that PC achieves compressive strength in the range of 70-75% of its target compressive strength after one day of age [180–182] and most of its strength after seven days of age if cured at ambient conditions (i.e., 21-24 ºC) [183]. Following these recommendations, specimens were air-cured for 7 days at controlled ambient conditions of 23 ±2 ºC and then tested. The compression test of the 3D printed concrete cubes was performed using a Tinius Olsen universal testing machine with a resolution of 1 lbf (4,45 N) and a maximum capacity of 400 Kip (1779 kN). 5 cubes 2.0 in x 2.0 in x 2.0 in (51 x 51 x 51mm) were cast as per ASTM

`

C109/C109M-20b [184]. The compressive strength of standard cubes is compared to the compressive strength of 3D printed cubes of 1.8 in x 1.8 in x 1.8 in (45 x45 x 45 mm) cut from the continuously printed filament and tested in the vertical (Z) direction. The difference in size between the two cubes is negligible, and both specimens satisfy the nominal maximum aggregate size requirement by ASTM C109/C109M-20b [184]. A displacement rate of 0.04 in/min (1 mm/min) was used throughout the test. The compressive strength was calculated as the maximum load obtained during the test divided by the initial cross-sectional area of the specimen.

Results and Discussion

The flow properties of the Novolac epoxy polymer (resin and hardener) and its evolution over time is presented in Figure 33 (Chapter 4).

For the PC, as explained above, the shear stress versus shear rate data in the decreasing part of the hysteresis loop was fitted to a Herschel-Bulkley model. The average coefficient of determination (R^2) of the three mixes at times 0, 15, and 30 min was determined using the least-squares method. The values obtained are 0.98 ± 0.01, 0.98 ± 0.01, and 0.94 ± 0.05, respectively. It should be noted that the model fits very well for all the time periods studied. The consistency (k), flow index (n), and dynamic yield stress (τ_d), the static yield stress (τ_s), and the thixotropy (A_{thix}) are presented in Figure 38.

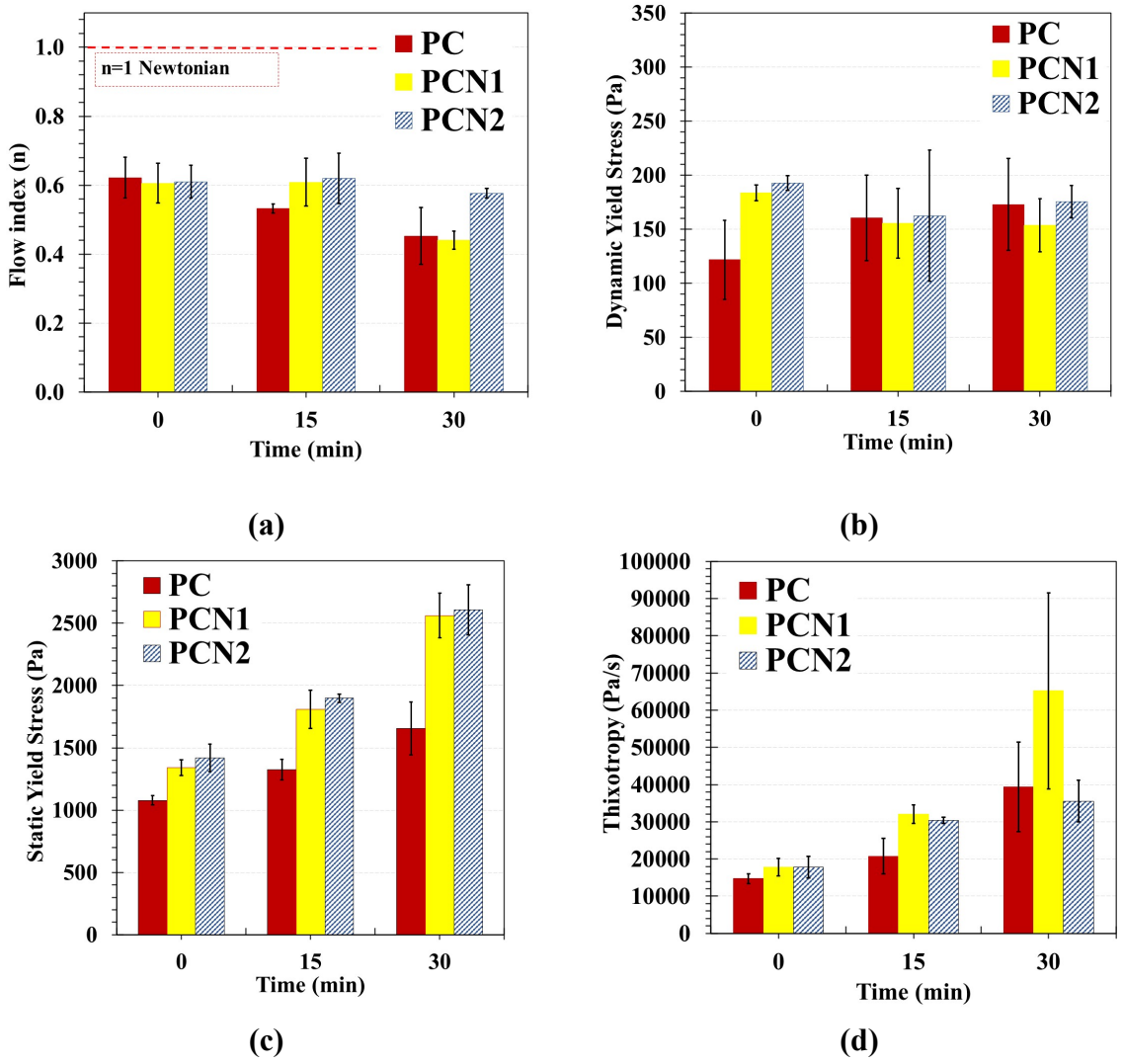

Figure 38. Effect of carbon nanofiber (CNF) on (a) flow index (n); (b) dynamic yield stress (τ_d); (c) static yield stress (τ_s); (d) thixotropy. The time-dependent evolution of the consistency, k(t), and flow index, n(t), was found to be linear. Equation 8 and Equation 9 (Chapter 4) describe the regression models and their nomenclature.

The linear regression variables A, B, C, D are presented in Table 7.

`

Table 7. Time-dependent linear regression for Herschel-Bulkley's parameters 'k' and 'n' to predict the dynamic yield stress of PC with and without CNF.

	PC	**PCN1**	**PCN2**
A	2.042	2.063	1.952
B	60.2	53.4	59.1
R^2	0.99	0.99	0.99

* k(t)=A*t + B

	PC	**PCN1**	**PCN2**
C	-0.00643	-0.00550	-0.00112
D	0.63	0.63	0.62
R^2	0.99	0.74	0.55

* n(t)=C*t + D

No significant difference was found at any given time for the flow index (*n*) for all the different mixes. This behavior is depicted in Figure 38 (a). The shear-thinning behavior of the PC can be attributed to the disentanglement of the polymer chains and alignment in the direction of the flow. This rearrangement would facilitate shearing by reducing the particle-matrix interactions (Figure 13), decreasing the apparent viscosity.

The dynamic yield stress is shown in Figure 38 (b). It seems to be time-independent of the mix design variables studied for each mix. Nonetheless, for time 0, it can be observed how the dynamic yield stress is statistically significantly higher for the mixes containing CNFs. This could be attributed to the potential physical resistance to flow that the CNFs could impose due to its high aspect ratio. The range of values observed was similar to those reported by others for cement-based 3D printing concrete [114,161]. The evolution of the

`

static yield stress with time is shown in Figure 38 (c). Traditionally, for cement-based materials, the rate is constant with time, as suggested by [55,56], and the static yield stress of the material after a resting time '*t*' can be calculated using Equation 10 (Chapter 4). For PC, the static yield stress was found to grow exponentially with time. The model suggested in Equation 10 predicts the static yield evolution with time. The fitting curve parameters (*E* and *F*) for each one of the 7 PC mixes are presented Table 8**.**

Table 8. Time-dependent exponential regression model for the static yield stress of PC with and without CNF.

	PC	**PCN1**	**PCN2**
E	1037.8	1329.3	1413.8
F	1.018	1.022	1.02
R^2	0.97	0.99	0.99

* $\tau_s(t) = E * F^t$

It is worth mentioning that E and F are independent of the shear rate, shear stress and its evolution over time. Therefore, the static yield stress's proposed equation is independent of the testing device and protocol used. Values within the same range are also reported for cement-based 3D printing concrete [43,114,161]. It can be observed how the increase from 0.5% to 1% CNF content does not seem to have a significant effect on the static yield stress. Nonetheless, the use of 0.5% CNF does provide a statistically significant increase in the static yield stress for all tested times. The time-dependent exponential growth of the static yield stress of PC is beneficial to ensure the stability of the 3D printed geometry as it allows to conduct the printing at a relatively high rising speed.

`

The inclusion of carbon nanofiber (CNF) at low percentages (0.5%) improves the static yield stress significantly. The difference between the use of 0.5% or 1% CNF content does not make a significant difference in the rheological behavior of the mix. Due to its high surface area and aspect ratio, the presence of CNF seems to have a significant effect on increasing the static yield stress but not on the dynamic yield stress. Similar effects were observed and reported in ultra-high-performance concrete by other researchers [189]. Before flow starts (solid regime), the fibers are dispersed randomly within the polymer matrix. When a shear rate is imposed between two particles, the CNFs tend to align with the flow direction. As the material transitions between the solid and liquid regime, the shear stress required to initiate the flow (static yield stress) increases due to the presence of the CNFs. Once the material is in a flow state, the CNFs are aligned with the flow direction, and therefore the dynamic yield stress is barely affected by their presence. The mechanisms behind this effect only on the static yield stress is summarized in Figure 39.

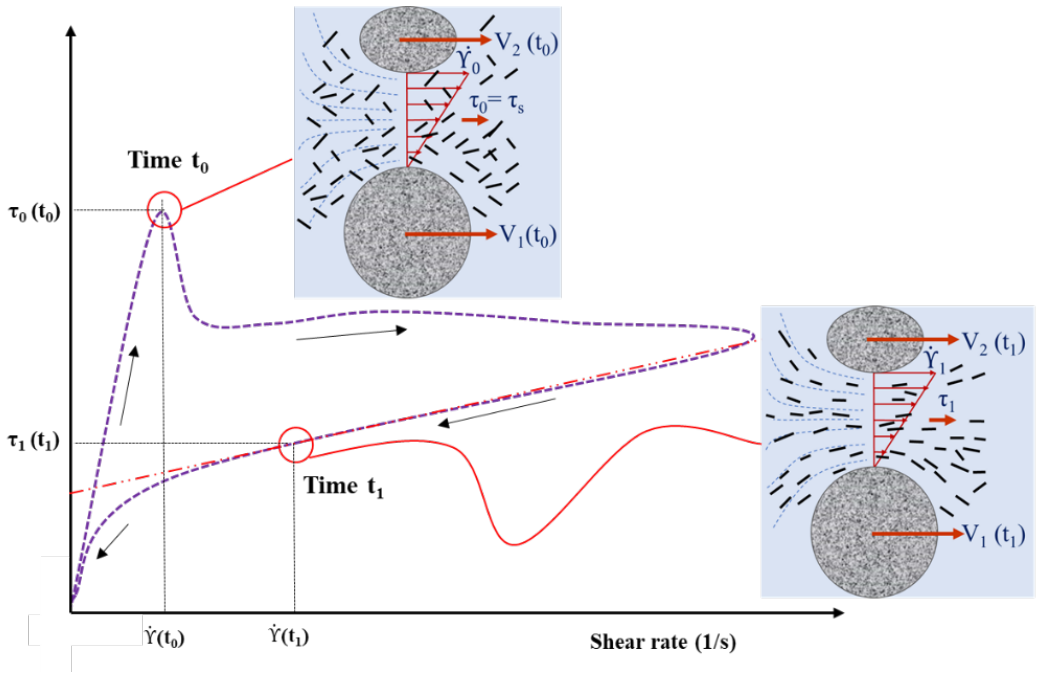

Figure 39. Alignment of the CNF with the direction of the flow.

`

The thixotropy increases with time for all mixes up to 30 min. The thixotropic behavior for all the mixes is governed by the Novolac polymerization, as depicted in Figure 14. This explains why it increases at a similar rate for all the mixes. The magnitude of the thixotropy values is similar to that reported for cement-based 3D printed concrete [114].

The average compressive strength of PC1 was 3913.6 ±88.4 psi (27.0±0.61 MPa) for the cast specimens and 4507.2 ±269.6 psi (31.1±1.86 MPa) for the 3D printed specimens (PC1). For the PCN1 mix, the average compressive strength for the cast specimens is 4240.7±191.6 psi (29.2±1.3MPa), and for the 3D printed one, 4780.2±269.5 psi (33.0±0.5MPa). The difference between printed and not printed is statistically significant (*T-test,* α=0.05) for both mixes, showing the 3D printed PC to have slightly higher strength than conventional cast concrete. The slight improvement in the compressive strength might be attributed to the low slump of the PC mix designed for 3D printing, making it not suitable for conventional casting. Moreover, the nozzle pressure during the printing of 3D printed concrete results in slight compaction that tends to improve the compressive strength [114]. Also, it can be observed how the use of CNF improves the compressive strength for both manufacturing techniques (cast and 3D printed). This difference is statistically significant (*T-test,* α=0.05) but probably not significant enough for practical application given the relatively high cost of CNF. The compressive strength results for PC and PCN1 mixes are reported in Figure 40.

`

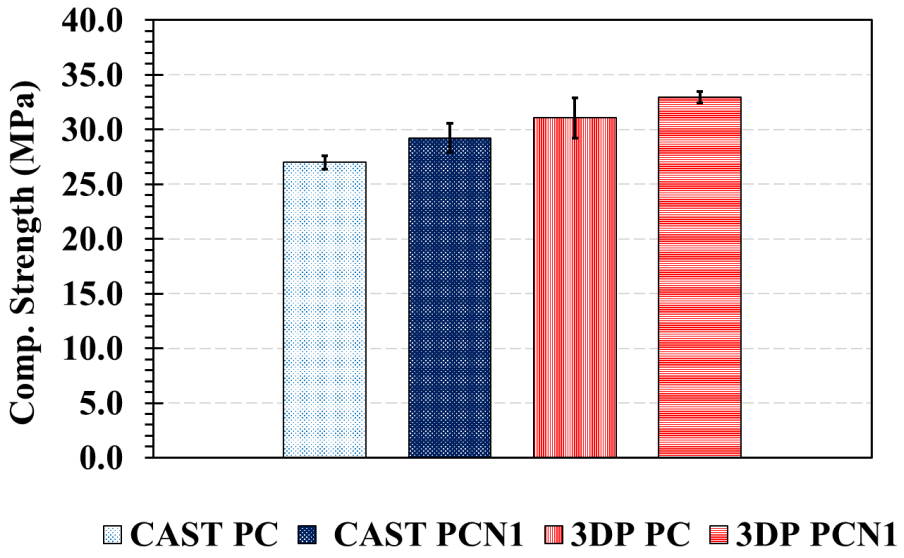

Figure 40. Compressive strength results for PC and PCN1 mixes (MPa).

The above investigation demonstrates the potential use of carbon nanofiber (CNF) for PC 3D printing as a static yield stress modifier. Simple models can be developed to predict the static yield stress evolution over time to ensure efficient and stable 3D printing.

`

Chapter 6. Textile Reinforcement as an Alternative Reinforcement for 3D Printing Applications

Textile reinforced concrete (TRC) has gained attention from the construction industry due to its lightweight, high tensile strength, design flexibility, corrosion resistance, and remarkably long service life. Some structural applications that utilize TRC components include precast panels, structural repair, waterproofing elements, and façades. TRC is produced by incorporating multiple textile fabrics into thin cementitious concrete panels. Premature debonding between the textile fabric and concrete due to improper cementitious matrix impregnation of the fibers was identified as a failure-governing mechanism. In this chapter, a new type of TRC is proposed to overcome this performance limitation by replacing the cement binder with a polymer resin to produce textile reinforced polymer concrete (TRPC). The new TRPC is created using a fine-graded aggregate, methyl methacrylate polymer resin, and basalt fiber textile fabric. Four different specimen configurations were manufactured by embedding 0, 1, 2, and 3 textile layers in concrete. Through 3-point bending tests, flexural performance was analyzed and compared with reference TRC specimens with similar compressive strength and reinforcement configurations.

Furthermore, the crack pattern intensity was determined using an image processing technique to quantify the ductility of TRPC compared with conventional TRC. TRPC showed significantly improved flexural capacity, and superior ductility and substantial plasticity compared with TRC. It is evident that TRPC represents an excellent new material for civil infrastructure applications.

The TRPC is produced using basalt fiber textile fabrics, well-graded fine aggregate, and Methyl Methacrylate (MMA) polymer as a binder. This is the first study to examine this type

of concrete to the best of the authors' knowledge. Flexural testing was conducted on TRPC with different reinforcement configurations. The flexural capacity, ductility, toughness, and the crack pattern of TRPC were quantified and compared with conventional TRC fabricated using Portland cement concrete of similar strength and with the same textile fabric and reinforcement configurations.

Experimental Methods

Materials

MMA polymer (by Transpo Industries, New Rochelle, NY, USA) was used to produce PC. The polymer system consists of two parts: a low viscosity MMA monomer resin and a Benzoyl Peroxide as an initiator. Type I/II Portland cement and a water/cement ratio of 0.25 were used for the conventional concrete mix. BASF Master Glenium 3030 (BASF, Florham Park, NJ, USA) superplasticizer was used with the conventional concrete mix. A well-graded fine quartz aggregate with a nominal maximum size of 2.36 mm was used for both cement concrete and PC mixes. The aggregate size distribution is depicted in Figure 41.

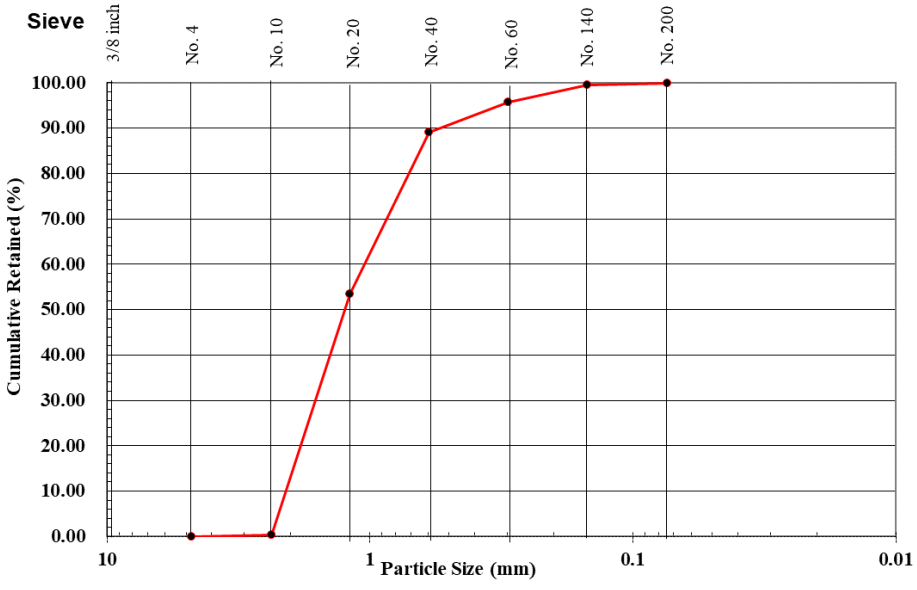

Figure 41. Sieve size distribution for aggregate used in both TRC and TRPC mixes.

`

The nominal maximum size of the aggregate needed to be smaller than the 5 mm window size of the textile fiber fabric to ensure proper impregnation. The concrete mix proportions for both the PC mix and the reference conventional concrete mix are presented in Table 9. As per ASTM C1437-20 [190], the flow values for both TRC and TRPC mixes are 113% and greater than 160%, respectively. The cement concrete reference specimens were cast and cured in a standard curing room at 99% relative humidity (RH) and 22 ºC for 28 days to reach the design strength. Studies reported that PC achieves about 75% of its strength within one day of curing [180–182] and 90% of its full strength after seven days of curing in such ambient temperatures [183]. PC was therefore left to cure in the lab ambient conditions of 30% RH and 22^{o}C for seven days [84]. Five cylinders, 2 in (50.8 mm) diameter by 4 in (101.6 mm) height, of each mix were cast to determine the compressive strength of conventional concrete and PC as per ASTM C39-17b [191]. The mean compressive strength for the conventional reference concrete after 28 days was 68.9 ± 5.1 MPa, and the average compressive strength of PC mixture after seven days was 53.9 ± 5.8 MPa. The cement-based concrete mix was intentionally designed to have similar or higher compressive strength than the polymer-based mix to ensure fair comparison. A bidirectional planar basalt fiber textile mesh (Smarter Building Systems, New Port, Rohde Island, USA) was used for the reinforcement of both TRC and TRPC specimens. The textile reinforcement material was selected for being a sustainable material derived from natural resources (e.g. Basalt), being eco-friendly, and for having resistance to high temperatures, high water absorption, good mechanical properties, corrosion free, high adhesion to cement matrix, high resistance to sea water and chemicals and aggressive environment compared with other textile reinforcement

`

materials. The characteristics of the basalt fiber textile mesh, as reported by the manufacturer, are presented in Table 10.

Table 9. Concrete mixture proportion (kg/m^3) for the reference conventional concrete and PC

	Reference Conventional Concrete	PC
Portland Cement	689	---
Water	172	---
Superplasticizer	21	---
Aggregate	1378	2002
Polymer Resin	---	251

Table 10. Geometry, density, and mechanical characteristics of basalt fiber textile mesh

Window Size	5.00 mm	Maximum Load-Weft	45,000 N/m
Total Weight/ Area	220 g/m^2	Elongation at break-Warp	6.7 %
Weight Resin Coating	No resin coating	Elongation at break-Weft	3.5 %
Thickness	0.6-0.7 mm	Breaking Elongation-Warp	13.5 mm
Maximum Load-Warp	48,000 N/m	Breaking Elongation-Weft	7.1 mm

Mixing and Casting

TRC and TRPC mixtures were mixed using the proportions described above and following standard concrete mixing protocol. Both mixes were mixed for 3-5 minutes using a 4.7-liter bowl-lift standard mixer until a uniform mixture is obtained. TRC and TRPC panels of 400 x

144 x 20 mm (length, width, and thickness) were cast using the conventional concrete or PC mixture, respectively, and the basalt fiber textile fabrics described above. Four configurations of TRPC panels were fabricated by incorporating 0, 1, 2, and 3 layers of basalt fabric denoted as TRPC-0, TRPC-1, TRPC-2, and TRPC-3 respectively. The same reinforcement configurations were used to fabricate the reference TRC panels, denoted as TRC-0, TRC-1, TRC-3, and TRC-3. Figure 42 illustrates the configurations of TRPC and TRC panels.

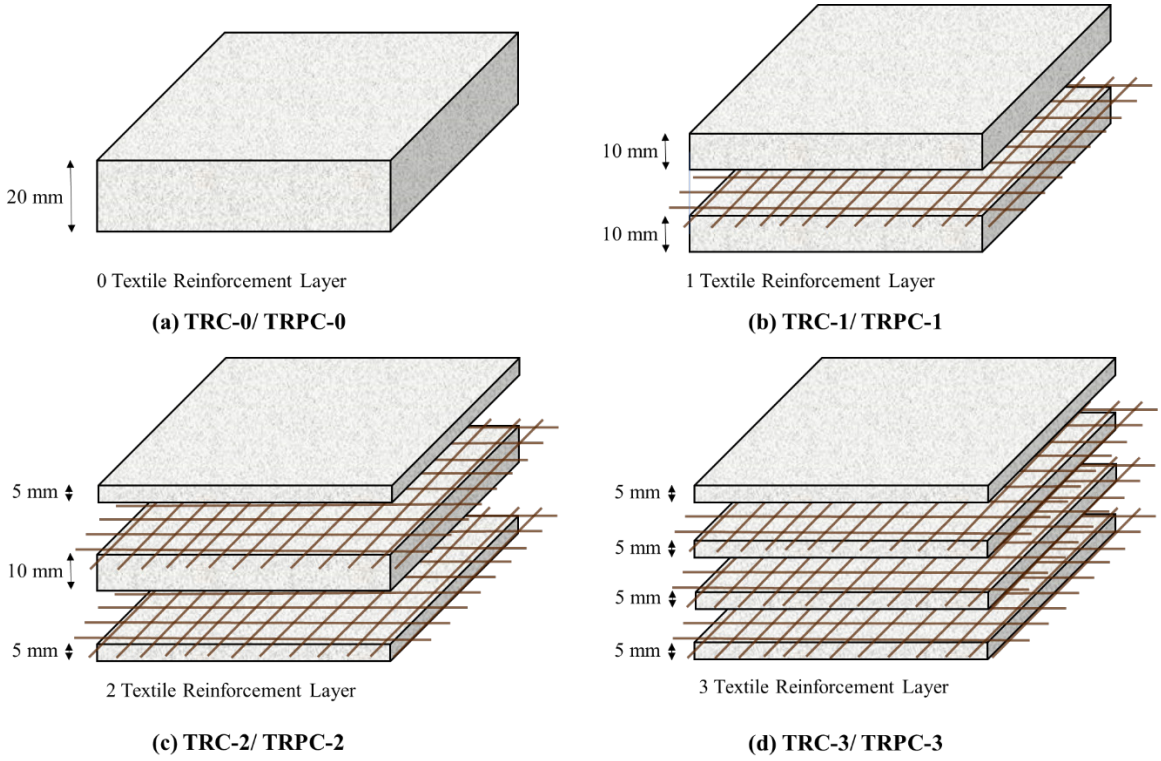

Figure 42. Schematic representation of the fabricated TRC and TRPC panels incorporating zero (a), one (b), two (c), and three (d) basalt fiber textile reinforcement layers.

All TRC/TRPC panels, regardless of the number of textile reinforcement layers used, were cast in four layers following a layer-by-layer method. A layer of fresh concrete (or PC) was placed first, and the basalt fiber textile fabric was placed at the desired thickness location afterward. The second layer of fresh concrete (or PC) was cast, and the process was repeated

`

until the total thickness of the specimen was obtained. Figure 43 shows the fabrication setup of the TRPC panels. All TRC and TRPC panels were demolded after 24 hours and then cured using the two curing protocols of 28 days in 99% RH for conventional concrete and seven days in 30% RH for PC as described above.

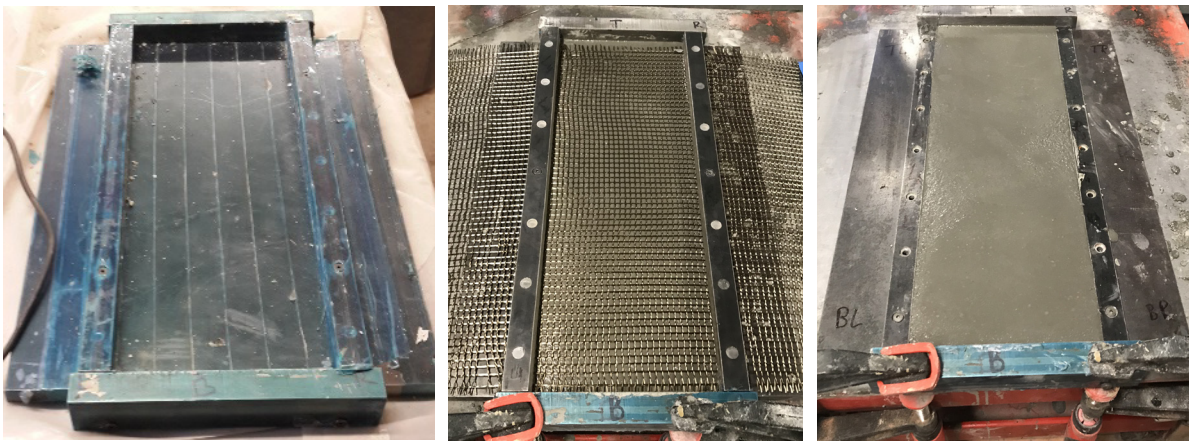

Figure 43. Process for the fabrication of TRC and TRPC panels. Left. Mold. Middle. Addition of an intermediate basalt fiber textile fabric above the concrete or PC layer. Right. TRC panel after fabrication.

Flexure Test Setup

The TRC/TRPC panels were cut into 400 mm x 35 mm x 20 mm (length x width x thickness) prisms using a waterjet cutting machine. The prisms were tested in three-point bending with a span length of 330 mm, achieving a span-to-depth ratio of 16.5. The deflection at the midspan location was measured using a linear variable differential transducer (LVDT). The load and displacement of the load cell were also recorded using MTS® Bionix servo-hydraulic system with a range of 0-25 kN and a resolution of 1 N. For testing, a displacement rate of 0.5 mm/min was imposed at the mid-span location. Three specimens were tested for

each TRC/TRPC reinforcement configuration. The test setup is shown in Figure 44(a). The three-point bending test setup included the digital image acquisition system to capture crack patterns during testing. The crack pattern intensity was quantified via digital image processing technique to assess the ductility of TRC/TRPC. Photoshop® and ImageJ® software were employed for examining the cracking pattern. Details for the method used for image transformation and processing have been described elsewhere [192]. Two types of cracks were analyzed, horizontal and vertical cracks, to assess the flexural ductility and the concrete-fabric bond strength. Figure 44 (b) shows the digital image data acquisition.

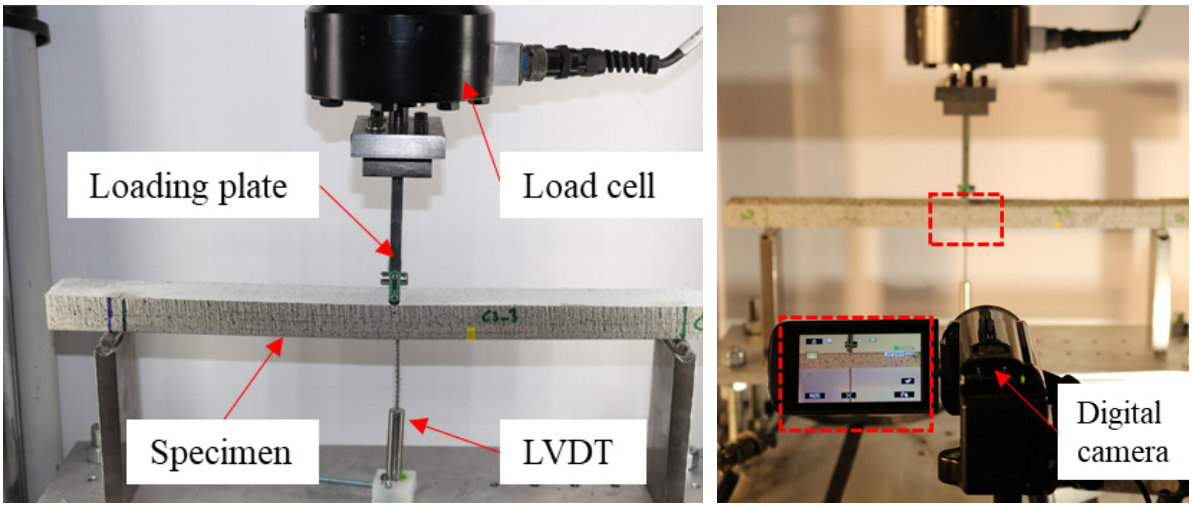

(a) **(b)**

Figure 44. Three-point bending test setup. (a) Specimen during testing and LVDT displacement recording system; (b) Digital image data acquisition system.

Results and Discussion

The median load-deflection curves of the three-point bending tests of TRC and TRPC specimens with different textile layers are shown in Figure 45. The mean flexural strength, deflection at maximum load, and toughness (energy absorption up to a post-peak residual capacity of 25% of the maximum load) of TRC and TRPC for the different reinforcement

configurations are presented in Figure 46. Similar mechanical properties (flexural strength in the order of 6.0 to 8.0 MPa) for TRC were reported by other researchers [140].

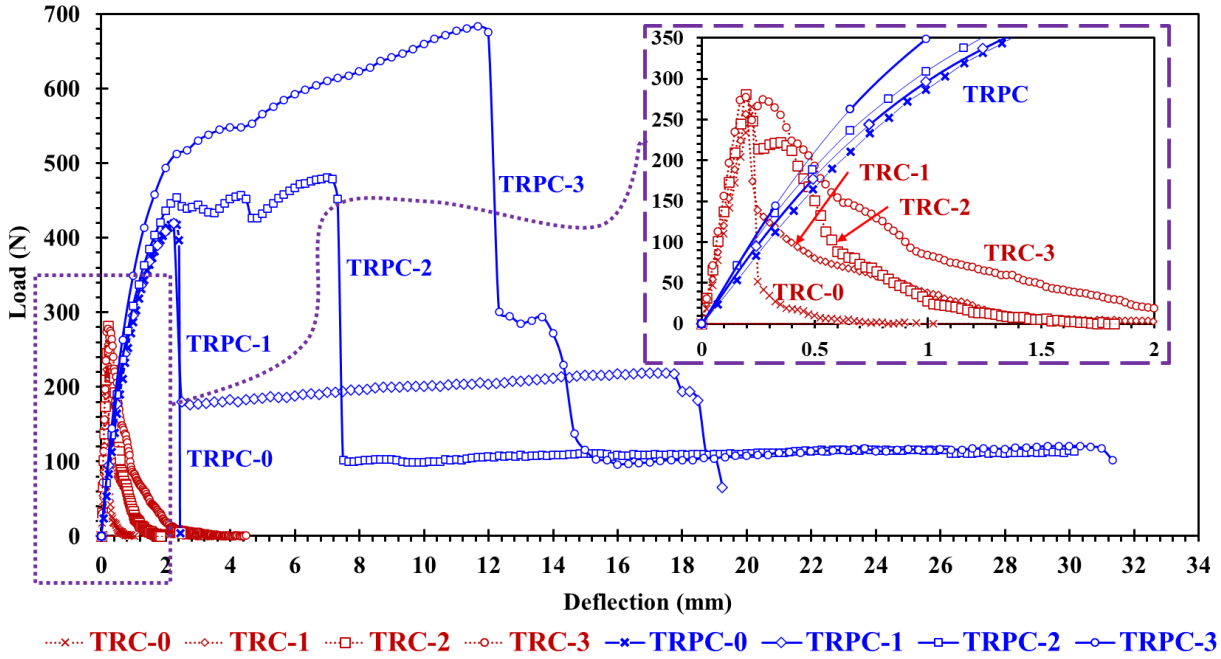

Figure 45. Load-displacement response of TRPC specimens with the different number of textile layers compared with TRC. Three specimens were tested for each case. One median test specimen is shown for each type for clarity. Inset shows a close-up to show the behavior of TRC.

Figure 45 and Figure 46 show the superior mechanical performance of TRPC in terms of flexural strength, deflection at peak load, and toughness for all the TRPC specimens compared with conventional TRC. The improvement in the mechanical behavior can be attributed to the higher tensile capacity and ductility of the polymer (as depicted by comparing TRC-0 to TRPC-0) and its better bond with the basalt fibers compared with cement paste. The figures also demonstrate the fact that the behavior of reinforced and unreinforced TRPC specimens is significantly different compared with TRC. For instance,

`

for TRC specimens, the addition of textile reinforcement layers did not significantly affect the flexural strength or deflection at peak load. This can be explained by the limited bond strength between the fibers and the cementitious matrix due to the high viscosity of the cement slurry, and consequently, the low penetrability of the cement matrix to the fiber mesh. On the other hand, the difference in terms of toughness for the TRC configurations is statistically significant (*t*-test, $\alpha=0.05$) due to the difference in post-peak behavior between the reinforcement configurations.

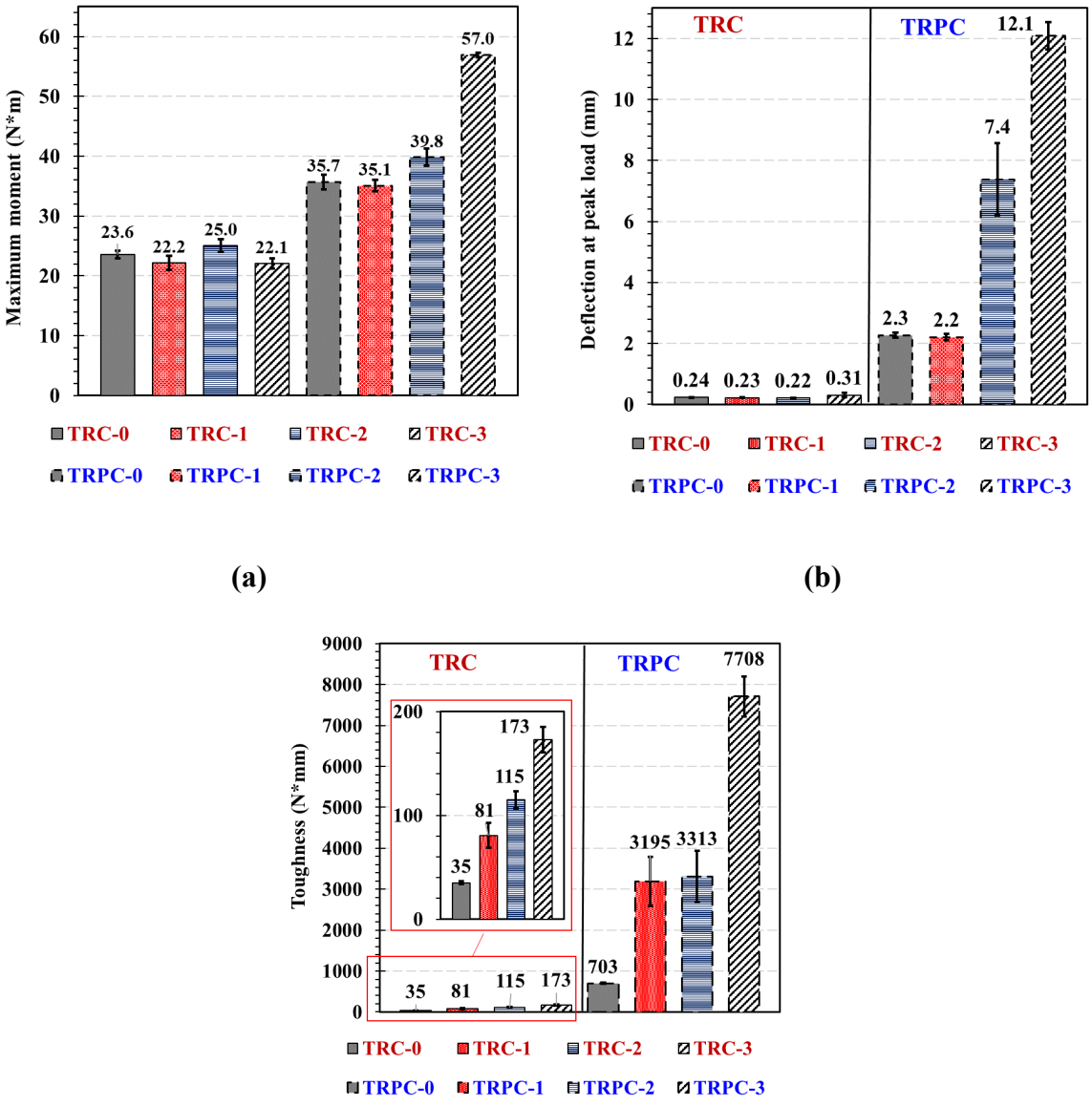

Figure 46. (a) moment, (b) deflection at maximum load, and (c) toughness, measured up to a post-peak residual capacity of 25% of the maximum load for TRC and TRPC with different textile reinforcement layers.

The addition of two and three textile layers in the TRPC specimens significantly increased the maximum moment compared with TRPC-0. The use of two and three layers of basalt textile fabric improved the maximum moment of TRPC-2 and TRPC-3 by 11.5 % and

`

59.5%, respectively, compared with TRPC-0. Similar behavior is observed for the deflection at peak load, which increased by 225% and 432% for TRPC-2, and TRPC-3, respectively, compared with TRPC-0. Statistical analysis shows that the difference in performance for TRPC-1 compared to TRPC-0, in terms of maximum moment, is not statistically significant (*t*-test, α=0.05). This is due to the low efficiency of the reinforcement when placed at the neutral axis position at the mid-height. Nevertheless, the post-peak behavior is significantly improved, as shown in Figure 45 and reflected in the toughness depicted in Figure 46 (c).

To assess the effect of fabric layers on the post-peak mechanical behavior of the panels, the flexural toughness was quantified and compared. The results show significant improvement of TRPC energy absorption by 354%, 371%, and 996% with the addition of one, two, and three basalt-fiber layers. The significant improvement in ductility/energy absorption depends on the improved load and deflection capacity and depends on the TRPC panels' ability to continue carrying the load after exceeding the maximum capacity. Figure 45 shows that as the number of fabric layers increase, the residual load capacity of TRC/TRPC increases. For TRC, the toughness also improves as the number of basalt-textile layers is increased. The use of 1, 2, and 3 layers of basalt fiber textile fabric resulted in improving the toughness of TRC-1, TRC-2, and TRC-3 by 131%, 228%, and 394%, respectively, compared with TRC-0. It is apparent that the improvement in toughness for TRC is much more limited compared with TRPC. It is also evident that the mechanical behavior of TRPC outperforms TRC for all the reinforcement configurations.

The crack pattern in TRC and TRPC specimens was analyzed using a digital image correlation system (DIC) for both horizontal and vertical cracks to assess cracking intensity and ductility. Crack pattern analysis results for horizontal and vertical cracks are presented in

`

Table 11 and Table 12. Moreover, examples of crack patterns for different TRC and TRPC specimens are shown in Figure 47.

Table 11. Horizontal crack length and width (mm) for TRC and TRPC (Mean values).

Specimen	Horizontal crack length *	Horizontal crack width*
TRC-0		
TRC-1		
TRC-2	No horizontal crack	
TRC-3		
TRPC-0		
TRPC-1	34.6	0.24
TRPC-2	51.3	0.45
TRPC-3	27.5	0.75

* Coefficient of variation (CV<0.5) for all samples.

Table 12. Vertical crack area (mm2) and width (mm) for TRC and TRPC (Mean values)

Specimen	Vertical crack area*	Vertical crack width*
TRC-0	4.28	0.39
TRC-1	9.46	0.58
TRC-2	13.42	0.65
TRC-3	17.81	0.85
TRPC-0	4.8	0.29
TRPC-1	27.0	1.04
TRPC-2	42.7	1.84
TRPC-3	113.8	2.40

* Coefficient of variation (CV<0.5) for all samples.

`

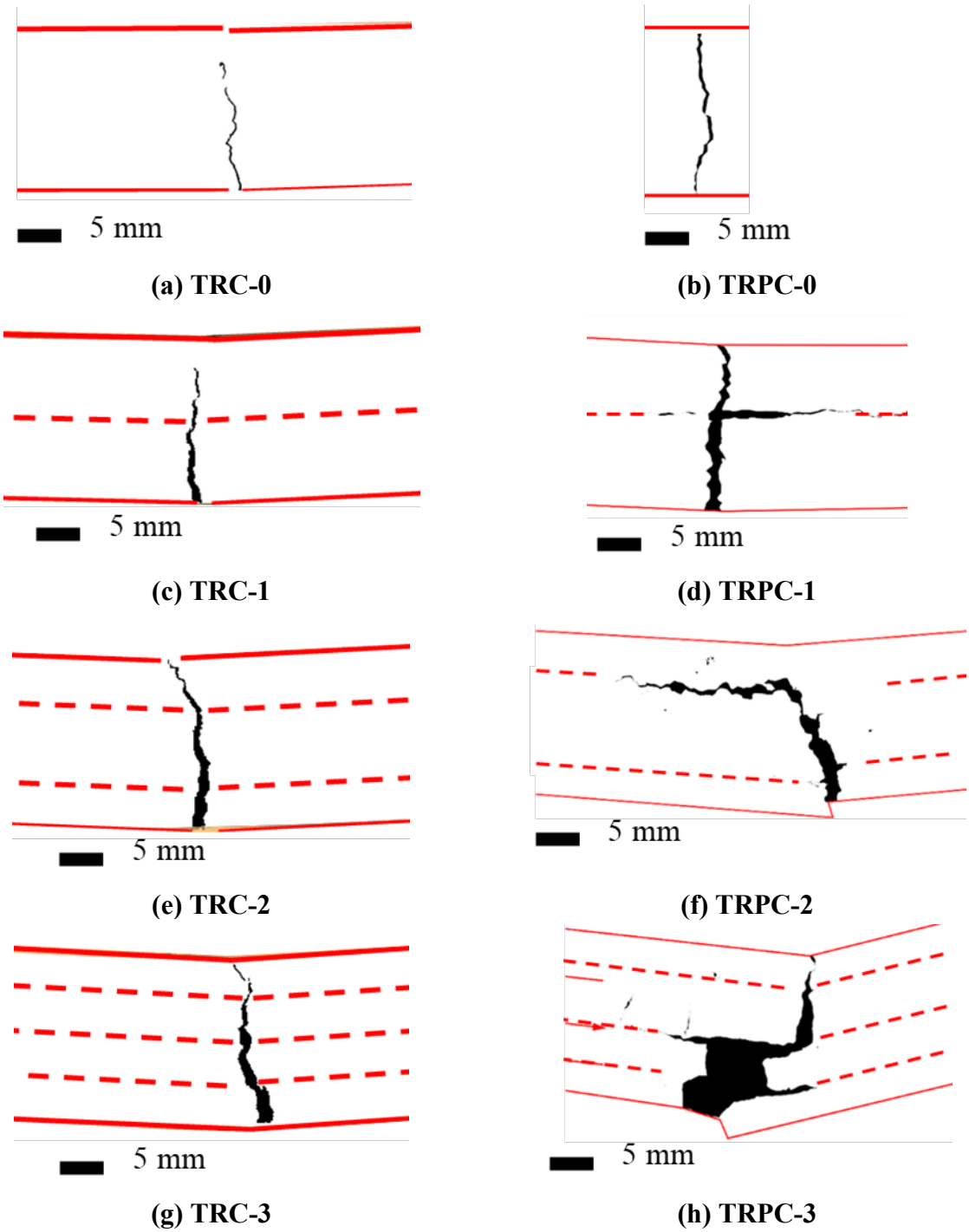

Figure 47. Cracking pattern for TRC and TRPC specimens with different reinforcement configurations recorded using DIC on the side of the specimens. Red continuous lines represent the contours of the specimens. Dotted marked lines represent the location of the

`

textile reinforcement. (a) TRC-0 (b) TRPC-0 (c) TRC-1 (d) TRPC-1 (e) TRC-2 (f) TRPC-2 (g) TRC-3 (h) TRPC-3.

Table 11 and Figure 47 show that no horizontal cracks were observed for all TRC reinforcement configurations and TRPC-0 configurations. This indicates that the vertical cracks grow relatively unrestricted with the absence of intermediate reinforcement. This is also an indication of the relatively low plasticity of TRC and TRPC without any textile reinforcement due to the absence of a mechanism to divert and deviate crack propagation. On the other hand, horizontal cracks were observed in all TRPC specimens incorporating textile reinforcement. The propagation of horizontal cracks delayed failure and thus provided additional plastic and ductile behavior. The presence of horizontal cracks might be influenced by the interface debonding due to the chemical adhesion between the textile yarn and the matrix. The development of horizontal cracks also demonstrates the ability of the textile fabric to improve fracture toughness for TRPC specimens compared with conventional TRC. The resistance to crack extension could be attributed to the good bond strength between the basalt textile fabric and PC. In TRC, the limited bond strength between the basalt textile fabric and cement matrix leads to lower cracking strength, resistance to crack propagation, and flexural capacity compared with TRPC. It is also apparent that the width of horizontal cracks depends on the number of textile reinforcement layers for the TRPC specimens. As the number of textile layers increased, the average crack width increased, demonstrating the ability of TRPC to sustain residual load while having a considerable level of damage in the specimen. For instance, the average crack width of TRPC-2 was 0.45 mm, which is about twice the average crack width of TRPC-1 of 0.24 mm,

`

and the average crack width of TRPC-3 was 0.75 mm, which is about three times that of TRPC-1.

The assessment for vertical cracks is presented in Table 12. It can be observed that the average vertical crack width increases as the number of fabric layers increase for both TRC and TRPC systems. The crack area also increased by increasing the number of textile layers. It is worth mentioning that TRPC-3 observed an average width of vertical crack of 2.4 mm, 8 times the average crack width of 0.29 mm observed for TRPC-0. Also, the crack area of 113.8 mm^2 for TRPC-3 was about 24 times of 4.8 mm^2 observed for TRPC-0. The use of three layers of basalt fiber provided superior strength and ductility to TRPC.

It is remarkable to compare the performance of TRPC cracking in terms of vertical crack width and area to that of TRC. The vertical crack width for TRPC-1, TRPC-2, and TRPC-3 is 79%, 183%, and 182% higher than the vertical crack width observed for TRC-1, TRC-2, and TRC-3 respectively. The vertical crack area for TRPC-1, TRPC-2, and TRPC-3 is 185%, 218%, and 538%, respectively, higher than the vertical crack area observed for TRC-1, TRC-2, and TRC-3. It is important to note that the cement-based mix has a compressive strength 28% higher than the polymer-based mix. However, TRPC shows a much-improved flexural behavior regarding vertical cracking for all reinforcement configurations compared with TRC. This is due to the high tensile strength and ductility of TRPC. To further understand the failure mechanisms of TRPC and TRC, images of failed specimens were analyzed, as shown in Figure 48.

`

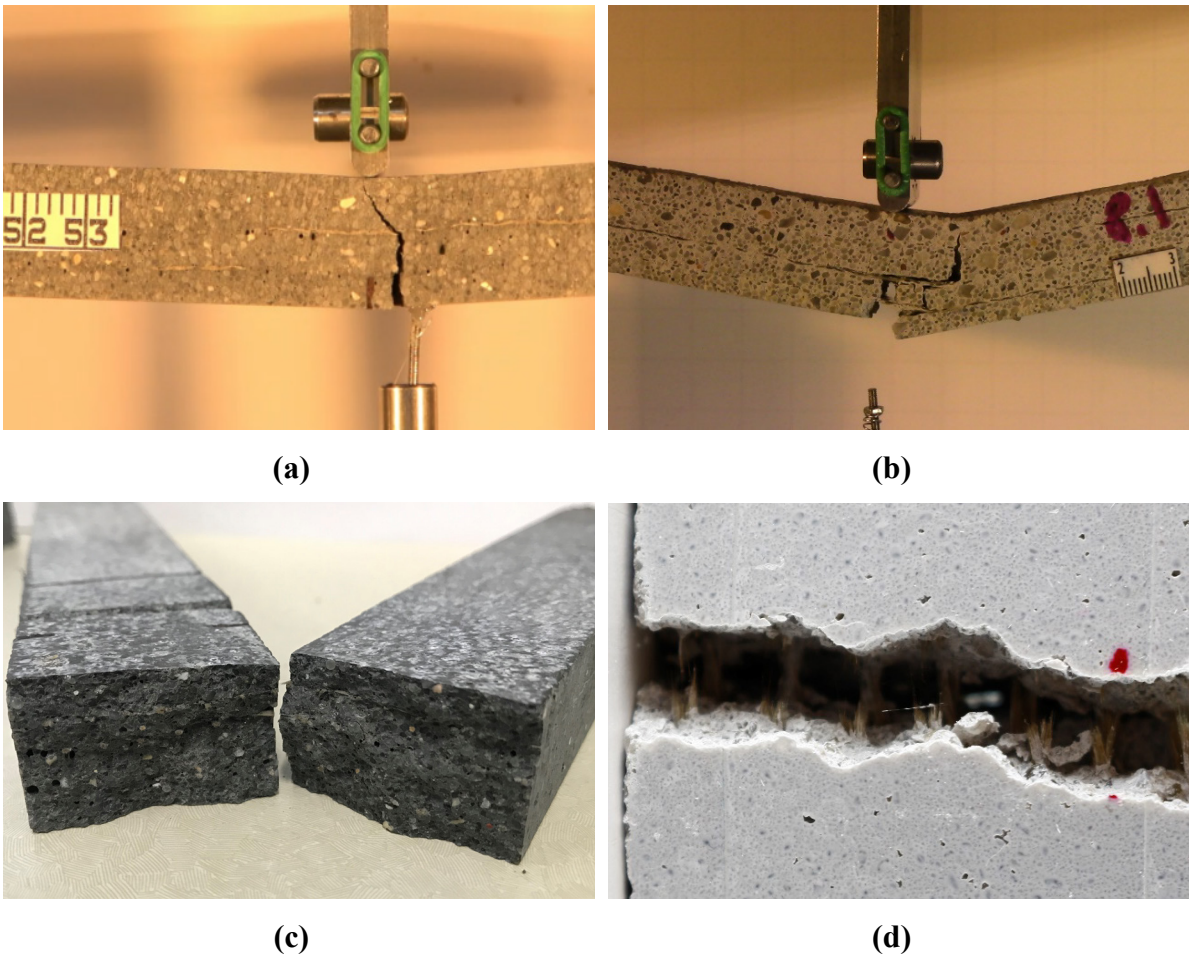

Figure 48. (a) Brittle failure of TRC-3. (b) Ductile failure of TRPC-3. (c) Close-up image of the side view of TRC-3 specimen after failure showing fiber yarn failure. (d) Close-up image of a bottom view of the TRPC-3 showing rupture of fiber yarns leading to the formation of wide cracks in TRPC.

The difference in failure mechanisms between TRC and TRPC is shown in Figure 48 (a)–(b). The images show that a vertical crack propagated the whole depth of textile-reinforced TRC. However, the textile reinforcement in TRPC managed to divert the crack and results in a horizontal crack that allowed the specimen to continue carrying loads while demonstrating a plastic behavior. The progressive crack propagation in the case of TRPC is also evident from the load-displacement curves shown in Figure 45. Figure 48(c)–(d) show close-up images of

`

the failure location of TRC-3 and TRPC-3, respectively. The fiber bridging mechanism in TRPC has contributed to improving the load-carrying capacity, deformation capacity, ductility, and plasticity of the TRPC panels. It is hypothesized that the strong fiber bridging and yarn failure in TRPC stems from a good bond strength between the textile fabric and the polymer matrix compared with the weak bond between the textile fabric and the cement matrix as reported by others in TRC [152]. To investigate this behavior, sagittal cuts using a precision saw with a wafering diamond blade were made in the intact and uncracked sections of the beam specimens. The specimens at the interface between the textile and matrix were analyzed using light microscopy. The light microscopic pictures of the sections for TRC and TRPC specimens for three different resolutions are depicted in Figure 49.

`

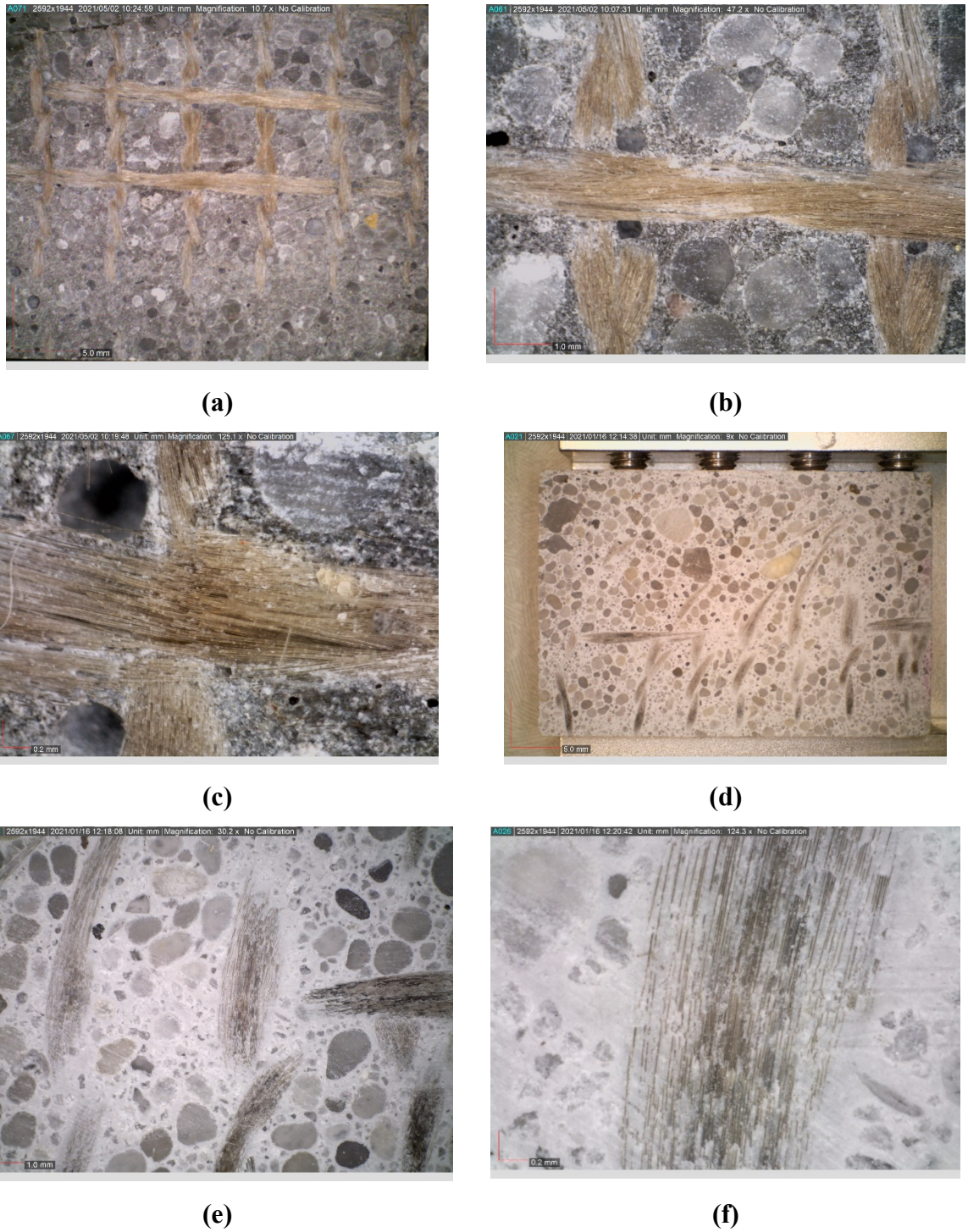

Figure 49. Light-microscopy pictures at a sagittal cut (through the textile-matrix interface) at three different resolutions (macro to micro-scale with left bottom corner image bar showing 5.00 mm, 1.0 mm, and 0.2 mm) for TRC (a, b, and c) and TRPC (d, e, and f).

`

It can be observed from the above images how for the TRPC composite, the polymer impregnates the fiber yarns very well (Figure 49 (f) compared with TRC (Figure 49 (c)), where an apparent absence of impregnation can be observed. The ability of the fresh slurry to impregnate the textile fabric is apparently a critical factor that affects the bond strength between the polymer or cement matrix and the textile fabric. It is evident that the polymer material has a much higher flowability (>160% as per ASTM C1437-20 [38]) than the cement paste (113% as per ASTM C1437-20 [38]), which results in much-improved impregnation of the polymer to the textile fabric compared with the cement paste. This concept is schematically presented in Figure 50. Previous research showed that improper impregnation of textile fabric associated with the use of cementitious matrix in conventional TRC caused properly impregnated outer fiber filaments and poorly impregnated central filaments [149,150]. The improper impregnation of fiber filaments leads to reduced contact surface area between the matrix and the fibers, limiting the bond strength and resulting in limiting the fibers' ability to bridge cracks. Fiber debonding rather than fiber rupture becomes the primary failure mechanism in TRC. In contrast with TRPC, the polymer's low viscosity and high wettability compared with cement result in proper textile fabric impregnation. Good impregnation of the textile fibers improves the bond strength and leads to improved fiber crack bridging and enhanced flexural strength and resistance to crack propagation. Basalt yarn rupture is shown in Figure 48(d) as proof of the relatively high bond of basalt textile and the polymer matrix. The improved impregnation and bond also allow the TRPC to make use of the polymer matrix's high failure strain, thus resulting in significant improvement in TRPC ductility compared with TRC. The above difference in impregnation and bond between the matrix and the textile fabric results in a difference in stress transfer in TRPC compared with

`

TRC. In TRC, shear forces are typically transferred between the fibers and cementitious matrix via friction due to poor adhesion. On the other hand, TRPC relies on the superior adhesion between fibers and the polymer matrix to transfer the shear forces and stress transfer through friction.

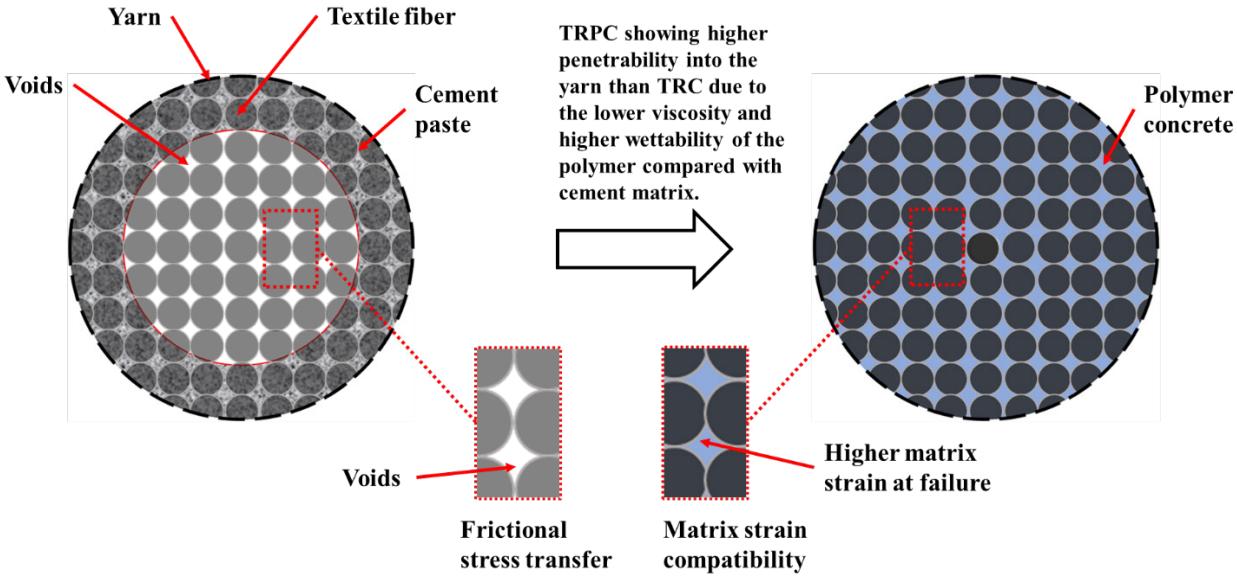

Figure 50. Leading factors affecting the mechanical behavior at the matrix-yarn interface for TRC/TRPC composites.

The above experimental investigations showed the improved flexural performance of TRPC represented by improved strength and superior ductility and plasticity compared with TRC. Limitations of the above study include the absence of test data related to the direct tension behavior of TRPC compared with TRC. Further research is also warranted to identify the optimal location and number of the textile fabrics in the composite. Furthermore, the significance of the fiber types or density was not examined. Other types of less expensive fibers than basalt fibers (e.g., bamboo fibers) should be studied. Finally, the ability to combine basalt fibers and sustainable polymers to produce a new sustainable TRPC should be considered in future research.

`

Chapter 7. Textile Reinforced 3D Printed Concrete and Polymer Concrete

Textile reinforcement is highly amenable with additive manufacturing technology for both in-plane and out-of-plane reinforcement. This chapter analyzes the mechanical performance of in-plane textile reinforced 3D printed concrete and polymer concrete. To do so, textile reinforced slabs were 3D printed and then tested in a 3-point bending configuration to study the reinforcement effect. It was found that for 3DP textile-reinforced concrete, textile reinforcement seems to affect the post-peak behavior positively. On the other hand, due to the specific nature of the polymer concrete mix, the addition of textile layers had a detrimental effect on mechanical performance. The mechanisms behind this phenomenon are discussed herein.

Experimental Methods

Materials

A high-performance 3D printable concrete mix was designed. Fresh-state properties such as rheology, extrudability, and buildability were considered. High compressive strength in the hardened state was addressed by selecting a high content of pozzolanic materials with respect to aggregate [43]. A well-graded aggregate with a maximum nominal aggregate size of 2.36 mm and a predominant range comprised of between #20 to #50 (0.8-0.3 mm) was used. Figure 41 shows the particle size distribution of the aggregate used in producing 3D printed concrete. This maximum aggregate size ensures proper printing resolution for the 20 mm nozzle diameter used in printing.

Type I-II Portland cement, type-F fly ash, and silica fume (Rheomac SF 100, BASF group) were used. The binder (cement, silica fume, and fly ash) to aggregate ratio and the pozzolanic material's content (cement and silica fume) to the total binder weight were adopted based on

`

the recommendations by Le et al. [43]. The mix also included a polycarboxylate-based high-range water-reducer (HRWR) admixture (MasterGlenium 3030, BASF group). This HRWR meets ASTM C494/C 494M requirements for Type F, high-range water-reducing, admixtures [160]. It was added in a dosage of 1.05% to the binder by weight. Previous researchers showed that such content is adequate to reduce the water-binder ratio and achieve satisfactory rheological properties [43,161]. The water to binder ratio was kept at 0.28. Concrete mix design proportions used in the 3D printed concrete are presented in Table 13.

Table 13. Concrete mix proportions used for 3D printed concrete.

Component	Quantity (kg/m^3)
Cement	546
Fly ash	156
Silica Fume	78
Sand	1171
Water	219
HRWR	8.20

Methyl Methacrylate (MMA) polymer (by Transpo Industries, New Rochelle, NY, USA) was used to produce PC. The polymer system consists of two parts: a low viscosity MMA monomer resin and a Benzoyl Peroxide as an initiator. Pyrogenic fumed silica (Cabot Corporation, Alpharetta, GA) with a hydrophobic surface treatment, a specific surface area of 120 m^2/g, and a density of 2.2 g/cm^3 was mixed with the resin to modify its rheological properties. Type-F fly ash (Salt River Materials Group, Scottsdale, AZ) compliant with ASTM C618-19 [174] with a density of 2.3 g/cm^3 was also used as a filler to increase the packing fraction and consequently the mechanical performance. A well-graded fine quartz

aggregate with a nominal maximum size of 2.36 mm was used for both cement concrete and PC mixes. The aggregate size distribution for both aggregates is depicted in Figure 41.

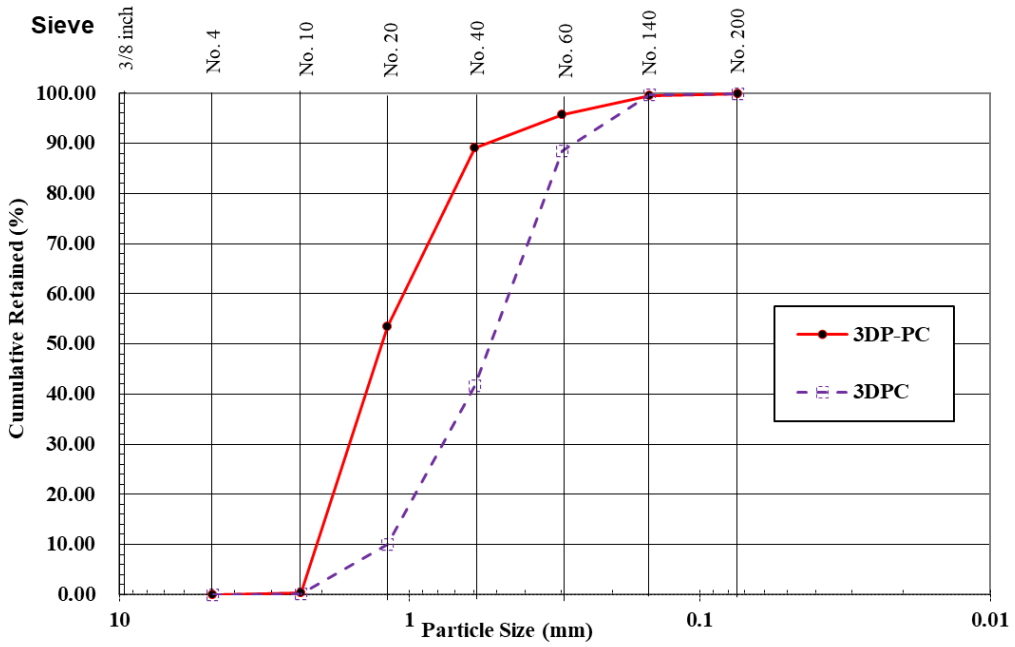

Figure 51. Sieve size distribution for aggregate used in both polymer concrete (3DP-PC) and cement concrete (3DPC) mixes.

The nominal maximum size of the aggregate needed to be smaller than the 5 mm window size of the textile fiber fabric to ensure proper impregnation. The polymer concrete mix proportions are presented in Table 14.

Table 14. Concrete mix proportions used for 3D printed polymer concrete.

Component	Quantity (kg/m^3)
Polymer	188.8
Hardener	7.6
Fumed silica	23.6
Type-F fly ash	466.7
Aggregate	1132.6

`

The cement concrete reference specimens were printed and cured in a standard curing room at 99% relative humidity (RH) and 22 ºC for 28 days to reach the design strength. Studies reported that PC achieves about 75% of its strength within one day of curing [180–182] and most of its total strength after seven days of curing in such ambient temperatures [183]. PC was therefore cured at 85 C for seven days.

Five cylinders, 2 in (50.8 mm) diameter by 4 in (101.6 mm) height, of each mix were cast to determine the compressive strength of conventional concrete and PC as per ASTM C39-17b [191]. A bidirectional planar basalt fiber textile mesh (Smarter Building Systems, New Port, Rohde Island, USA) was used to reinforce TRC and TRPC specimens. *T*he basalt fiber textile mesh characteristics are presented in Table 10 (Chapter 6) as reported by the manufacturer.

Mixing and Printing

TRC and TRPC mixtures were mixed using the proportions described above and following standard concrete mixing protocol. Both mixes were mixed for 3-5 minutes using a 4.7-liter bowl-lift standard mixer until a uniform mixture is obtained. TRC and TRPC panels of 20mm thickness were 3D printed using a cartesian 3D printer, as depicted in Figure 53. The basalt fiber textile fabrics described above were placed by pausing the printing after the deposition of the substrate layer, as depicted in Figure 52. Four configurations of 3DP-TRPC panels were fabricated by incorporating 0, 1, 2, and 3 layers of basalt fabric denoted as 3DP-TRPC-0, 3DP-TRPC-1, 3DP-TRPC-2, and 3DP-TRPC-3, respectively. The same reinforcement configurations were used to fabricate the reference 3DP-TRC panels, denoted as 3DP-TRC-0, 3DP-TRC-1, 3DP-TRC-2, and 3DP-TRC-3. Figure 52 illustrates the configurations of 3DP-TRPC and 3DP-TRC panels.

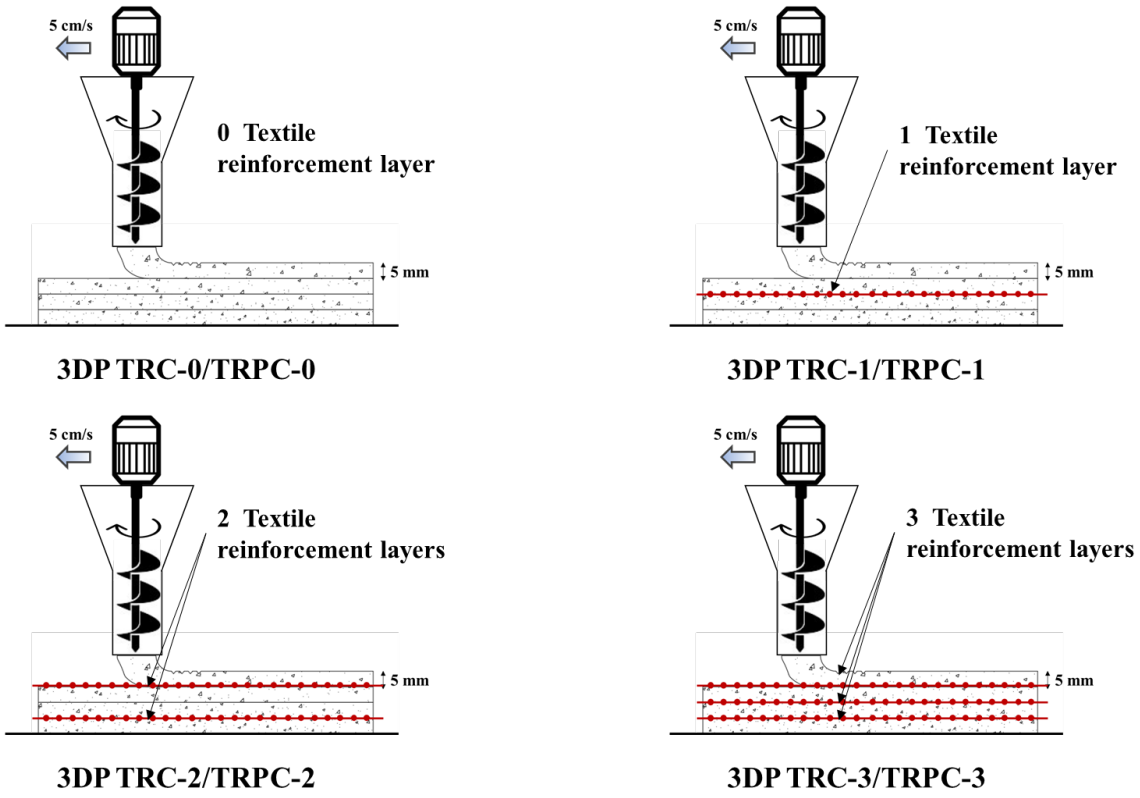

Figure 52. Schematic representation of the printed TRC and TRPC panels incorporating zero (a), one (b), two (c), and three (d) basalt fiber textile reinforcement layers.

All TRC/TRPC panels, regardless of the number of textile reinforcement layers used, were printed in four layers. A layer of fresh concrete (or PC) was printed first, and the basalt fiber textile fabric was placed at the desired thickness location afterward. The second layer of fresh concrete (or PC) was printed, and the process was repeated until the total thickness of the specimen was obtained. Figure 52 shows the fabrication setup of the 3DP-TRPC panels. All TRC and TRPC panels were cured using the two curing protocols of 28 days in 99% RH for conventional concrete and seven days in 30% RH and 80C for PC as described above.

`

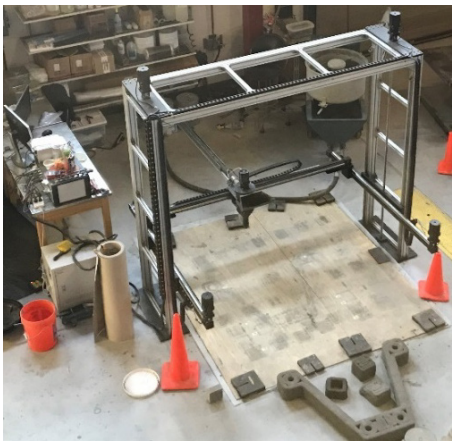

(a)

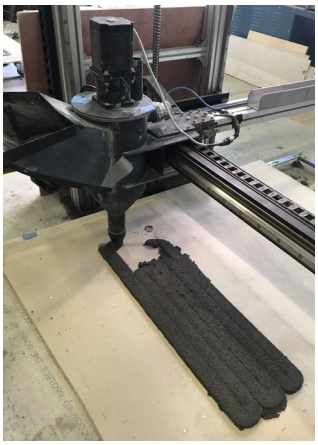

(b)

(c)

(d)

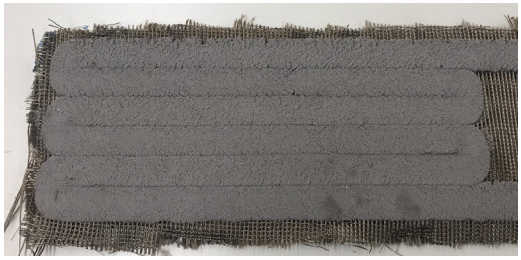

(e)

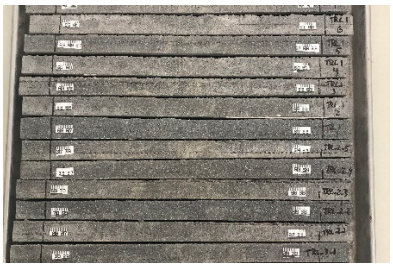

(f)

Figure 53. Process for the fabrication of 3DP-TRC and 3DP-TRPC panels. (a) Gantry robot printer system. (b) Printing of a PC substrate layer. (c) Placement of the basalt textile reinforcement. (d) Printing over the textile reinforcement. (e) 3DP-TRPC specimen before waterjet cutting. (f) Specimens after waterjet cutting.

`

Flexure Test Setup

The TRC/TRPC panels were cut into 400 mm x 35 mm x 20 mm (length x width x thickness) prisms using a waterjet cutting machine. The prisms were tested in three-point bending with a span length of 330 mm, achieving a span-to-depth ratio of 16.5, as depicted in Figure 53 (f). The deflection at the midspan location was measured using a linear variable differential transducer (LVDT). The load and displacement of the load cell were also recorded using MTS® Bionix servo-hydraulic system with a range of 0-25 kN and a resolution of 1 N. For testing, a displacement rate of 0.5 mm/min was imposed at the mid-span location. Five specimens were tested for each TRC/TRPC reinforcement configuration. The test setup is shown in Figure 54 (a). The three-point bending test setup included the digital image acquisition system to capture crack patterns during testing. The crack pattern intensity was quantified via digital image processing technique to assess the ductility of TRC/TRPC. Photoshop® and ImageJ® software were employed for examining the cracking pattern. Details for the method used for image transformation and processing have been described elsewhere [192]. Two types of cracks were analyzed, horizontal and vertical cracks, to assess the flexural ductility and the concrete-fabric bond strength. Figure 54 (b) shows the digital image data acquisition.

`

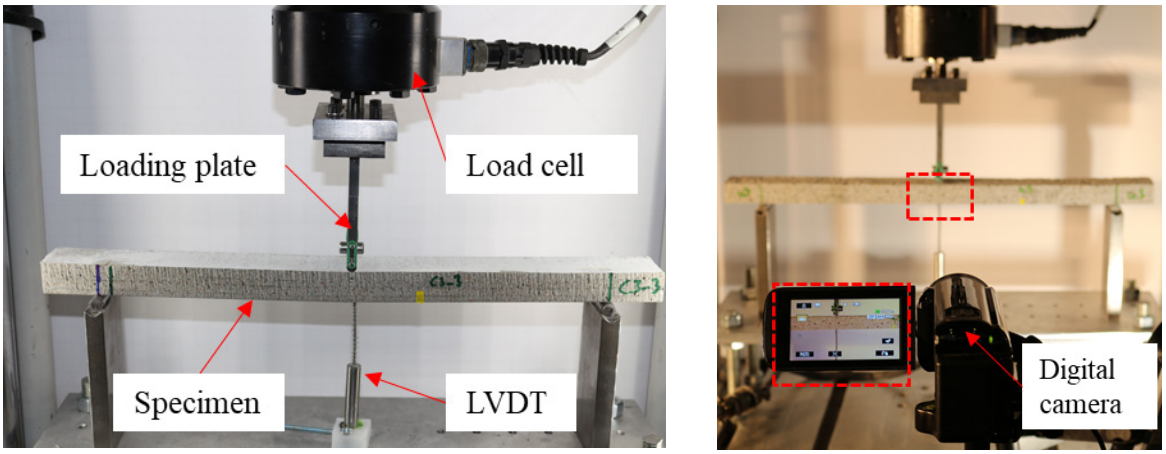

(a) **(b)**

Figure 54. Three-point bending test setup. (a) Specimen during testing and LVDT displacement recording system; (b) Digital image data acquisition system.

Results and Discussion

The mean compressive strength for the conventional reference concrete after 28 days was 62.9 ± 5.6 MPa (for cast specimen as depicted in Figure 26, Chapter 3). The PC mix was modified from the one shown in Chapter 6 (average compressive strength after seven days 53.9 ± 5.8 MPa). The cement-based concrete mix was intentionally designed to have similar or higher compressive strength than the polymer-based mix to ensure a fair comparison. The median modulus of rupture (MoR)-displacement curves of the three-point bending tests of 3DP-TRC and 3DP-TRPC specimens with different textile layers are shown in Figure 55. The mean moment capacity of TRC and TRPC for the different reinforcement configurations are presented in Figure 56.

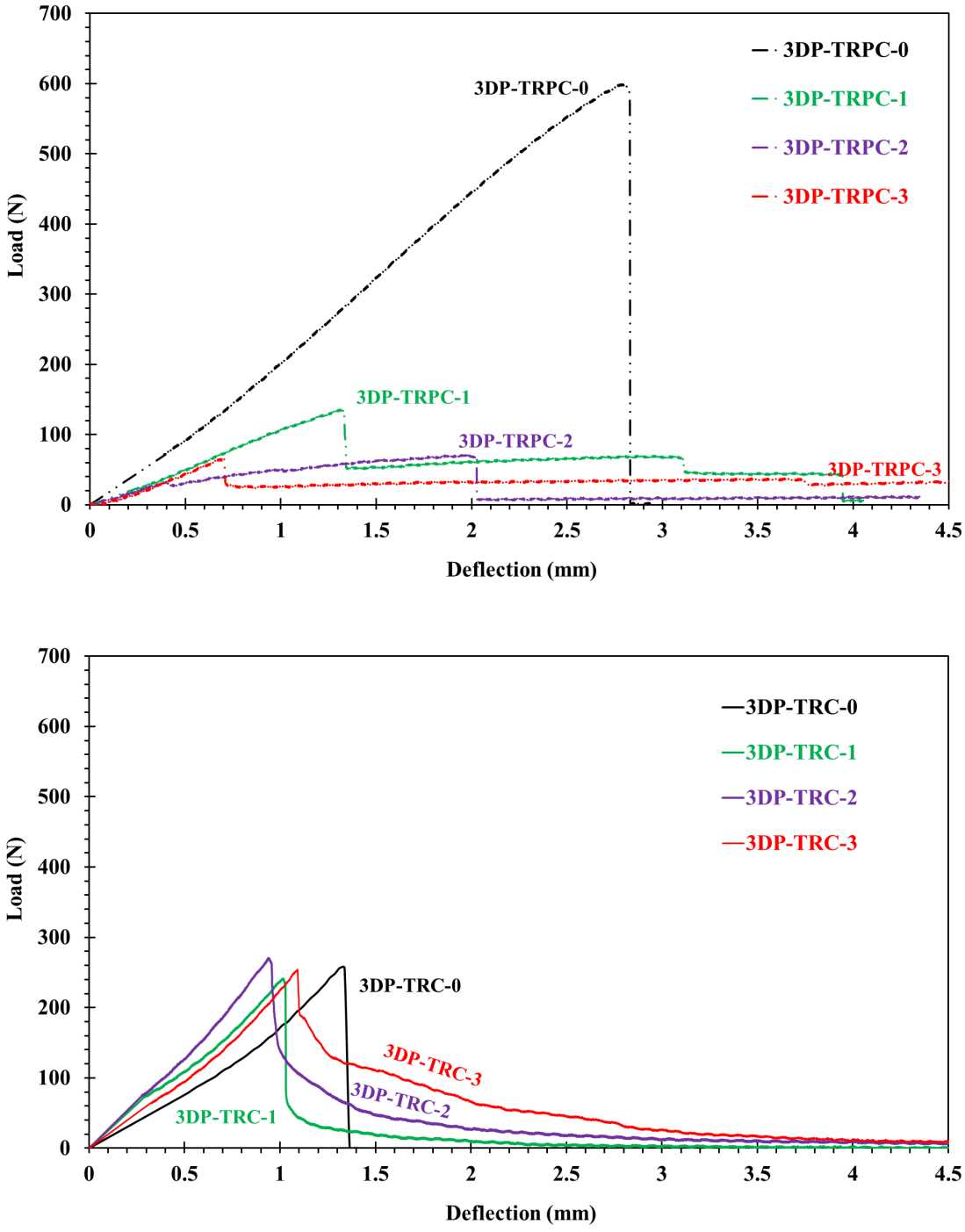

Figure 55. Load-deflection response of 3DP-TRPC specimens with different textile layers (top) compared with 3DP-TRC (bottom). Five specimens were tested for each case.

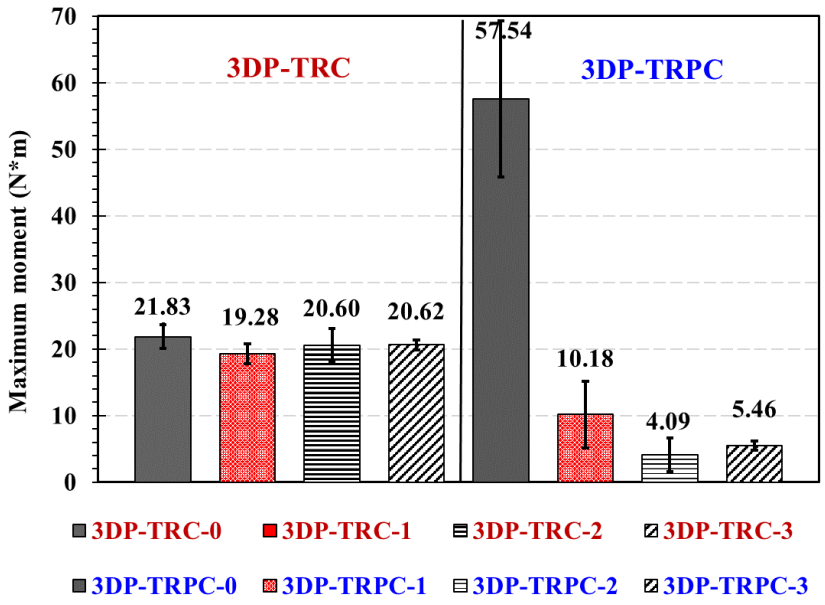

Figure 56. Moment capacity for 3DP-TRC and 3DP-TRPC with different numbers of textile reinforcement layers.

While comparing 3DP-TRC reinforcement configurations, Figure 55 and Figure 56 show that the addition of textile reinforcement layers did not significantly affect the maximum moment. This was also observed in Chapter 6 for distinct layer cast specimens, and it is attributed to the limited bond strength between the fibers and the cementitious matrix due to the high viscosity of the cement slurry, and consequently, the low penetrability of the cement matrix to the fiber mesh. Nonetheless, the post-peak behavior is significantly different due to the action of the reinforcement.

For 3DP-TRPC, Figure 55 and Figure 56 show the superior mechanical performance of 3DP-TRPC-0 (no reinforcement) while compared to 3DP-TRC and 3DP-TRPC with other reinforcement configurations. While comparing 3DP-TRPC configurations, it can be seen how adding reinforcement seems to have a detrimental effect on the maximum moment of

`

the composites. This can be attributed to the fact that the MMA polymer has a very low viscosity, but then it is modified by adding fumed silica (very high surface area) to meet the rheological criteria for 3D printing. The particle system has increased the surface area significantly due to using high surface area modifiers, and the coating polymer thickness wetting each particle is significantly reduced. The fact that the thickness of this coating is shallow has a detrimental effect on the wettability of the polymer on the fiber yarns. This is depicted in Figure 58. Despite the 3DP-TRPC mix having a maximum moment capacity two times higher than the 3DP-TRC mix (unreinforced configuration), once the textile reinforcement is implemented, the mechanical performance drops significantly due to the inability of the mix to wet and penetrate the fiber yarns. There is then no composite action between the fiber and the matrix, and the fiber planes are the ones that first fail to propagate the cracks through them. This low penetrability is depicted in Figure 58.

Due to the poor performance of the 3DP-TRPC mixes, only the crack patterns of 3DP-TRC mixes were studied. The crack pattern was analyzed using a digital image correlation system (DIC) for both horizontal and vertical cracks to assess cracking intensity and ductility. Crack pattern analysis results for horizontal and vertical cracks are presented in Table 15. None of the 3DP-TRC specimens showed any horizontal cracks (also observed for TRC specimens, Table 11, Chapter 6). This can be explained due to the brittle behavior of the composite material due to the low tensile strength of the cement-based mix. Moreover, examples of crack patterns for different 3DP-TRC and specimens are shown in Figure 57**.**

`

Table 15. Vertical crack area (mm^2) and width (mm) for 3DP-TRC (Mean values ± standard deviation)

Specimen	Vertical crack area	Vertical crack width
3DP-TRC-0	4.90 ± 2.38	0.36 ± 0.19
3DP-TRC-1	11.47 ± 4.13	0.56 ± 0.33
3DP-TRC-2	12.85 ± 1.00	0.67 ± 0.39
3DP-TRC-3	17.30 ± 1.69	0.93 ± 0.58

The assessment for vertical cracks is presented in Table 15. It can be observed that the average vertical crack width increases as the number of fabric layers increase. The crack area also increased by increasing the number of textile layers. It is worth mentioning that 3DP-TRC-3 observed an average area of the vertical cracks of 17.30 mm2 that of 3 times the one observed for 3DP-TRC-0. The use of three layers of basalt fibers provided superior strength to 3DP-TRC and improved the post-failure response, as depicted in Figure 55. Figure 57 shows the cracking patterns for the different 3DP-TRC configurations. The absence of horizontal cracks for all the reinforcement systems and the increase in vertical crack area and width as the number of reinforcement layers is increased can also be noted.

`

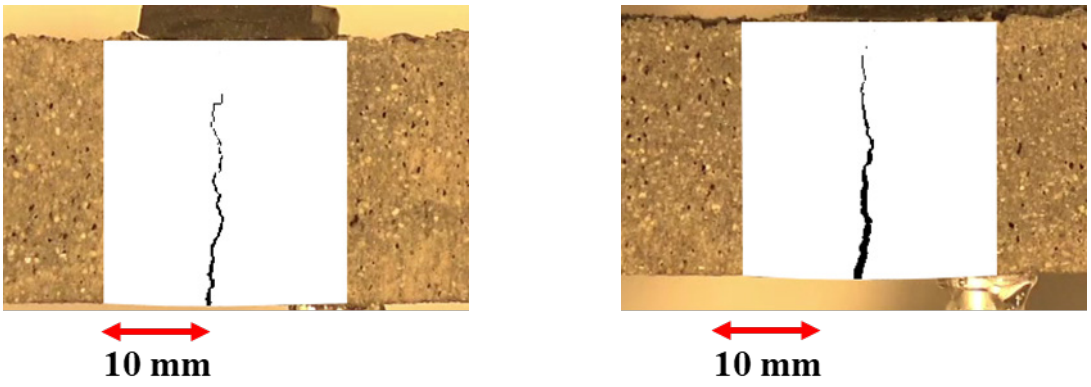

(a) 3DP-TRC-0 **(b) 3DP-TRC-1**

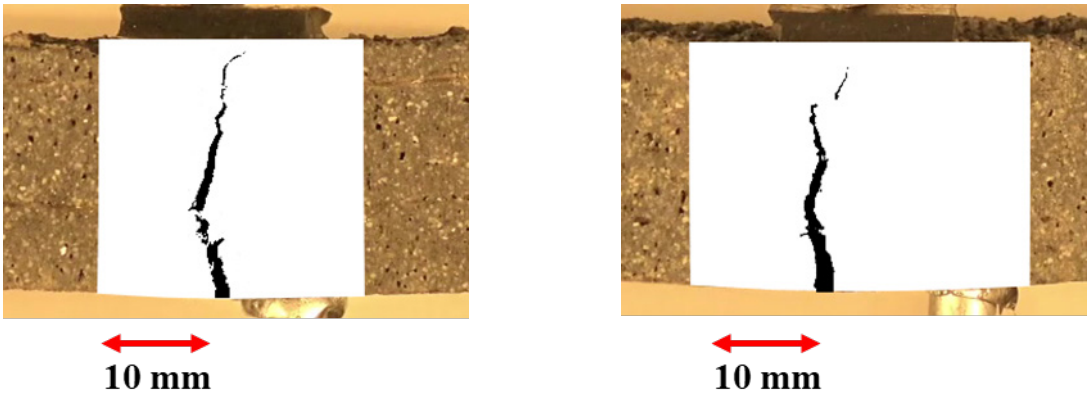

(c) 3DP-TRC-2 **(d) 3DP-TRC-3**

Figure 57. Cracking pattern for 3DP-TRC with different reinforcement configurations recorded using DIC on the side of the specimens. (a) 3DP-TRC-0 (b) 3DP-TRC-1 (c) 3DP-TRC-2 (d) 3DP-TRC-3.

To further understand the failure mechanisms of 3DP-TRC, images of failed specimens were analyzed, as shown in Figure 58.

`

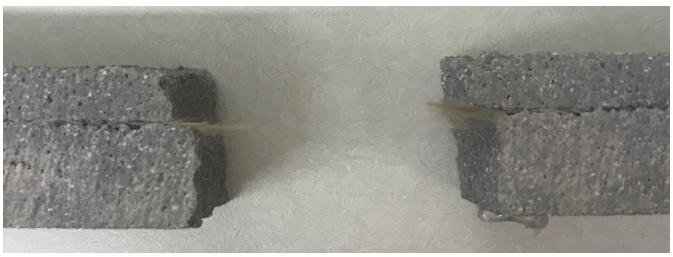

(a)

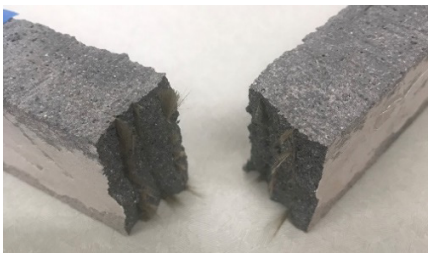

(b)

(c)

(d)

Figure 58. Pictures of the failure modes for 3DP-TRC (a, and b) and 3DP-TRPC (c and d).

From Figure 58. It can be observed how the polymer concrete fails to impregnate the fiber yarns due to the factors mentioned above (Figure 58 d). This results in a failure mode consisting of a vertical crack propagating to the reinforcement plane and propagating horizontally.

The ability of the matrix to impregnate the textile fabric is a critical factor that affects the bond strength between the polymer or cement matrix and the textile fabric. The polymer material fails to impregnate the textile fabric compared with the cement paste. Previous research showed that improper impregnation of textile fabric associated with the use of cementitious matrix in conventional TRC with outer fiber filaments properly impregnated and central filaments poorly impregnated [149,150]. The improper impregnation of fiber

`

filaments leads to reduced contact surface area between the matrix and the fibers, limiting the bond strength and the fibers' ability to bridge cracks.

For 3DP-TRC specimens, a fiber rupture mechanism prevails (Figure 58 a, b). On the other hand, for 3DP-TRPC, fiber debonding rather than fiber rupture becomes the primary failure mechanism.

This work analyzes the potential use of the textile reinforcement technique for concrete and polymer concrete additive manufacturing. While the effect of textile reinforcement on 3DP concrete was positive (improving the post-peak behavior), the effect for polymer concrete was found to be detrimental due to the nature of the polymer used for the mix (very low viscosity). To achieve a printable mix, the low viscosity polymer was modified (in terms of rheology) by adding a high surface area fumed silica. This reduced the particle polymer coating thickness reducing the wettability of the fiber yarns dramatically.

`

Chapter 8. Concrete 3D Printing as an Emerging Technology to Improve Infrastructure Resilience

Analysis of Concrete 3D Printing as an Emerging Technology and Level of Maturity Evaluation

There is not a consensual definition for emerging technologies (ETs) in the scientific literature. Authors such as Rotolo et al.[193] have made an outstanding effort in developing a foundational definition that will be quoted herein:

"An emerging technology is a radically novel and relatively fast-growing technology characterized by a certain degree of coherence persisting over time and with the potential to exert a considerable impact on the socio-economic domain(s) which is observed in terms of the composition of actors, institutions and patterns of interactions among those, along with the associated knowledge production processes. However, its most prominent impact lies in the future and so in the emergence phase is still somewhat uncertain and ambiguous".

Furthermore, Rotolo et al. [193] defined the requirements for a technology to be classified as an ET as (a) being radically novel, (b) growing at a relatively fast pace, (c) being coherent over time in terms of maturity, (d) prone to create an impact on a socio-economic scale, and (e) being uncertain at early phases of analysis.

Concrete 3D printing can be classified as a non-consumer ET since it meets all the requirements cited above. In addition, the maturity of the technology, in general, can be evaluated by using different methods such as the technology readiness levels (TRLs) developed by NASA [194,195] or the Gartner hype cycle [196] depicted in Figure 59. The Gartner hype cycle divides the life of technology into five states, as depicted in Figure 59.

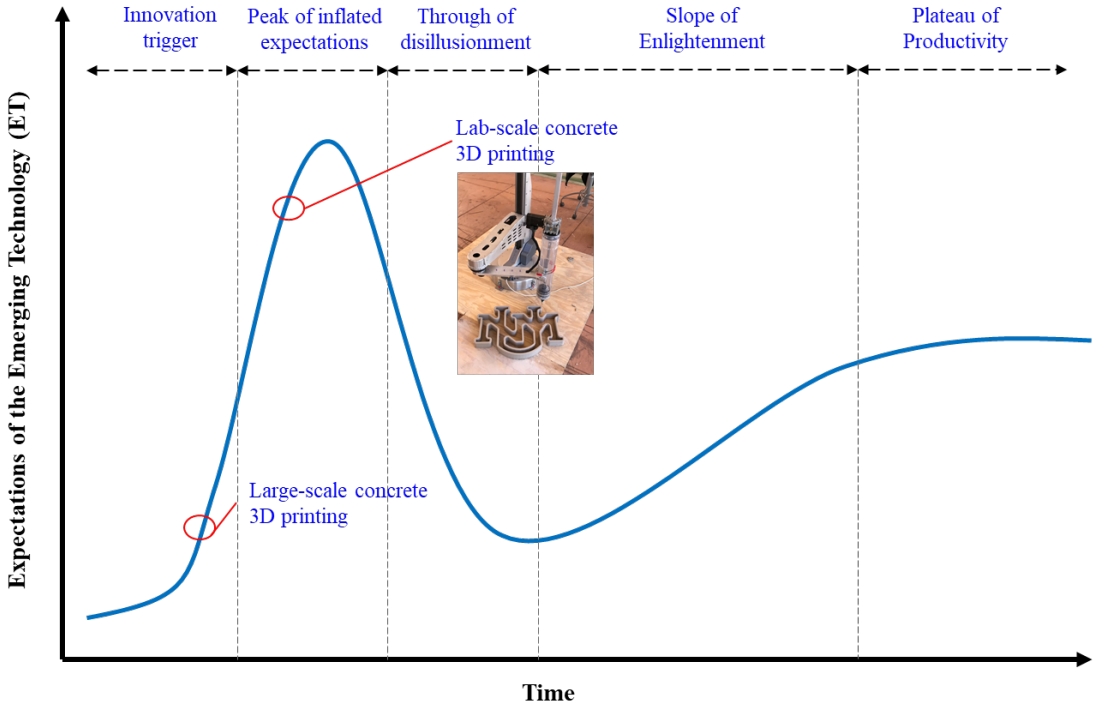

Figure 59. Gartner Hype Cycle for concrete 3D printing at various scales. Adapted from [196].

When 3D printing as a technology first appeared on the 2012 Gartner Hype Cycle of ETs, it was positioned at the peak of inflated expectations [197]. Concrete 3D printing can arguably be located at the first stage (innovative trigger) or at the peak of inflated expectations based on the Gartner hype cycle definitions depicted in Figure 59 and depending on the scale of the manufacturing process (lab vs. large scale) [198].

`

Table 16. Five key phases of a technology's life cycle according to Gartner hype cycle. Adapted from [196].

Phase	Description
Technology Trigger	Technology with potential breaks through at a research scale. There is proof-of-concept research, and media interest starts to arise. However, no products are streaming from the technology yet. Its viability is not proven.
Peak of Inflated Expectations	Early press divulges several successful stories related to the technology, often coexisting with cases of failure. As a result, some early adopters act, but most do not.
Trough of Disillusionment	As adopters fail to embrace the technology, producers of the technology languish or fail. The investment only continues if technology producers can adapt the technology to the demands of early adopters.
Slope of Enlightenment	The gap between technology providers and adopters starts to close. The potential benefits to the adopters are widely understood. As a result, technology providers develop new generations of products. A substantial amount of companies fund pilot (or R&D) projects. Conservative companies remain watchful.
Plateau of Productivity	Dominant adoption starts to take off. The technology market applicability is clear and is yielding benefits to the adopters. If the technology can be applied to other (new) markets, it can expand and keep growing.

It is important to note that the most prominent benefits for ETs in industry and communities are commonly attained in the final phases of the life cycle. 3D concrete printing is being adopted at a relatively slow pace. Some examples of large-scale projects can be found herein [35,44,199–201]. That slow adoption is relatively common in ETs that are marketed for specific industrial applications [202]. For example, readers are referred to literature

`

explaining the reasons behind the slow adoption of building information modeling (BIM) in construction projects [203,204].

Potential Contributions of Concrete 3D Printing Towards Infrastructure Resilience

Adopting new technologies such as concrete 3D printing is primarily influenced by its perception of generating perceived benefits for the adopters. In the particular case of concrete 3D printing, Reda Taha et al. [198] listed the potential benefits of the adoption of this technology as:

- Possibility to parametrically engineer the product's properties in terms of material selection, quantity, or infill pattern to optimally accommodate the structural requirements [11,127].
- The absence of molds, which could potentially impact productivity and reduce labor in the precast industry.
- The possibility to optimize topologies for each project since no molds are required, reducing the amount of materials needed and the environmental cost of the overall production.
- The ability to engineer mix designs by including recycled and environmentally friendly materials, reducing the CO_2 footprint.

Nonetheless, some authors [205] advise that using only economic growth indicators to evaluate technology prospects can only be done once the technology is widely diffused and used. This expansion process is based on expectations and ultimately depends on decisions taken by adopters. The mitigation of the uncertainties related to the potential use of ETs could facilitate and accelerate the technology adoption [202,206].

`

Additive manufacturing for construction applications is an ET that is increasingly becoming more accessible in research institutions and making its way into the field. Some construction companies are adopting it for certain types of projects [35,44,199,200]. The potential adoption of this technology or other automated construction technologies by companies, stakeholders, and other services providers in the construction field raises questions on the potential impact these technologies could have on infrastructure resilience [198,202,206]. Studying the resilience of these ETs is essential for system managers, researchers, and end-users of the systems affected in case of a disruptive event [207]. Resilient infrastructure systems are essential to mitigate the social impacts in case of an extreme event. Furthermore, the present status of the civil infrastructure in the U.S. requires a noteworthy upgrade [208]. ETs have the potential, once included in the market, to improve infrastructure performance and, particularly, resilience [198]. Also, resilient infrastructure can help prevent system interactions if an extreme event in which one infrastructure system failure leads to other infrastructure being negatively affected [209].

The search for a definition of resilience in multiple fields, specifically in infrastructure engineering, has progressively evolved [202]. The reader is referred to Cimellaro et al. [22] for an extensive list of these definitions.

Based on the general definition by McDaniels et al. [207], resilience can be defined as the ability of a complex system to absorb a shock while maintaining function. Ayyub [210] defined resilience in the broad context of infrastructure, communication networks, and communities as follows:

"Resilience notionally means the ability to prepare for and adapt to changing conditions and withstand and recover rapidly from disruptions. Resilience includes the ability to withstand

`

and recover from disturbances of the deliberate attacks, accidents, or naturally occurring threats or incidents".

Other authors have built upon the classical definition of resilience to adapt it to infrastructure engineering. For example, Bruneau et al. [211] defined resilience in the context of a disruptive seismic scenario as: *"Community seismic resilience is defined as the ability of social units (e.g., organizations, communities) to mitigate hazards, contain the effects of disasters when they occur, and carry out recovery activities in ways that minimize social disruption and mitigate the effects of future earthquakes".* Bruneau et al. [211] also divided resilience into four categories, widely known as 4Rs: robustness, redundancy, rapidity, and resourcefulness. A schematic representation of these properties is depicted in Figure 60.

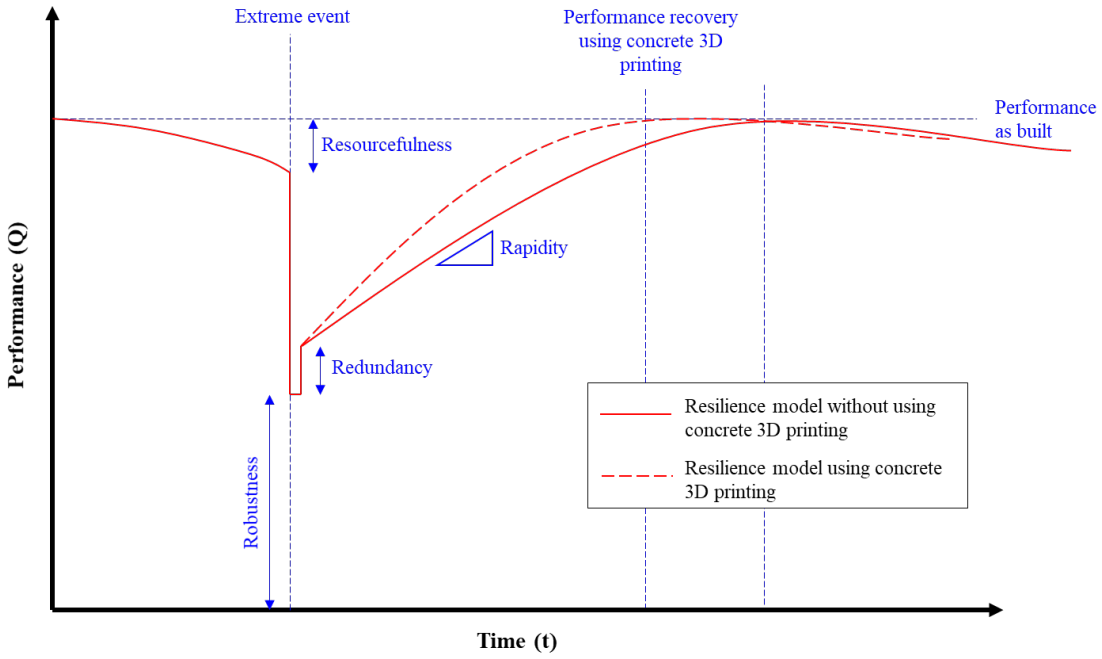

Figure 60. Resilience model as described by Bruneau et al. [211] with and without the implementation of concrete 3D printing by technology adopters.

`

Across all these definitions, the authors imply that resilience as a concept entails both strength to resist the extreme event and flexibility to adapt to the disrupted scenario. The properties described by Bruneau et al. [211] can be divided into two largest groups: *ex-ante* and *ex-post,* depending on whether the actions leading to these properties are taken before or after the disruptive event [207]. As depicted in Figure 60, ex-ante contributors are robustness, resourcefulness, and redundancy since they are adopted before the event occurs while rapidity occurs after the event (*ex-post*).

Adopting 3D concrete printing as an automated manufacturing technique depends primarily on the socio-economical aspects described in Chapter 1; it is worth studying the potential that this ET has on improving infrastructure resilience. Concrete 3D printing has the potential to reduce construction times and to close the gap between designers and contractors [198]. In the case of an extreme event, these features are very important since they can improve the rapidity (post event), improving the rate at which the infrastructure system can recover its capacity or performance. Also, the potential that 3D printing has to improve the organization in case of an extreme event is a critical aspect as reported by the resilience alliance (www.resaliance.org) due to the high degree of automation and the need for less agents implicated in the creation of the process from design to manufacturing. Another key aspect in the case of an extreme event is the capacity to adapt. The freeform nature of 3D printing makes this technology very versatile in a disruptive event affecting civil infrastructure.

In a hypothetical case of a disrupting event affecting civil infrastructure such as a bridge failure, halting communication, the fast and adaptative construction of temporal 3D printed segmental bridges can help in restoring the functionality of the infrastructure system

promptly [202]. There are proofs-of-concept of 3D printing technology used for the segmental construction of segmental pedestrian bridges [119,121,212].

A new temporary segmental bridge can be constructed on-site or off-site using a combination of 3D printing and post-tensioning technologies [121]. The manufacturing of the concrete segments using 3D concrete printing can be made quickly [41,213,214]. This concept is shown in Figure 61. 3D printing can occur in any facility near the bridge site to reduce the need for transporting bridge sections [206]. The concrete segments can be placed using cranes and post-tensioned using segmental bridge construction technology [206].

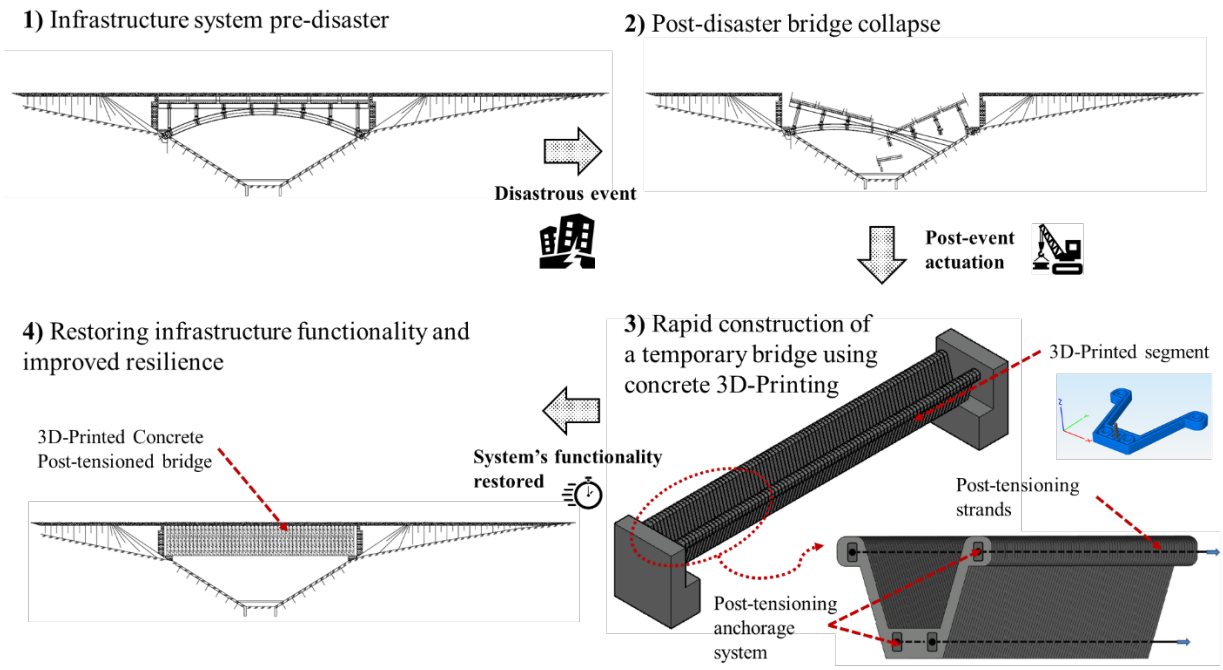

Figure 61. A schematic illustration of a 3D printed post-tensioned temporary concrete bridge using. Adapted from [202].

3D concrete printing as an ET has a significant potential to improve infrastructure resilience. Nonetheless, the expectations from 3D concrete printing are expected to change as the technology evolves (matures) over time, as depicted in Figure 59. 3D concrete printing for

`

construction-scale projects is still in the research phase with only a few field implementation cases. Nevertheless, the use of construction-scale 3D concrete printing is likely to advance infrastructure resilience at structural, economic, and social levels.

Linkov et al. [215] identified that addressing resilience quantifications by only using a risk assessment approach is one of the main barriers to adequately measuring resilience contributors for complex infrastructure systems. In this line of research, Davidson [216,217] identified the importance of interdisciplinary research in evaluating community resilience to natural disasters. Further work and economic and socio-economical frameworks need to be designed to assess the return on investment and whether 3D concrete printing can support their goal to improve infrastructure resilience and the level of improvement it can offer. Furthermore, it is essential to develop methods for quantifying the contribution of 3D concrete printing to infrastructure resilience [198]. Such measurement would enable decision-makers and stakeholders to decide whether to adopt or invest in an ET

Besides the potential contribution of ETs in general and 3D concrete printing to infrastructure resilience, some challenges could prevent implementing the 3D concrete printing technology at a construction scale in the long term. For example, the cost of the technology and its evolution over time is a critical factor for implementation [198]. Also, quantification of the cost of production using 3D concrete printing [41,214] is required, and the rate of maturity evolution of 3D printing technologies is a challenge that needs to be further studied for successful implementation.

Another prevailing challenge that 3D concrete printing faces is its upscaling for field implementation [198]. 3D concrete printing technology has been evaluated at the lab scale and shows encouraging results, yet technical difficulties are associated with their large-scale

`

field implementation [198]. Upscaling failures have raised important critiques to ETs for overpromising and underdelivering. The use of life cycle assessment has been suggested as a critical tool for examining the capability to upscale ETs [218]. Also, field testing has been proven to improve ETs' maturity [219].

Finally, ETs also suffer from the lack of realistic research data required for field implementation. The absence of design guidelines and desired performance specifications for 3D concrete printing is a significant challenge toward successful field implementation. Such guidelines and performance specifications are essential for companies developing ETs to advance their technologies to meet the construction industry's field expectations [220].

`

Chapter 9. Conclusions

Research Summary and Contributions

This research seeks to investigate the use of new materials and reinforcement configurations as well as the rheological and mechanical properties of 3D printed concrete materials. Five main objectives are classified and targeted in sequential order in Chapters 3 to 7.

Chapter 3 explores how the combined presence of both interfaces within the same bulk specimen can affect the overall anisotropic mechanical behavior of 3D printed concrete. Furthermore, the potential effect of the printing infill pattern on the mechanical properties of bulk specimens and the anisotropy of 3D printed concrete is investigated. This work examines the significance of infill printing patterns on the hardened properties (density and compressive strength) of 3D printed concrete. Concrete specimens were printed with three different infill patterns, and the performance of those specimens was compared with conventionally cast concrete ones. The anisotropy of the 3D printed concrete associated with the infill printing patterns and testing directions was analyzed and reported herein through compression testing.

Chapter 4 reports on the potential use of polymer concrete for 3D printing applications. The influence of mix design parameters, specifically rheology modifier content, filler to polymer ratio, and aggregate to polymer ratio on the rheological properties of a 3D printable PC, are investigated. The rheological properties of seven PC mixes are tested and characterized. PC can be described as a Bingham pseudoplastic material, and a Herschel-Bulkley model can accurately describe its rheological behavior (dynamic shear stress) over time. The evolution of the static yield stress over time was found to follow an exponential trend. Using these models to predict PC's dynamic and static yield stress shall enable the design of efficient and

`

stable 3D printing. The use of carbon nanofibers (CNFs) as a rheology modifier with the potential to also improve compressive strength is also explored. It was found that the presence of CNFs at very low concentrations (0.5% by resin wt.) has a significant effect on increasing the static yield stress over time. The compressive strength for cast and 3D printed specimens is also improved by using CNFs at low concentrations (0.5%).

Chapter 6 explores the potential use of textile reinforcement to improve the flexural behavior of distinct layer casted composites. Cement-based (TRC) and polymer-based (TRPC) materials are explored. The use of a polymer material to fully replace the cement binder results in a significantly improved flexural capacity, superior ductility, and substantial plasticity compared with TRC. It is evident that TRPC represents an excellent new material for civil infrastructure applications. This is the first article to examine this type of concrete to the best of the authors' knowledge. Flexural testing was conducted on TRPC with different reinforcement configurations. The flexural capacity, ductility, toughness, and the crack pattern of TRPC were quantified and compared with conventional TRC fabricated using Portland cement concrete of similar strength and with the same textile fabric and reinforcement configurations. This Chapter paves the way for the investigation on Chapter 7.

Chapter 7 investigates the use of textile reinforcement configurations for 3D printing. Cement-based and an innovative polymer-based material are printed while implementing textile reinforcement at the interlayer plane. Then, the mechanical performance by using 3-point bending testing and DIC techniques is analyzed.

Chapter 8 analyzes concrete 3D printing as a non-consumer ET and its potential to improve infrastructure resilience. First, the technology is classified as emerging based on the current literature. Then, the technology's maturity level for both lab and large scales is evaluated by

`

using the Gartner hype cycle. Finally, the potential benefit of this technology towards infrastructure resilience is analyzed by using state-of-the-art literature in the field of engineering and social sciences. It is concluded by using a case study that 3D printing can improve resilience after a disruptive event (ex-post) through an increase in rapidity (the rate at which the structure's performance is brought back to normal).

Main Research Findings

Specific conclusions are given in Chapters 3 to 7. Here, conclusions regarding the thesis are drawn.

In Chapter 3, bulk (complete filled volume) 3D printed concrete specimens were manufactured using the same printing parameters and different infill patterns and tested in compression in the three principal directions (Z being the extrusion direction).

The investigations show that 3D printed concrete can have a higher dry density and higher compressive strength than conventionally cast concrete due to the increased pressure on the concrete layers and thus compaction during the printing process. The results also show that there is a directional dependency on all the infill patterns. The specimens show lower compressive strength and modulus of elasticity in the Z (extrusion) direction than the X and Y directions but insignificant differences in the strength and modulus between the X and Y directions. However, no directional dependency was found for the strain at failure. On the other hand, no significant difference in the mechanical properties of 3D printed concrete was observed or can be attributed to the infill printing patterns.

This phenomenon can be explained by the fact that interfilamentous shear strength (shear strength between the filaments at a given layer) is weaker than the interlayer shear strength (shear strength between the layers). This strength difference is mainly caused by the presence

`

of macro-scale pores in the interfilamentous interface due to the low pressure exerted at this plane while printing compared with the interlayer one (filaments are pressed during deposition). It is worth mentioning that printing pressure during deposition can be significantly influenced by printing parameters such as filament height and width as well as layer thickness.

Furthermore, 3D printed concrete shows higher compressive strength for two out of the three testing directions (X and Y) than conventionally cast concrete. This is due to the above-mentioned densification associated with the printing process that is strongly dependent on the printing parameters, precisely nozzle diameter to layer height ratio, and geometry of the printed product.

Higher levels of macroporosity were observed in the interfilamentous interfaces compared with the interlayer interfaces. This can also be explained by the effect of compaction on the interlayer interface and the lack of such pressure in between the filaments [16,20,21]. For the printing parameters adopted in this study, the infill printing pattern seems to make no significant difference in the compressive strength and elastic modulus of 3D printed concrete when tested in any testing direction. This proves that choosing the appropriate printing parameters that suit the 3D printed concrete mix can ensure good, hardened properties of the 3D printed concrete structure independent of the chosen infill printing pattern for bulk specimens. The results are highly dependent on the printing parameters and the rheological properties of the mix.

In Chapter 4, seven 3D printable polymer concrete mixes were designed, and their rheology behavior was characterized. The seven PC mixes were divided into three groups to examine the significance of the rheology modifier (fumed silica), the filler (fly ash and silica fume) to

`

polymer ratio, and the aggregate (silica sand) to polymer ratio. The rheology modifier content seems to have the most prominent effect. Nevertheless, the filler to polymer ratio and the aggregate to polymer ratio also affect the rheology of the PC mix, specifically the static yield stress and thixotropy.

The fresh PC can be classified as a non-Newtonian fluid, and it tends to become more shear-thinning as time passes (the flow index decays with time). The consistency, *k(t),* and the flow index, *n(t),* seem to follow generally a linear evolution over time, with ascending evolution for *k(t)* and descending for *n(t).* The dynamic yield stress seems to remain time-independent for all seven mixes up to 30 minutes. The static yield stress and thixotropy, on the other hand, build-up with time. Epoxy Novolac PC seems to behave as a pseudoplastic Bingham material, and it can be predicted at early ages (up to 30 min) by using a Herschel-Bulkley model. This model allows for predicting the dynamic yield stress, which is a critical criterion for efficient material extrudability and is strongly related to the extrusion rate and the 3D printing speed. The static yield stress of PC grows exponentially over time, which can be beneficial to ensure the stability of a printed geometry, particularly if printing is taking place at a relatively high rising speed.

The physical mechanism controlling the rheological behavior of PC is strongly related to the polymerization rate of the polymer, the amount, nature, and size distribution of the aggregate and filler particles and the interactions between the polymer and the aggregate. Modeling and understanding the rheological behavior of PC can help in successful and economical 3D printing.

In Chapter 5, three 3D printable polymer concrete mixes were designed, and their rheology behavior was characterized. The significance of CNFs in two different concentrations (0.5

`

and 1% of the polymer matrix weight) in the rheological properties and compressive strength is examined. The presence of low concentrations (0.5%) of CNF has a remarkable effect on the static yield stress. The addition of CNF in higher percentages does not seem to increase the static yield stress further. This higher static yield stress and the exponential growth of it over time can be of interest to ensure the stability of a printed geometry, particularly if printing is taking place at a relatively high rising speed. The compressive strength is significantly improved by using CNF for both cast and 3D printed mixes. As described in Chapter 4, the material is a non-Newtonian fluid, and the Herschel-Bulkley model provides a good fit for the flow curves. The model provided in Chapter 4 seems to describe the behavior of this nano-modified composite material accurately. The effect of the polymerization on the rheological properties are described in depth in Chapter 4.

In Chapter 6, flexural tests were carried out to examine an innovative TRPC panel's flexural behavior using PC incorporating various basalt fiber textile fabric layers. TRPC panels incorporating basalt textile reinforcement exhibited a higher flexure strength, significantly improved ductility and plasticity, and a substantially enhanced toughness than conventional cementitious TRC. The flexure performance of TRPC improves as the number of reinforcement layers increase. Cracking pattern analysis showed the ability of reinforced TRPC to develop significantly wide horizontal and vertical cracks and maintain structural integrity at high loads and deformation compared with conventional cementitious TRC. The fiber bridging effect was evident in TRPC with two and three reinforcement layers. On the other hand, limited improvement in flexure performance is achieved in TRC by incorporating basalt-textile reinforcement. The main difference in behavior between TRPC and TRC is attributed to the high bond strength between the polymer matrix and the textile reinforcement

`

yarns compared with that of the cement matrix. The improved bond of the polymer matrix is attributed to the low viscosity, high flowability, and penetrability of the polymer into the fibers of the yarns compared with the cement paste. Such high penetrability enables TRC to observe fiber rupture rather than typical fiber debonding observed in TRC. Finally, it is concluded that it is possible to produce textile reinforced polymer concrete panels with significant flexural capacity, good plasticity, and high ductility using basalt fiber layers.

In Chapter 7, flexural tests were carried out to examine 3D printed panels' flexural behavior using polymer and cement-based concrete incorporating various basalt fiber textile fabric layers. The flexural behavior of both composites is compared.

For 3DP-TRC composites, the basalt fiber reinforcement positively affects the post-peak behavior of the specimen by slowing the mechanical capacity degradation. These results align with the ones from Chapter 6. On the other hand, for 3DP-TRPC composites, the inclusion of textile reinforcement does not improve the mechanical behavior but reduces the mechanical capacity while compared to the reference (unreinforced) specimen. This is due to the reduced wettability of the mix because of the inclusion of particles of a very high surface area in the mix design (fumed silica to increase the viscosity of the polymer and meet the printability requirements).

It can be concluded that even though the 3DP-TRPC mix showed good mechanical properties in terms of modulus of rupture, the rheological mix design conditions make it unsuitable for additive manufacturing with textile reinforcement. Using a polymer with a higher viscosity (such as Novolac) is suggested to meet the rheological requirements with a higher particle coating thickness. As a result, the mix is expected to have higher wettability of the fiber yarns by the mechanisms described in Chapter 6.

`

Cracking pattern analysis showed how adding textile reinforcement layers for the 3DP-TRC composite improves the vertical crack area and width, resulting in higher toughness. Finally, it is concluded that it is feasible to produce textile reinforced polymer concrete panels by using 3D printing technology and basalt fiber layers.

Finally, in Chapter 8, 3D concrete printing is analyzed as a non-consumer ET with the potential to impact socio-economic domains. 3D concrete printing as a technology is still at a very early phase in terms of maturity. The adoption of the technology for large-scale projects is still very slow-paced. Nonetheless, concrete 3D printing can improve infrastructure resilience in case of a disruptive event by increasing the rapidity to restore infrastructure functionality.

Future Work

Previous studies in the literature indicated that the bond strength of the printed concrete is mainly controlled by the printing time gap between extruded layers. In most of the reported research [16,17,20,63,221], there has been agreement that tensile bond strength decreases with an increase in the printing time gap. This effect would become more pronounced for large, printed areas.

Sanjayan et al. [222] suggested that in 10- and 30-min time gaps, the bond strength of the printed specimens appears to be higher than a 20-min time gap. Extra tests of surface moisture content and bleeding rates were conducted to investigate the relationship between the printing time gap and the interlayer bond strength. It was shown that initially, high bond strength could be attributed to a high moisture level from a lubricating layer near the surface of the extruded paste, but bond strength then decreases during the time gap with the evaporation of the surface moisture. After an increase in the bleeding rate from 20- to 30-min

`

time gaps, a rise of surface moisture leads to the increased bond strength. It was concluded that the evolution of surface moisture content over time controls interlayer bond strength development in 3D printed concrete [222]. Previous findings indicate that moisture condition at the existing layer is related to the time gap that controls bond development at 3D printed concrete.

This proposed research builds on the above previous findings but suggests that the interlayer bond development is strongly dependent on the moisture transport phenomenon at the interface. Further research to understand the moisture transport process across the interface of 3D printed concrete and its influence on interlayer bond development is proposed.

Since rheological control of the 3D printable material during the manufacturing process is so important, a smart cement-based magnetorheological (MR) 3D printing material could be tailor-designed to yield the desired rheological properties of cement paste in real-time is suggested. By incorporating magnetic particles inside the cement paste and varying the magnitude of the magnetic field strength, the rheological response of the sample can be altered significantly. This cement-based MR fluid would allow for better control over the stiffening/setting behavior of concrete and can be helpful in applications in which controlling the fresh-state behavior of concrete is critical. There are research precedents of this technology being tested for cement pastes [223–225].

Furthermore, the development of an analytical model to predict the behavior of the structure during the extrusion process and its evolution over time is suggested. The model should account for the mix's fresh mechanical properties[54] and the rheological properties of the mix so that the model provides valuable information about the suitability of a material for 3D

printing [226]. The model should also account for the material non-linearity (plastic flow) and the geometrical non-linearity (buckling).

As an integral end target of the thesis, a segmental construction of prefabricated 3D printed components for a pedestrian bridge is suggested. Segmental construction is one of the fastest construction techniques, and it is widely used for building applications such as accelerated bridge construction (ABC). These prefabricated parts are prone to be created by using additive manufacturing technologies. To do so, the study of the structural behavior of a segmental 3D printed large-scale concrete beam with post-tensioned strands is proposed. The structural response under combined flexure and shear should be carefully inspected. Furthermore, structural properties such as density, modulus of elasticity, compressive and tensile strength should be analyzed. Also, long-term properties such as creep and shrinkage that could gradually reduce the prestressed loads of external active reinforcement systems should be calculated and accounted for overtime. The union between precast concrete segments for large structures such as bridges consists of dry joints with multiple shear keys [227,228]. The use of epoxy resins is usually avoided since it slows the process, causing delays. This construction technique using dry joints is commonly used in prestressed bridges [229].

The theory to evaluate the shear strength of resin-free dry joints with shear keys assumes that the shear stresses are transmitted across the joint through two different mechanisms [230,231]. The first mechanism represents the friction resistance between two rough compressed surfaces. This friction is proportional to the actuating compression, and the corresponding proportionality factor is called the friction coefficient, μ_1. The second

`

mechanism considers the support effect of the mechanical shear keys. These keys permit the shear transfer when there is contact between them [230–232].

A large-scale 3D printed, post-tensioned beam can be manufactured and mechanically tested up to failure as future work. The results should be compared to a reference traditionally casted beam design of the same geometry. The beam could be manufactured by 3D printing segments, including ducts to accommodate longitudinal reinforcement and strands. Stirrups will be embedded between layers as needed by design. Continuous 3D printed shear keys will be implemented in the design at the points of maximum shear flow (mid-point in the vertical direction).

The failure mechanisms, strength, and ductility governing a 3D printed large-scale structure would be identified and compared with the reference values for a traditionally manufactured beam. A combination of shear with joint opening failure is expected, but failure modes inherent to the manufacturing process could happen. Macroscale failure modes and patterns will be recognized, and the mechanical properties will be analyzed. The final goal is to highlight practical challenges that need to be overcome to implement this technology at a large scale for infrastructure applications.

`

References

[1] D.L. Bourell, J.J. Beaman, M.C. Leu, D.W. Rosen, A brief history of additive manufacturing and the 2009 roadmap for additive manufacturing: looking back and looking ahead, Proc. RapidTech. (2009) 24–25.

[2] M.O. John, Photo-glyph recording, US2775758A, 1956. https://patents.google.com/patent/US2775758A/en (accessed June 29, 2021).

[3] W.K. Swainson, Method, medium and apparatus for producing three-dimensional figure product, US4041476A, 1977. https://patents.google.com/patent/US4041476A/en (accessed June 29, 2021).

[4] R.F. Housholder, Molding process, US4247508A, 1981. https://patents.google.com/patent/US4247508A/en (accessed June 29, 2021).

[5] H. Kodama, Automatic method for fabricating a three-dimensional plastic model with photo-hardening polymer, Rev. Sci. Instrum. 52 (1981) 1770–1773. https://doi.org/10.1063/1.1136492.

[6] ISO / ASTM52900 - 15 Standard Terminology for Additive Manufacturing – General Principles – Terminology, (n.d.). https://www-astm-org.libproxy.unm.edu/Standards/ISOASTM52900.htm (accessed June 29, 2021).

[7] W. Gao, Y. Zhang, D. Ramanujan, K. Ramani, Y. Chen, C.B. Williams, C.C.L. Wang, Y.C. Shin, S. Zhang, P.D. Zavattieri, The status, challenges, and future of additive manufacturing in engineering, Comput.-Aided Des. 69 (2015) 65–89. https://doi.org/10.1016/j.cad.2015.04.001.

`

[8] J.-P. Kruth, M.C. Leu, T. Nakagawa, Progress in Additive Manufacturing and Rapid Prototyping, CIRP Ann. 47 (1998) 525–540. https://doi.org/10.1016/S0007-8506(07)63240-5.

[9] J.R.C. Dizon, A.H. Espera, Q. Chen, R.C. Advincula, Mechanical characterization of 3D-printed polymers, Addit. Manuf. 20 (2018) 44–67. https://doi.org/10.1016/j.addma.2017.12.002.

[10] I. Campbell, O. Diegel, J. Kowen, T. Wohlers, Wohlers Report 2018: 3D printing and additive manufacturing state of the industry: Annual Worldwide Progress Report, Wohlers Associates, 2018. https://researchspace.auckland.ac.nz/handle/2292/46627 (accessed June 29, 2021).

[11] R.A. Buswell, W.R. Leal de Silva, S.Z. Jones, J. Dirrenberger, 3D printing using concrete extrusion: A roadmap for research, Cem. Concr. Res. 112 (2018) 37–49. https://doi.org/10.1016/j.cemconres.2018.05.006.

[12] N. Labonnote, A. Rønnquist, B. Manum, P. Rüther, Additive construction: State-of-the-art, challenges and opportunities, Autom. Constr. 72 (2016) 347–366. https://doi.org/10.1016/j.autcon.2016.08.026.

[13] P.M. Teicholz, Labor-productivity declines in the construction industry: causes and remedies (a second look), AECbytes Viewp. (2013).

[14] P.K. Mehta, Concrete. Structure, Properties and Materials, (1986). https://trid.trb.org/view/273357 (accessed March 3, 2019).

[15] M. Moini, J. Olek, J.P. Youngblood, B. Magee, P.D. Zavattieri, Additive Manufacturing and Performance of Architectured Cement-Based Materials, Adv. Mater. 30 (2018) 1802123. https://doi.org/10.1002/adma.201802123.

`

[16] T.T. Le, S.A. Austin, S. Lim, R.A. Buswell, R. Law, A.G.F. Gibb, T. Thorpe, Hardened properties of high-performance printing concrete, Cem. Concr. Res. 42 (2012) 558–566. https://doi.org/10.1016/j.cemconres.2011.12.003.

[17] B. Panda, S.C. Paul, N.A.N. Mohamed, Y.W.D. Tay, M.J. Tan, Measurement of tensile bond strength of 3D printed geopolymer mortar, Measurement. 113 (2018) 108–116. https://doi.org/10.1016/j.measurement.2017.08.051.

[18] E. Keita, H. Bessaies-Bey, W. Zuo, P. Belin, N. Roussel, Weak bond strength between successive layers in extrusion-based additive manufacturing: measurement and physical origin, Cem. Concr. Res. 123 (2019) 105787. https://doi.org/10.1016/j.cemconres.2019.105787.

[19] V.N. Nerella, S. Hempel, V. Mechtcherine, Effects of layer-interface properties on mechanical performance of concrete elements produced by extrusion-based 3D-printing, Constr. Build. Mater. 205 (2019) 586–601. https://doi.org/10.1016/j.conbuildmat.2019.01.235.

[20] B. Panda, S.C. Paul, L.J. Hui, Y.W.D. Tay, M.J. Tan, Additive manufacturing of geopolymer for sustainable built environment, J. Clean. Prod. 167 (2017) 281–288. https://doi.org/10.1016/j.jclepro.2017.08.165.

[21] Y. Zhang, Y. Zhang, W. She, L. Yang, G. Liu, Y. Yang, Rheological and harden properties of the high-thixotropy 3D printing concrete, Constr. Build. Mater. 201 (2019) 278–285. https://doi.org/10.1016/j.conbuildmat.2018.12.061.

[22] P. Bedarf, A. Dutto, M. Zanini, B. Dillenburger, Foam 3D printing for construction: A review of applications, materials, and processes, Autom. Constr. 130 (2021) 103861. https://doi.org/10.1016/j.autcon.2021.103861.

`

[23] S. Lim, R.A. Buswell, T.T. Le, S.A. Austin, A.G.F. Gibb, T. Thorpe, Developments in construction-scale additive manufacturing processes, Autom. Constr. 21 (2012) 262–268. https://doi.org/10.1016/j.autcon.2011.06.010.

[24] B. Berman, 3-D printing: The new industrial revolution, Bus. Horiz. 55 (2012) 155–162. https://doi.org/10.1016/j.bushor.2011.11.003.

[25] S.C. Paul, G.P.A.G. van Zijl, M.J. Tan, I. Gibson, A review of 3D concrete printing systems and materials properties: current status and future research prospects, Rapid Prototyp. J. 24 (2018) 784–798. https://doi.org/10.1108/RPJ-09-2016-0154.

[26] E. Lloret, A.R. Shahab, M. Linus, R.J. Flatt, F. Gramazio, M. Kohler, S. Langenberg, Complex concrete structures: merging existing casting techniques with digital fabrication, Comput.-Aided Des. 60 (2015) 40–49.

[27] J. Xiao, G. Ji, Y. Zhang, G. Ma, V. Mechtcherine, J. Pan, L. Wang, T. Ding, Z. Duan, S. Du, Large-scale 3D printing concrete technology: Current status and future opportunities, Cem. Concr. Compos. 122 (2021) 104115. https://doi.org/10.1016/j.cemconcomp.2021.104115.

[28] V.N. Nerella, M. Krause, V. Mechtcherine, Direct printing test for buildability of 3D-printable concrete considering economic viability, Autom. Constr. 109 (2020) 102986. https://doi.org/10.1016/j.autcon.2019.102986.

[29] E.L. Kreiger, M.A. Kreiger, M.P. Case, Development of the construction processes for reinforced additively constructed concrete, Addit. Manuf. 28 (2019) 39–49. https://doi.org/10.1016/j.addma.2019.02.015.

[30] B. García de Soto, I. Agustí-Juan, J. Hunhevicz, S. Joss, K. Graser, G. Habert, B.T. Adey, Productivity of digital fabrication in construction: Cost and time analysis of a

robotically built wall, Autom. Constr. 92 (2018) 297–311. https://doi.org/10.1016/j.autcon.2018.04.004.

[31] G.A. Pacillo, G. Ranocchiai, F. Loccarini, M. Fagone, Additive manufacturing in construction: A review on technologies, processes, materials, and their applications of 3D and 4D printing, Mater. Des. Process. Commun. n/a (n.d.). https://doi.org/10.1002/mdp2.253.

[32] M. Benedetti, A. du Plessis, R.O. Ritchie, M. Dallago, S.M.J. Razavi, F. Berto, Architected cellular materials: A review on their mechanical properties towards fatigue-tolerant design and fabrication, Mater. Sci. Eng. R Rep. 144 (2021) 100606. https://doi.org/10.1016/j.mser.2021.100606.

[33] D. Lowke, E. Dini, A. Perrot, D. Weger, C. Gehlen, B. Dillenburger, Particle-bed 3D printing in concrete construction – Possibilities and challenges, Cem. Concr. Res. 112 (2018) 50–65. https://doi.org/10.1016/j.cemconres.2018.05.018.

[34] B. Khoshnevis, D. Hwang, K.-T. Yao, Z. Yeh, Mega-scale fabrication by Contour Crafting, Int. J. Ind. Syst. Eng. 1 (2006) 301–320. https://doi.org/10.1504/IJISE.2006.009791.

[35] S. Lim, T. Le, J. Webster, R. Buswell, A. Austin, A. Gibb, T. Thorpe, Fabricating construction components using layered manufacturing technology, in: Glob. Innov. Constr. Conf., Loughborough University, 2009: pp. 512–520.

[36] N. Hack, K. Dörfler, A.N. Walzer, T. Wangler, J. Mata-Falcón, N. Kumar, J. Buchli, W. Kaufmann, R.J. Flatt, F. Gramazio, M. Kohler, Structural stay-in-place formwork for robotic in situ fabrication of non-standard concrete structures: A real scale

architectural demonstrator, Autom. Constr. 115 (2020) 103197. https://doi.org/10.1016/j.autcon.2020.103197.

[37] M.S. Khan, F. Sanchez, H. Zhou, 3-D printing of concrete: Beyond horizons, Cem. Concr. Res. 133 (2020) 106070. https://doi.org/10.1016/j.cemconres.2020.106070.

[38] M.T. Souza, I.M. Ferreira, E. Guzi de Moraes, L. Senff, A.P. Novaes de Oliveira, 3D printed concrete for large-scale buildings: An overview of rheology, printing parameters, chemical admixtures, reinforcements, and economic and environmental prospects, J. Build. Eng. 32 (2020) 101833. https://doi.org/10.1016/j.jobe.2020.101833.

[39] S.M.E. Sepasgozar, A. Shi, L. Yang, S. Shirowzhan, D.J. Edwards, Additive Manufacturing Applications for Industry 4.0: A Systematic Critical Review, Buildings. 10 (2020) 231. https://doi.org/10.3390/buildings10120231.

[40] A. Siddika, M.A.A. Mamun, W. Ferdous, A.K. Saha, R. Alyousef, 3D-printed concrete: applications, performance, and challenges, J. Sustain. Cem.-Based Mater. 9 (2020) 127–164. https://doi.org/10.1080/21650373.2019.1705199.

[41] S. Reichenbach, B. Kromoser, State of practice of automation in precast concrete production, J. Build. Eng. 43 (2021) 102527. https://doi.org/10.1016/j.jobe.2021.102527.

[42] B. Khoshnevis, R. Dutton, Innovative Rapid Prototyping Process Makes Large Sized, Smooth Surfaced Complex Shapes in a Wide Variety of Materials, Mater. Technol. 13 (1998) 53–56. https://doi.org/10.1080/10667857.1998.11752766.

`

[43] T.T. Le, S.A. Austin, S. Lim, R.A. Buswell, A.G.F. Gibb, T. Thorpe, Mix design and fresh properties for high-performance printing concrete, Mater. Struct. 45 (2012) 1221–1232. https://doi.org/10.1617/s11527-012-9828-z.

[44] F. Bos, R. Wolfs, Z. Ahmed, T. Salet, Additive manufacturing of concrete in construction: potentials and challenges of 3D concrete printing, Virtual Phys. Prototyp. 11 (2016) 209–225. https://doi.org/10.1080/17452759.2016.1209867.

[45] T.A.M. Salet, F.P. Bos, R.J.M. Wolfs, Z.Y. Ahmed, 3D concrete printing – a structural engineering perspective, in: High Tech Concr. Technol. Eng. Meet Proc. 2017 Fib Symp. Held Maastricht Neth. June 12–14 2017, Springer, 2017: pp. xliii–lvii. https://doi.org/10.1007/978-3-319-59471-2.

[46] G. De Schutter, K. Lesage, V. Mechtcherine, V.N. Nerella, G. Habert, I. Agusti-Juan, Vision of 3D printing with concrete — Technical, economic and environmental potentials, Cem. Concr. Res. 112 (2018) 25–36. https://doi.org/10.1016/j.cemconres.2018.06.001.

[47] M.K. Mohan, A.V. Rahul, G. De Schutter, K. Van Tittelboom, Extrusion-based concrete 3D printing from a material perspective: A state-of-the-art review, Cem. Concr. Compos. 115 (2021) 103855. https://doi.org/10.1016/j.cemconcomp.2020.103855.

[48] J. Pegna, Exploratory investigation of solid freeform construction, Autom. Constr. 5 (1997) 427–437. https://doi.org/10.1016/S0926-5805(96)00166-5.

[49] G. Cesaretti, E. Dini, X. De Kestelier, V. Colla, L. Pambaguian, Building components for an outpost on the Lunar soil by means of a novel 3D printing technology, Acta Astronaut. 93 (2014) 430–450. https://doi.org/10.1016/j.actaastro.2013.07.034.

`

[50] N. Roussel, Understanding the Rheology of Concrete, Elsevier, 2011.

[51] L. Reiter, T. Wangler, N. Roussel, R.J. Flatt, The role of early age structural build-up in digital fabrication with concrete, Cem. Concr. Res. 112 (2018) 86–95. https://doi.org/10.1016/j.cemconres.2018.05.011.

[52] L.K. Mettler, F.K. Wittel, R.J. Flatt, H.J. Herrmann, Evolution of strength and failure of SCC during early hydration, Cem. Concr. Res. 89 (2016) 288–296. https://doi.org/10.1016/j.cemconres.2016.09.004.

[53] N. Roussel, Rheological requirements for printable concretes, Cem. Concr. Res. 112 (2018) 76–85. https://doi.org/10.1016/j.cemconres.2018.04.005.

[54] R.J.M. Wolfs, F.P. Bos, T.A.M. Salet, Early age mechanical behaviour of 3D printed concrete: Numerical modelling and experimental testing, Cem. Concr. Res. 106 (2018) 103–116. https://doi.org/10.1016/j.cemconres.2018.02.001.

[55] N. Roussel, A thixotropy model for fresh fluid concretes: Theory, validation and applications, Cem. Concr. Res. 36 (2006) 1797–1806. https://doi.org/10.1016/j.cemconres.2006.05.025.

[56] N. Roussel, G. Ovarlez, S. Garrault, C. Brumaud, The origins of thixotropy of fresh cement pastes, Cem. Concr. Res. 42 (2012) 148–157. https://doi.org/10.1016/j.cemconres.2011.09.004.

[57] D. Marchon, S. Kawashima, H. Bessaies-Bey, S. Mantellato, S. Ng, Hydration and rheology control of concrete for digital fabrication: Potential admixtures and cement chemistry, Cem. Concr. Res. 112 (2018) 96–110. https://doi.org/10.1016/j.cemconres.2018.05.014.

`

[58] R.J.M. Wolfs, F.P. Bos, T.A.M. Salet, Hardened properties of 3D printed concrete: The influence of process parameters on interlayer adhesion, Cem. Concr. Res. 119 (2019) 132–140. https://doi.org/10.1016/j.cemconres.2019.02.017.

[59] X. Hui-cai, L. Geng-ying, X. Guang-jing, Microstructure model of the interfacial zone between fresh and old concrete, J. Wuhan Univ. Technol.-Mater Sci Ed. 17 (2002) 64–68. https://doi.org/10.1007/BF02838421.

[60] V. Colla, E. Dini, Large scale 3D printing: From deep sea to the moon, Low-Cost 3D Print. Sci. Educ. Sustain. Dev. Canessa E Fonda C Zennaro M Eds. (2013) 127–132.

[61] P. Wu, J. Wang, X. Wang, A critical review of the use of 3-D printing in the construction industry, Autom. Constr. 68 (2016) 21–31. https://doi.org/10.1016/j.autcon.2016.04.005.

[62] A.R. Torrado, D.A. Roberson, Failure Analysis and Anisotropy Evaluation of 3D-Printed Tensile Test Specimens of Different Geometries and Print Raster Patterns, J. Fail. Anal. Prev. 16 (2016) 154–164. https://doi.org/10.1007/s11668-016-0067-4.

[63] Y.W.D. Tay, G.H.A. Ting, Y. Qian, B. Panda, L. He, M.J. Tan, Time gap effect on bond strength of 3D-printed concrete, Virtual Phys. Prototyp. (2018) 1–10. https://doi.org/10.1080/17452759.2018.1500420.

[64] B. Zareiyan, B. Khoshnevis, Effects of interlocking on interlayer adhesion and strength of structures in 3D printing of concrete, Autom. Constr. 83 (2017) 212–221. https://doi.org/10.1016/j.autcon.2017.08.019.

[65] T. Wangler, E. Lloret, L. Reiter, N. Hack, F. Gramazio, M. Kohler, M. Bernhard, B. Dillenburger, J. Buchli, N. Roussel, R. Flatt, Digital Concrete: Opportunities and

Challenges, RILEM Tech. Lett. 1 (2016) 67–75. https://doi.org/10.21809/rilemtechlett.2016.16.

[66] M. Fiebrich, Grundlagen der Adhäsionskunde, Dtsch. Aussch. Für Stahlbeton. 334 (1994) 75–90.

[67] P. Feng, X. Meng, J.-F. Chen, L. Ye, Mechanical properties of structures 3D printed with cementitious powders, Constr. Build. Mater. 93 (2015) 486–497. https://doi.org/10.1016/j.conbuildmat.2015.05.132.

[68] V.N. Nerella, S. Hempel, V. Mechtcherine, Micro-and macroscopic investigations on the interface between layers of 3d-printed cementitious elements, in: Proc. Int. Conf. Adv. Constr. Mater. Syst. Chennai India, 2017: pp. 3–8.

[69] B. Panda, S. Chandra Paul, M. Jen Tan, Anisotropic mechanical performance of 3D printed fiber reinforced sustainable construction material, Mater. Lett. 209 (2017) 146–149. https://doi.org/10.1016/j.matlet.2017.07.123.

[70] W.A. Megid, K.H. Khayat, Bond Strength in Multilayer Casting of Self-Consolidating Concrete, ACI Mater. J. 114 (2017). https://doi.org/10.14359/51689597.

[71] N. Roussel, F. Cussigh, Distinct-layer casting of SCC: The mechanical consequences of thixotropy, Cem. Concr. Res. 38 (2008) 624–632. https://doi.org/10.1016/j.cemconres.2007.09.023.

[72] Z.Y. Ahmed, F.P. Bos, R.J.M. Wolfs, T. a. M. Salet, Design considerations due to scale effects in 3D concrete printing, in: Proc. 8th Int. Conf. Arab Soc. Comput. Aided Archit. Des. ASCAAD 2016 Lond. U. K., 2016: pp. 1–10. https://research.tue.nl/en/publications/design-considerations-due-to-scale-effects-in-3d-concrete-printin (accessed March 4, 2019).

`

[73] S. Lim, R.A. Buswell, P.J. Valentine, D. Piker, S.A. Austin, X. De Kestelier, Modelling curved-layered printing paths for fabricating large-scale construction components, Addit. Manuf. 12 (2016) 216–230. https://doi.org/10.1016/j.addma.2016.06.004.

[74] R.J.M. Wolfs, F.P. Bos, E.C.F. van Strien, T.A.M. Salet, A Real-Time Height Measurement and Feedback System for 3D Concrete Printing, in: D.A. Hordijk, M. Luković (Eds.), High Tech Concr. Technol. Eng. Meet, Springer International Publishing, 2018: pp. 2474–2483.

[75] A. Perrot, D. Rangeard, A. Pierre, Structural built-up of cement-based materials used for 3D-printing extrusion techniques, Mater. Struct. 49 (2016) 1213–1220. https://doi.org/10.1617/s11527-015-0571-0.

[76] W. Ferdous, A. Manalo, T. Aravinthan, G. Van Erp, Properties of epoxy polymer concrete matrix: Effect of resin-to-filler ratio and determination of optimal mix for composite railway sleepers, Constr. Build. Mater. 124 (2016) 287–300. https://doi.org/10.1016/j.conbuildmat.2016.07.111.

[77] V. Toufigh, M. Hosseinali, S.M. Shirkhorshidi, Experimental study and constitutive modeling of polymer concrete's behavior in compression, Constr. Build. Mater. 112 (2016) 183–190. https://doi.org/10.1016/j.conbuildmat.2016.02.100.

[78] S.M. Daghash, E.M. Soliman, U.F. Kandil, M.M.R. Taha, Improving Impact Resistance of Polymer Concrete Using CNTs, Int. J. Concr. Struct. Mater. 10 (2016) 539–553. https://doi.org/10.1007/s40069-016-0165-4.

[79] M. Emiroglu, A.E. Douba, R.A. Tarefder, U.F. Kandil, M.R. Taha, New Polymer Concrete with Superior Ductility and Fracture Toughness Using Alumina

Nanoparticles, J. Mater. Civ. Eng. 29 (2017) 04017069. https://doi.org/10.1061/(ASCE)MT.1943-5533.0001894.

[80] A. Douba, M. Emiroglu, U.F. Kandil, M.M. Reda Taha, Very ductile polymer concrete using carbon nanotubes, Constr. Build. Mater. 196 (2019) 468–477. https://doi.org/10.1016/j.conbuildmat.2018.11.021.

[81] S.M. Daghash, R. Tarefder, M.M.R. Taha, A New Class of Carbon Nanotube: Polymer Concrete with Improved Fatigue Strength, in: K. Sobolev, S.P. Shah (Eds.), Nanotechnol. Constr., Springer International Publishing, Cham, 2015: pp. 285–290. https://doi.org/10.1007/978-3-319-17088-6_37.

[82] M. El-Hawary, H. Al-Khaiat, S. Fereig, Performance of epoxy-repaired concrete in a marine environment, Cem. Concr. Res. 30 (2000) 259–266. https://doi.org/10.1016/S0008-8846(99)00242-2.

[83] W. Ferdous, A. Manalo, A. Khennane, O. Kayali, Geopolymer concrete-filled pultruded composite beams – Concrete mix design and application, Cem. Concr. Compos. 58 (2015) 1–13. https://doi.org/10.1016/j.cemconcomp.2014.12.012.

[84] ACI Committee 548. (2009). Guide for the use of polymers in concrete, ACI 548. IR-09. Farmington Hills, MI: American Concrete Institute, (n.d.).

[85] M.M. Rueda, M.-C. Auscher, R. Fulchiron, T. Périé, G. Martin, P. Sonntag, P. Cassagnau, Rheology and applications of highly filled polymers: A review of current understanding, Prog. Polym. Sci. 66 (2017) 22–53. https://doi.org/10.1016/j.progpolymsci.2016.12.007.

[86] ACI Committee 548. (2019). Polymer Concrete: Guidelines for Structural Applications. Farmington Hills, MI: American Concrete Institute.548.6R-19:, (n.d.).

`

[87] J.P. Gorninski, D.C. Dal Molin, C.S. Kazmierczak, Study of the modulus of elasticity of polymer concrete compounds and comparative assessment of polymer concrete and portland cement concrete, Cem. Concr. Res. 34 (2004) 2091–2095. https://doi.org/10.1016/j.cemconres.2004.03.012.

[88] Rebeiz K. S., Serhal S. P., Craft A. P., Properties of Polymer Concrete Using Fly Ash, J. Mater. Civ. Eng. 16 (2004) 15–19. https://doi.org/10.1061/(ASCE)0899-1561(2004)16:1(15).

[89] M. Bărbuţă, M. Harja, I. Baran, Comparison of mechanical properties for polymer concrete with different types of filler, J. Mater. Civ. Eng. 22 (2010) 696–701.

[90] R. Bedi, R. Chandra, S.P. Singh, Mechanical Properties of Polymer Concrete, J. Compos. (2013). https://doi.org/10.1155/2013/948745.

[91] J.P. Gorninski, D.C. Dal Molin, C.S. Kazmierczak, Strength degradation of polymer concrete in acidic environments, Cem. Concr. Compos. 29 (2007) 637–645. https://doi.org/10.1016/j.cemconcomp.2007.04.001.

[92] J.-Z. Liang, Reinforcement and quantitative description of inorganic particulate-filled polymer composites, Compos. Part B Eng. 51 (2013) 224–232. https://doi.org/10.1016/j.compositesb.2013.03.019.

[93] J. Aghazadeh Mohandesi, A. Refahi, E. Sadeghi Meresht, S. Berenji, Effect of temperature and particle weight fraction on mechanical and micromechanical properties of sand-polyethylene terephthalate composites: A laboratory and discrete element method study, Compos. Part B Eng. 42 (2011) 1461–1467. https://doi.org/10.1016/j.compositesb.2011.04.048.

`

[94] A. Boudenne, L. Ibos, M. Fois, J.C. Majesté, E. Géhin, Electrical and thermal behavior of polypropylene filled with copper particles, Compos. Part Appl. Sci. Manuf. 36 (2005) 1545–1554. https://doi.org/10.1016/j.compositesa.2005.02.005.

[95] S. Takahashi, Y. Imai, A. Kan, Y. Hotta, H. Ogawa, Dielectric and thermal properties of isotactic polypropylene/hexagonal boron nitride composites for high-frequency applications, J. Alloys Compd. 615 (2014) 141–145. https://doi.org/10.1016/j.jallcom.2014.06.138.

[96] F. Danes, B. Garnier, T. Dupuis, Predicting, Measuring, and Tailoring the Transverse Thermal Conductivity of Composites from Polymer Matrix and Metal Filler, Int. J. Thermophys. 24 (2003) 771–784. https://doi.org/10.1023/A:1024096401779.

[97] F. Cavodeau, B. Otazaghine, R. Sonnier, J.-M. Lopez-Cuesta, C. Delaite, Fire retardancy of ethylene-vinyl acetate composites – Evaluation of synergistic effects between ATH and diatomite fillers, Polym. Degrad. Stab. 129 (2016) 246–259. https://doi.org/10.1016/j.polymdegradstab.2016.04.018.

[98] T. Tanaka, M. Kozako, K. Okamoto, Toward High Thermal Conductivity Nano Micro Epoxy Composites with Sufficient Endurance Voltage, J. Int. Counc. Electr. Eng. 2 (2012) 90–98. https://doi.org/10.5370/JICEE.2012.2.1.090.

[99] T. Xia, Y. Cao, N.A. Oyler, J. Murowchick, L. Liu, X. Chen, Strong Microwave Absorption of Hydrogenated Wide Bandgap Semiconductor Nanoparticles, ACS Appl. Mater. Interfaces. 7 (2015) 10407–10413. https://doi.org/10.1021/acsami.5b01598.

[100] R. Pal, Rheology of particulate dispersions and composites, CRC Press: Boca Raton, 2006.

`

[101] R.G. Larson, The structure and rheology of complex fluids, Oxford University Press: New York, 1999.

[102] D.M. Kalyon, S. Aktaş, Factors affecting the rheology and processability of highly filled suspensions, Annu. Rev. Chem. Biomol. Eng. 5 (2014) 229–254.

[103] J.S. Chong, E.B. Christiansen, A.D. Baer, Rheology of concentrated suspensions, J. Appl. Polym. Sci. 15 (1971) 2007–2021.

[104] A.B. Metzner, Rheology of Suspensions in Polymeric Liquids, J. Rheol. 29 (1985) 739–775. https://doi.org/10.1122/1.549808.

[105] H.A. Barnes, J.F. Hutton, K. Walters, An introduction to rheology, 1st ed., Elsevier Science B.V.: Amsterdam, 1989.

[106] A.V. Shenoy, Rheology of Filled Polymer Systems, Springer Science & Business Media: The Netherlands, 2013.

[107] M. Hambach, D. Volkmer, Properties of 3D-printed fiber-reinforced Portland cement paste, Cem. Concr. Compos. 79 (2017) 62–70. https://doi.org/10.1016/j.cemconcomp.2017.02.001.

[108] H. Abdel-Fattah, M.M. El-Hawary, Flexural behavior of polymer concrete, Constr. Build. Mater. 13 (1999) 253–262. https://doi.org/10.1016/S0950-0618(99)00030-6.

[109] A.E.F. de S. Almeida, E.P. Sichieri, Thermogravimetric analyses and mineralogical study of polymer modified mortar with silica fume, Mater. Res. 9 (2006) 321–326. https://doi.org/10.1590/S1516-14392006000300012.

[110] Y. Ohama, Mix Proportions and Properties of Polyester Resin Concretes, Spec. Publ. 40 (1973) 283–294. https://doi.org/10.14359/17394.

`

[111] A.J.M. Ferreira, C. Tavares, C. Ribeiro, Flexural Properties of Polyester Resin Concretes, J. Polym. Eng. 20 (2000) 459–468. https://doi.org/10.1515/POLYENG.2000.20.6.459.

[112] M.C.S. Ribeiro, C.M.L. Tavares, M. Figueiredo, A.J.M. Ferreira, A.A. Fernandes, Bending characteristics of resin concretes, Mater. Res. 6 (2003) 247–254. https://doi.org/10.1590/S1516-14392003000200021.

[113] M.C.S. Ribeiro, P.R. Nóvoa, A.J.M. Ferreira, A.T. Marques, Flexural performance of polyester and epoxy polymer mortars under severe thermal conditions, Cem. Concr. Compos. 26 (2004) 803–809. https://doi.org/10.1016/S0958-9465(03)00162-8.

[114] D. Heras Murcia, M. Genedy, M.M. Reda Taha, Examining the significance of infill printing pattern on the anisotropy of 3D printed concrete, Constr. Build. Mater. 262 (2020) 120559. https://doi.org/10.1016/j.conbuildmat.2020.120559.

[115] D. Asprone, C. Menna, F.P. Bos, T.A.M. Salet, J. Mata-Falcón, W. Kaufmann, Rethinking reinforcement for digital fabrication with concrete, Cem. Concr. Res. 112 (2018) 111–121. https://doi.org/10.1016/j.cemconres.2018.05.020.

[116] D. Asprone, F. Auricchio, C. Menna, V. Mercuri, 3D printing of reinforced concrete elements: Technology and design approach, Constr. Build. Mater. 165 (2018) 218–231. https://doi.org/10.1016/j.conbuildmat.2018.01.018.

[117] T. Marchment, J. Sanjayan, Mesh reinforcing method for 3D Concrete Printing, Autom. Constr. 109 (2020) 102992. https://doi.org/10.1016/j.autcon.2019.102992.

[118] B.N. Diggs-McGee, E.L. Kreiger, M.A. Kreiger, M.P. Case, Print time vs. elapsed time: A temporal analysis of a continuous printing operation for additive constructed

concrete, Addit. Manuf. 28 (2019) 205–214. https://doi.org/10.1016/j.addma.2019.04.008.

[119] T.A.M. Salet, Z.Y. Ahmed, F.P. Bos, H.L.M. Laagland, Design of a 3D printed concrete bridge by testing, Virtual Phys. Prototyp. 13 (2018) 222–236. https://doi.org/10.1080/17452759.2018.1476064.

[120] G. Vantyghem, W. De Corte, E. Shakour, O. Amir, 3D printing of a post-tensioned concrete girder designed by topology optimization, Autom. Constr. 112 (2020) 103084. https://doi.org/10.1016/j.autcon.2020.103084.

[121] M.M. Reda Taha, D. Heras Murcia, M.A. Najvani, 3D-Printed Segmental Concrete Structures and Methods of Making, 2020–090, n.d.

[122] Y.J. Nam, Y.K. Hwang, J.W. Park, Y.M. Lim, Chapter 4 - Fiber-Reinforced Cementitious Composite Design with Controlled Distribution and Orientation of Fibers Using Three-Dimensional Printing Technology, in: J.G. Sanjayan, A. Nazari, B. Nematollahi (Eds.), 3D Concr. Print. Technol., Butterworth-Heinemann, 2019: pp. 59–72. https://doi.org/10.1016/B978-0-12-815481-6.00004-X.

[123] B. Nematollahi, P. Vijay, J. Sanjayan, A. Nazari, M. Xia, V. Naidu Nerella, V. Mechtcherine, Effect of Polypropylene Fibre Addition on Properties of Geopolymers Made by 3D Printing for Digital Construction, Materials. 11 (2018) 2352. https://doi.org/10.3390/ma11122352.

[124] B. Nematollahi, M. Xia, J. Sanjayan, P. Vijay, Effect of Type of Fiber on Inter-Layer Bond and Flexural Strengths of Extrusion-Based 3D Printed Geopolymer, Mater. Sci. Forum. 939 (2018) 155–162. https://doi.org/10.4028/www.scientific.net/MSF.939.155.

`

[125] M. Hambach, H. Möller, T. Neumann, D. Volkmer, Portland cement paste with aligned carbon fibers exhibiting exceptionally high flexural strength (> 100MPa), Cem. Concr. Res. 89 (2016) 80–86. https://doi.org/10.1016/j.cemconres.2016.08.011.

[126] H. Ogura, V. Nerella, V. Mechtcherine, Developing and Testing of Strain-Hardening Cement-Based Composites (SHCC) in the Context of 3D-Printing, Materials. 11 (2018) 1375. https://doi.org/10.3390/ma11081375.

[127] F.P. Bos, Z.Y. Ahmed, R.J.M. Wolfs, T.A.M. Salet, 3D Printing Concrete with Reinforcement, in: D.A. Hordijk, M. Luković (Eds.), High Tech Concr. Technol. Eng. Meet, Springer International Publishing, 2018: pp. 2484–2493.

[128] F.P. Bos, Z.Y. Ahmed, E.R. Jutinov, T.A.M. Salet, Experimental Exploration of Metal Cable as Reinforcement in 3D Printed Concrete, Materials. 10 (2017) 1314. https://doi.org/10.3390/ma10111314.

[129] G. Ma, Z. Li, L. Wang, G. Bai, Micro-cable reinforced geopolymer composite for extrusion-based 3D printing, Mater. Lett. 235 (2019) 144–147. https://doi.org/10.1016/j.matlet.2018.09.159.

[130] J.H. Lim, B. Panda, Q.-C. Pham, Improving flexural characteristics of 3D printed geopolymer composites with in-process steel cable reinforcement, Constr. Build. Mater. 178 (2018) 32–41. https://doi.org/10.1016/j.conbuildmat.2018.05.010.

[131] T. Ding, J. Xiao, S. Zou, X. Zhou, Anisotropic behavior in bending of 3D printed concrete reinforced with fibers, Compos. Struct. 254 (2020) 112808. https://doi.org/10.1016/j.compstruct.2020.112808.

[132] C. Kulas, Actual applications and potential of textile-reinforced concrete, GRC 2015. (2015) 1–11.

`

[133] I.G. Lepenies, M. Richter, B.W. Zastrau, A Multi-Scale Analysis of Textile Reinforced Concrete Structures, PAMM. 8 (2008) 10553–10554. https://doi.org/10.1002/pamm.200810553.

[134] A. Volkova, A. Paykov, S. Semenov, O. Stolyarov, B. Melnikov, Flexural Behavior of Textile-Reinforced Concrete, MATEC Web Conf. 53 (2016) 01016. https://doi.org/10.1051/matecconf/20165301016.

[135] J. Žák, P. Štemberk, J. Vodička, Production of a textile reinforced concrete protective layers with non-woven polypropylene fabric, IOP Conf. Ser. Mater. Sci. Eng. 246 (2017) 012054. https://doi.org/10.1088/1757-899X/246/1/012054.

[136] T. Gries, M. Raina, T. Quadflieg, O. Stolyarov, Manufacturing of textiles for civil engineering applications, in: Text. Fibre Compos. Civ. Eng., Elsevier, 2016: pp. 3–24.

[137] N. Williams Portal, K. Lundgren, H. Wallbaum, K. Malaga, Sustainable potential of textile-reinforced concrete, J. Mater. Civ. Eng. 27 (2015) 04014207.

[138] T. Triantafillou, Textile fibre composites in civil engineering, Woodhead Publishing, 2016.

[139] A. Peled, A. Bentur, B. Mobasher, Textile reinforced concrete, CRC Press, 2017.

[140] Y. Du, X. Zhang, F. Zhou, D. Zhu, M. Zhang, W. Pan, Flexural behavior of basalt textile-reinforced concrete, Constr. Build. Mater. 183 (2018) 7–21. https://doi.org/10.1016/j.conbuildmat.2018.06.165.

[141] M. Abdel-Emam, E. Soliman, A. Nassr, W. Khair-Eldeen, A. Abd-Elshafy, Dynamic Behavior of Textile Reinforced Polymer Concrete Using Split Hopkinson Pressure Bar, in: M.M.R. Taha (Ed.), Int. Congr. Polym. Concr. ICPIC 2018, Springer

International Publishing, Cham, 2018: pp. 389–395. https://doi.org/10.1007/978-3-319-78175-4_49.

[142] A. Brückner, R. Ortlepp, M. Curbach, Textile reinforced concrete for strengthening in bending and shear, Mater. Struct. 39 (2006) 741–748.

[143] F. Schladitz, M. Frenzel, D. Ehlig, M. Curbach, Bending load capacity of reinforced concrete slabs strengthened with textile reinforced concrete, Eng. Struct. 40 (2012) 317–326. https://doi.org/10.1016/j.engstruct.2012.02.029.

[144] Z.C. Tetta, L.N. Koutas, D.A. Bournas, Textile-reinforced mortar (TRM) versus fiber-reinforced polymers (FRP) in shear strengthening of concrete beams, Compos. Part B Eng. 77 (2015) 338–348. https://doi.org/10.1016/j.compositesb.2015.03.055.

[145] C.G. Papanicolaou, T.C. Triantafillou, M. Papathanasiou, K. Karlos, Textile reinforced mortar (TRM) versus FRP as strengthening material of URM walls: out-of-plane cyclic loading, Mater. Struct. 41 (2008) 143–157. https://doi.org/10.1617/s11527-007-9226-0.

[146] S. De Santis, G. de Felice, Tensile behaviour of mortar-based composites for externally bonded reinforcement systems, Compos. Part B Eng. 68 (2015) 401–413. https://doi.org/10.1016/j.compositesb.2014.09.011.

[147] A. D'Ambrisi, L. Feo, F. Focacci, Experimental analysis on bond between PBO-FRCM strengthening materials and concrete, Compos. Part B Eng. 44 (2013) 524–532. https://doi.org/10.1016/j.compositesb.2012.03.011.

[148] J. Donnini, V. Corinaldesi, A. Nanni, Mechanical properties of FRCM using carbon fabrics with different coating treatments, Compos. Part B Eng. 88 (2016) 220–228. https://doi.org/10.1016/j.compositesb.2015.11.012.

`

[149] J. Hartig, U. Häußler-Combe, A model for the uniaxial tensile behaviour of Textile Reinforced Concrete with a stochastic description of the concrete material properties, Bicanic N Borst R Mang H. (2010) 153–162.

[150] A. Peled, A. Bentur, B. Mobasher, Textile reinforced concrete, CRC Press, 2017.

[151] U. Häußler-Combe, J. Hartig, Bond and failure mechanisms of textile reinforced concrete (TRC) under uniaxial tensile loading, Cem. Concr. Compos. 29 (2007) 279–289. https://doi.org/10.1016/j.cemconcomp.2006.12.012.

[152] U. Häußler-Combe, F. Jesse, M. Curbach, Textile reinforced concrete-overview, experimental and theoretical investigations, in: Fract. Mech. Concr. Struct. Proc. Fifth Int. Conf. Fract. Mech. Concr. Concr. Struct. Ia-Fram. Vail CO USA, 2004: pp. 12–16.

[153] G. Wu, X. Wang, Z. Wu, Z. Dong, G. Zhang, Durability of basalt fibers and composites in corrosive environments, J. Compos. Mater. 49 (2015) 873–887. https://doi.org/10.1177/0021998314526628.

[154] D.W. Fowler, Polymers in concrete: a vision for the 21st century, Cem. Concr. Compos. 21 (1999) 449–452. https://doi.org/10.1016/S0958-9465(99)00032-3.

[155] B. Chmielewska, L. Czarnecki, J. Sustersic, A. Zajc, The influence of silane coupling agents on the polymer mortar, Cem. Concr. Compos. 28 (2006) 803–810. https://doi.org/10.1016/j.cemconcomp.2006.04.005.

[156] K. Chrissafis, D. Bikiaris, Can nanoparticles really enhance thermal stability of polymers? Part I: An overview on thermal decomposition of addition polymers, Thermochim. Acta. 523 (2011) 1–24. https://doi.org/10.1016/j.tca.2011.06.010.

[157] A.A. Wereszczak, T.G. Morrissey, C.N. Volante, P.J. Farris, R.J. Groele, R.H. Wiles, H. Wang, Thermally Conductive MgO-Filled Epoxy Molding Compounds, IEEE

Trans. Compon. Packag. Manuf. Technol. 3 (2013) 1994–2005. https://doi.org/10.1109/TCPMT.2013.2281212.

[158] B. Olalla, C. Carrot, R. Fulchiron, I. Boudimbou, E. Peuvrel-disdier, Analysis of the influence of polymer viscosity on the dispersion of magnesium hydroxide in a polyolefin matrix, Rheol. Acta. 51 (2012) 235–247. https://doi.org/10.1007/s00397-011-0580-z.

[159] Mechanical properties of Mg(OH)2/polypropylene composites modified by functionalized polypropylene - Mai - 2003 - Journal of Applied Polymer Science - Wiley Online Library, (n.d.). https://onlinelibrary.wiley.com/doi/full/10.1002/app.11762 (accessed March 11, 2020).

[160] C09 Committee, Specification for Chemical Admixtures for Concrete, ASTM International, n.d. https://doi.org/10.1520/C0494_C0494M-19.

[161] Y. Zhang, Y. Zhang, G. Liu, Y. Yang, M. Wu, B. Pang, Fresh properties of a novel 3D printing concrete ink, Constr. Build. Mater. 174 (2018) 263–271. https://doi.org/10.1016/j.conbuildmat.2018.04.115.

[162] BS EN 12390-3:2019 - Testing hardened concrete. Compressive strength of test specimens, (n.d.). https://shop.bsigroup.com/ProductDetail/?pid=000000000030360097 (accessed May 17, 2020).

[163] C09 Committee, Practice for Making and Curing Concrete Test Specimens in the Field, ASTM International, n.d. https://doi.org/10.1520/C0031_C0031M-19A.

[164] C09 Committee, Practice for Estimating Concrete Strength by the Maturity Method, ASTM International, n.d. https://doi.org/10.1520/C1074-19.

`

[165] D01 Committee, Test Methods for Rheological Properties of Non-Newtonian Materials by Rotational Viscountess, ASTM International, n.d. https://doi.org/10.1520/D2196-18E01.

[166] D18 Committee, Test Method for Field Vane Shear Test in Saturated Fine-Grained Soils, ASTM International, n.d. https://doi.org/10.1520/D2573_D2573M-18.

[167] R.N. Weltmann, H. Green, Rheological Properties of Colloidal Solutions, Pigment Suspensions, and Oil Mixtures, J. Appl. Phys. 14 (1943) 569–576. https://doi.org/10.1063/1.1714935.

[168] W.-J. Long, J.-L. Tao, C. Lin, Y. Gu, L. Mei, H.-B. Duan, F. Xing, Rheology and buildability of sustainable cement-based composites containing micro-crystalline cellulose for 3D-printing, J. Clean. Prod. 239 (2019) 118054. https://doi.org/10.1016/j.jclepro.2019.118054.

[169] C01 Committee, Test Methods for Time of Setting of Hydraulic Cement by Vicat Needle, ASTM International, n.d. https://doi.org/10.1520/C0191-18A.

[170] C09 Committee, Test Method for Slump of Hydraulic-Cement Concrete, ASTM International, n.d. https://doi.org/10.1520/C0143_C0143M-15A.

[171] D30 Committee, Test Method for Short-Beam Strength of Polymer Matrix Composite Materials and Their Laminates, ASTM International, n.d. https://doi.org/10.1520/D2344_D2344M-16.

[172] D.A. Williams, A.W. Saak, H.M. Jennings, The influence of mixing on the rheology of fresh cement paste, Cem. Concr. Res. 29 (1999) 1491–1496. https://doi.org/10.1016/S0008-8846(99)00124-6.

`

[173] J. Mewis, N.J. Wagner, Thixotropy, Adv. Colloid Interface Sci. 147–148 (2009) 214–227. https://doi.org/10.1016/j.cis.2008.09.005.

[174] ASTM C618-19, Specification for Coal Fly Ash and Raw or Calcined Natural Pozzolan for Use in Concrete, ASTM International, n.d. https://doi.org/10.1520/C0618-19.

[175] D. Heras Murcia, 3D-Printed Polymer Concrete for Infrastructure Applications, in: ICIMART 2019, n.d.

[176] D18 Committee, Test Method for Laboratory Miniature Vane Shear Test for SaturatedFine-Grained Clayey Soil, ASTM International, n.d. https://doi.org/10.1520/D4648_D4648M-16.

[177] V.W.H. Herschel, Consistency of Measurements Rubber-Benzene Solutions, Kolloid-Zeit. 39 (1926) 291–300.

[178] R.S. Campos, G.F. Maciel, Test protocol and rheological model influence on determining the rheological properties of cement pastes, J. Build. Eng. (2021) 103206. https://doi.org/10.1016/j.jobe.2021.103206.

[179] J. Yan, A.E. James, The yield surface of viscoelastic and plastic fluids in a vane viscometer, J. Non-Newton. Fluid Mech. 70 (1997) 237–253. https://doi.org/10.1016/S0377-0257(97)00005-0.

[180] K.S. Rebeiz, Time-temperature properties of polymer concrete using recycled PET, Cem. Concr. Compos. 17 (1995) 119–124. https://doi.org/10.1016/0958-9465(94)00004-I.

`

[181] K.S. Rebeiz, Precast use of polymer concrete using unsaturated polyester resin based on recycled PET waste, Constr. Build. Mater. 10 (1996) 215–220. https://doi.org/10.1016/0950-0618(95)00088-7.

[182] M.E. Tawfik, S.B. Eskander, Polymer Concrete from Marble Wastes and Recycled Poly(ethylene terephthalate), J. Elastomers Plast. 38 (2006) 65–79. https://doi.org/10.1177/0095244306055569.

[183] Y. Ohama, K. Demura, Relation between curing conditions and compressive strength of polyester resin concrete, Int. J. Cem. Compos. Lightweight Concr. 4 (1982) 241–244. https://doi.org/10.1016/0262-5075(82)90028-8.

[184] ASTM C109/C109M-20b., Test Method for Compressive Strength of Hydraulic Cement Mortars (Using 2-in. or [50-mm] Cube Specimens), ASTM International, n.d. https://doi.org/10.1520/C0109_C0109M-20B.

[185] G.J. Dienes, Flow properties of phenolic resins, J. Colloid Sci. 4 (1949) 257–264. https://doi.org/10.1016/0095-8522(49)90008-2.

[186] Y. Qian, S. Kawashima, Distinguishing dynamic and static yield stress of fresh cement mortars through thixotropy, Cem. Concr. Compos. 86 (2018) 288–296. https://doi.org/10.1016/j.cemconcomp.2017.11.019.

[187] D.C.-H. Cheng, Yield stress: A time-dependent property and how to measure it, Rheol. Acta. 25 (1986) 542–554. https://doi.org/10.1007/BF01774406.

[188] E.M. Soliman, U.F. Kandil, M.M.R. Taha, The significance of carbon nanotubes on styrene butadiene rubber (SBR) and SBR modified mortar, Mater. Struct. (2012) 803.

`

[189] W. Meng, K.H. Khayat, Effect of graphite nanoplatelets and carbon nanofibers on rheology, hydration, shrinkage, mechanical properties, and microstructure of UHPC, Cem. Concr. Res. 105 (2018) 64–71. https://doi.org/10.1016/j.cemconres.2018.01.001.

[190] ASTM C1437-20, C01 Committee, Test Method for Flow of Hydraulic Cement Mortar, ASTM International, West Conshohocken, PA, USA, 2020, n.d. https://doi.org/10.1520/C1437-20.

[191] ASTM C39-17b, C09 Committee, Standard Test Method for Compressive Strength of Cylindrical Concrete Specimens, ASTM International: West Conshohocken, PA, USA, 2017., n.d. https://doi.org/10.1520/C0039_C0039M-20.

[192] C. Başyiğit, B. Çomak, Ş. Kılınçarslan, İ. Serkan Üncü, Assessment of concrete compressive strength by image processing technique, Constr. Build. Mater. 37 (2012) 526–532. https://doi.org/10.1016/j.conbuildmat.2012.07.055.

[193] D. Rotolo, D. Hicks, B.R. Martin, What is an emerging technology?, Res. Policy. 44 (2015) 1827–1843. https://doi.org/10.1016/j.respol.2015.06.006.

[194] I. Tzinis, Technology Readiness Level, NASA. (2015). http://www.nasa.gov/directorates/heo/scan/engineering/technology/technology_readiness_level (accessed June 21, 2021).

[195] S.M. Moni, R. Mahmud, K. High, M. Carbajales-Dale, Life cycle assessment of emerging technologies: A review, J. Ind. Ecol. 24 (2020) 52–63. https://doi.org/10.1111/jiec.12965.

[196] Gartner Hype Cycle Research Methodology, Gartner. (n.d.). https://www.gartner.com/en/research/methodologies/gartner-hype-cycle (accessed June 21, 2021).

`

[197] J.D. Prince, 3D Printing: An Industrial Revolution, J. Electron. Resour. Med. Libr. 11 (2014) 39–45. https://doi.org/10.1080/15424065.2014.877247.

[198] M. Reda Taha, B.M. Ayyub, K. Soga, S. Daghash, D. Heras Murcia, F. Moreu, E. Soliman, Emerging Technologies for Resilient Infrastructure: Conspectus and Roadmap, ASCE-ASME J. Risk Uncertain. Eng. Syst. Part Civ. Eng. 7 (2021) 03121002. https://doi.org/10.1061/AJRUA6.0001134.

[199] B. Khoshnevis, Automated construction by contour crafting—related robotics and information technologies, Autom. Constr. 13 (2004) 5–19. https://doi.org/10.1016/j.autcon.2003.08.012.

[200] J. Zhang, B. Khoshnevis, Optimal machine operation planning for construction by Contour Crafting, Autom. Constr. 29 (2013) 50–67. https://doi.org/10.1016/j.autcon.2012.08.006.

[201] E. Barnett, C. Gosselin, Large-scale 3D printing with a cable-suspended robot, Addit. Manuf. 7 (2015) 27–44. https://doi.org/10.1016/j.addma.2015.05.001.

[202] P.G. Hubbard, Z. Chen, K. Soga, M. Reda Taha, D. Heras Murcia, P. Tang, B. Glisic, O. Ozbulut, C. Ford, A framework for evaluating emerging technologies' contributions to system resilience, Rev. (n.d.).

[203] H. Son, S. Lee, C. Kim, What drives the adoption of building information modeling in design organizations? An empirical investigation of the antecedents affecting architects' behavioral intentions, Autom. Constr. 49 (2015) 92–99. https://doi.org/10.1016/j.autcon.2014.10.012.

`

[204] D. Cao, H. Li, G. Wang, Impacts of Isomorphic Pressures on BIM Adoption in Construction Projects, J. Constr. Eng. Manag. 140 (2014) 04014056. https://doi.org/10.1061/(ASCE)CO.1943-7862.0000903.

[205] Adoption of New Technology | NBER, (n.d.). https://www.nber.org/papers/w9730 (accessed June 21, 2021).

[206] K. Soga, P.G. Hubbard, M. Reda Taha, Z. Chen, D. Heras Murcia, P. Tang, B. Glisic, O. Ozbulut, C. Ford, N. Lu, Y.-F. Su, Evaluation of emerging technologies for system resilience contributions: case studies, Rev. (n.d.).

[207] T. McDaniels, S. Chang, D. Cole, J. Mikawoz, H. Longstaff, Fostering resilience to extreme events within infrastructure systems: Characterizing decision contexts for mitigation and adaptation, Glob. Environ. Change. 18 (2008) 310–318. https://doi.org/10.1016/j.gloenvcha.2008.03.001.

[208] ASCE's 2021 American Infrastructure Report Card | GPA: C-, ASCEs 2021 Infrastruct. Rep. Card. (2017). https://infrastructurereportcard.org/ (accessed June 22, 2021).

[209] T. McDaniels, S. Chang, K. Peterson, J. Mikawoz, D. Reed, Empirical Framework for Characterizing Infrastructure Failure Interdependencies, J. Infrastruct. Syst. 13 (2007) 175–184. https://doi.org/10.1061/(ASCE)1076-0342(2007)13:3(175).

[210] B.M. Ayyub, Practical Resilience Metrics for Planning, Design, and Decision Making, ASCE-ASME J. Risk Uncertain. Eng. Syst. Part Civ. Eng. 1 (2015) 04015008. https://doi.org/10.1061/AJRUA6.0000826.

[211] M. Bruneau, S.E. Chang, R.T. Eguchi, G.C. Lee, T.D. O'Rourke, A.M. Reinhorn, M. Shinozuka, K. Tierney, W.A. Wallace, D. von Winterfeldt, A Framework to

Quantitatively Assess and Enhance the Seismic Resilience of Communities, Earthq. Spectra. 19 (2003) 733–752. https://doi.org/10.1193/1.1623497.

[212] G. Vantyghem, W. De Corte, E. Shakour, O. Amir, 3D printing of a post-tensioned concrete girder designed by topology optimization, Autom. Constr. 112 (2020) 103084. https://doi.org/10.1016/j.autcon.2020.103084.

[213] Y. Weng, M. Li, S. Ruan, T.N. Wong, M.J. Tan, K.L. Ow Yeong, S. Qian, Comparative economic, environmental and productivity assessment of a concrete bathroom unit fabricated through 3D printing and a precast approach, J. Clean. Prod. 261 (2020) 121245. https://doi.org/10.1016/j.jclepro.2020.121245.

[214] R. Pekuss, B. García de Soto, Preliminary Productivity Analysis of Conventional, Precast and 3D Printing Production Techniques for Concrete Columns with Simple Geometry, in: F.P. Bos, S.S. Lucas, R.J.M. Wolfs, T.A.M. Salet (Eds.), Second RILEM Int. Conf. Concr. Digit. Fabr., Springer International Publishing, Cham, 2020: pp. 1031–1050. https://doi.org/10.1007/978-3-030-49916-7_100.

[215] I. Linkov, D.A. Eisenberg, M.E. Bates, D. Chang, M. Convertino, J.H. Allen, S.E. Flynn, T.P. Seager, Measurable Resilience for Actionable Policy, Environ. Sci. Technol. 47 (2013) 10108–10110. https://doi.org/10.1021/es403443n.

[216] R.A. Davidson, Integrating disciplinary contributions to achieve community resilience to natural disasters, Civ. Eng. Environ. Syst. 32 (2015) 55–67. https://doi.org/10.1080/10286608.2015.1011627.

[217] R.A. Davidson, L.K. Nozick, T. Wachtendorf, B. Blanton, B. Colle, R.L. Kolar, S. DeYoung, K.M. Dresback, W. Yi, K. Yang, N. Leonardo, An Integrated Scenario

Ensemble-Based Framework for Hurricane Evacuation Modeling: Part 1—Decision Support System, Risk Anal. 40 (2020) 97–116. https://doi.org/10.1111/risa.12990.

[218] S. Cucurachi, C. van der Giesen, J. Guinée, Ex-ante LCA of Emerging Technologies, Procedia CIRP. 69 (2018) 463–468. https://doi.org/10.1016/j.procir.2017.11.005.

[219] Y. Jia, J. Yan, S. Du, T. Feng, P. Fidler, C. Middleton, K. Soga, A.A. Seshia, Real world assessment of an auto-parametric electromagnetic vibration energy harvester, J. Intell. Mater. Syst. Struct. 29 (2018) 1481–1499. https://doi.org/10.1177/1045389X17740964.

[220] K.T.Q. Nguyen, S. Navaratnam, P. Mendis, K. Zhang, J. Barnett, H. Wang, Fire safety of composites in prefabricated buildings: From fibre reinforced polymer to textile reinforced concrete, Compos. Part B Eng. 187 (2020) 107815. https://doi.org/10.1016/j.compositesb.2020.107815.

[221] R.J.M. Wolfs, F.P. Bos, T.A.M. Salet, Hardened properties of 3D printed concrete: The influence of process parameters on interlayer adhesion, Cem. Concr. Res. 119 (2019) 132–140. https://doi.org/10.1016/j.cemconres.2019.02.017.

[222] J.G. Sanjayan, B. Nematollahi, M. Xia, T. Marchment, Effect of surface moisture on inter-layer strength of 3D printed concrete, Constr. Build. Mater. 172 (2018) 468–475. https://doi.org/10.1016/j.conbuildmat.2018.03.232.

[223] D. Jiao, K. Lesage, M.Y. Yardimci, C. Shi, G. De Schutter, Possibilities of fly ash as responsive additive in magneto-rheology control of cementitious materials, Constr. Build. Mater. 296 (2021) 123656. https://doi.org/10.1016/j.conbuildmat.2021.123656.

`

[224] C. Krezinski, P. Panchmatia, M. Genedy, S. Nair, M. Juenger, C. Usher, E. van Oort, Magnetorheological cements for plug setting control in oil and gas wells, J. Pet. Sci. Eng. 200 (2021) 108257. https://doi.org/10.1016/j.petrol.2020.108257.

[225] S.D. Nair, R.D. Ferron, Real time control of fresh cement paste stiffening: Smart cement-based materials via a magnetorheological approach, Rheol. Acta. 55 (2016) 571–579. https://doi.org/10.1007/s00397-016-0923-x.

[226] J. Kruger, S. Zeranka, G. van Zijl, 3D concrete printing: A lower bound analytical model for buildability performance quantification, Autom. Constr. 106 (2019) 102904. https://doi.org/10.1016/j.autcon.2019.102904.

[227] J. Turmo, G. Ramos, A.C. Aparicio, FEM modelling of unbonded post-tensioned segmental beams with dry joints, Eng. Struct. 28 (2006) 1852–1863. https://doi.org/10.1016/j.engstruct.2006.03.028.

[228] J. Turmo, G. Ramos, A.C. Aparicio, Shear strength of dry joints of concrete panels with and without steel fibres, Eng. Struct. 28 (2006) 23–33. https://doi.org/10.1016/j.engstruct.2005.07.001.

[229] J. Muller, Construction of the long key bridge, J. Prestress. Concr. Inst. 25 (1980) 97–111.

[230] O. Buyukozturk, M.M. Bakhoum, S. Michael Beattie, Shear Behavior of Joints in Precast Concrete Segmental Bridges, J. Struct. Eng. 116 (1990) 3380–3401. https://doi.org/10.1061/(ASCE)0733-9445(1990)116:12(3380).

[231] G. Ramirez, R. MacGregor, M.E. Kreger, C. Roberts-Wollmann, J.E. Breen, Shear strength of segmental structures, in: Proc. Workshop AFPC Extern. Prestress. Struct. St.-Rémy-Lès-Chevreuse, 1993: pp. 287–296.

`

[232] A.C. Aparicio, G. Ramos, J.R. Casas, Testing of externally prestressed concrete beams, Eng. Struct. 24 (2002) 73–84. https://doi.org/10.1016/S0141-0296(01)00062-1.

`

Appendix

Cartesian Coordinate 3D Printer Technical Parameters

Technical parameters of JYHC 3D printing gantry robot system(3DPRT)		
Frame structure	Size: length (mm) * width (mm) * height (mm)	2800*2010*2600
	Weight (kg)	300
	Drive motor	Stepper motor, five
	Power supply	AC 220V
Mixing and feeding system	Shear mixer Capacity (L) Voltage (V) Power (W) Weight (kg)	 50 (recommended) (max 60) 380 AC 3000 300x2
	Pumping system Voltage (V) Power (W) Horizontal transmission distance (M) Transmission height (m) Weight (kg)	 380 AC 4000 15 5 180
	Transporting pipe: Material Length (m) Inner diameter (mm)	 Rubber 5 45
Motion control system	Effective size: length (mm) * width (mm) * height (mm)	1800*1600*1800
	XY Plane moving speed (mm/s)	10 to 350
	Z moving speed (mm/s)	10 to 20
Printing head	Diameter of printing head (mm)	25, 35, 45 mm
	The diameter of acrylic printing head(mm)	40 mm
	Ways of adding material	Manual (through the printing head) or automatic (pumping system)
Software	Software development environment	LabVIEW (reads from a G-Code)
	Interface text	English
	Software upgrade	Network transmission, Free of renew

Table 17. Technical parameters of JYHC 3D printing gantry robot system (3DPRT)

`

G-Code Programming Language Examples

In this appendix, numerical control programming examples used for Chapter 3 (and depicted in Figure 19) are shown.

[0]$_{12}$ Cube with Outline Perimeter

```
M109 S210.000000
;Sliced at: Mon 20-11-2017 12:24:19
;Basic settings: Layer height: 1
Walls: 1 Fill: 0
;Print time: 2 hours 43 minutes
;Filament used: 4.605m 36.0g
;Filament cost: None
;M190 S70 ;Uncomment to add your own
bed temperature line
;M109 S210 ;Uncomment to add your own
temperature line
G21        ;metric values
G90        ;absolute positioning
M82        ;set extruder to absolute
mode
M107       ;start with the fan off
G28 X0 Y0  ;move X/Y to min endstops
G28 Z0     ;move Z to min endstops
G1 Z15.0 F9000 ;move the platform down
15mm
G92 E0                  ;zero the
extruded length
G1 F200 E3              ;extrude 3mm
of feed stock
G92 E0                  ;zero the
extruded length again
G1 F9000
;Put printing message on LCD screen
M117 Printing...

;Layer count: 3
;LAYER:0
M107

;LAYER:1
M106 S255
G0 F9000 X15.65 Y0.000  Z1.000
;TYPE:WALL-OUTER
G1 F2400 E0.00000

G1 X15.65 Y0.000 F4800

G1 X15.65 Y15.65 E1.000
G1 X1.15 Y15.65 E2.000
G1 X1.15 Y1.15 E3.000
G1 X15.65 Y1.15 E4.000
; solid layer

G0 X1.15 Y3.52 F4800

G1 X13.28 Y3.52 E1.000 F1007
G1 X13.28 Y5.96 E2.000
G1 X3.52 Y5.96 E3.000
G1 X3.52 Y8.4 E4.000
G1 X13.28 Y8.4 E5.000
G1 X13.28 Y10.84 E6.000
G1 X3.52 Y10.84 E7.000
G1 X3.52 Y13.28 E8.000
G1 X13.28 Y13.28 E9.000

;LAYER:2
M106 S255
G0 F9000 X15.65 Y0.000  Z2.000
;TYPE:WALL-OUTER
G1 F2400 E0.00000

G1 X15.65 Y0.000 F4800

G1 X15.65 Y15.65 E1.000
G1 X1.15 Y15.65 E2.000
G1 X1.15 Y1.15 E3.000
G1 X15.65 Y1.15 E4.000
; solid layer

G0 X1.15 Y3.52 F4800

G1 X13.28 Y3.52 E1.000 F1007
G1 X13.28 Y5.96 E2.000
G1 X3.52 Y5.96 E3.000
G1 X3.52 Y8.4 E4.000
G1 X13.28 Y8.4 E5.000
G1 X13.28 Y10.84 E6.000
G1 X3.52 Y10.84 E7.000
G1 X3.52 Y13.28 E8.000
G1 X13.28 Y13.28 E9.000


M107
;End GCode
M104 S0                     ;extruder
heater off
M140 S0                     ;heated
bed heater off (if you have it)
G91
;relative positioning
G1 E-1 F300
;retract the filament a bit before
lifting the nozzle, to release some of
the pressure
G1 Z+0.5 E-5 X-20 Y-20 F9000 ;move Z
up a bit and retract filament even
more
```

`

```
G28 X0 Y0
;move X/Y to min endstops, so the head
is out of the way
```

[0,90]$_6$ Cube with Outline Perimeter

```
M109 S210.000000
;Sliced at: Mon 20-11-2017 12:24:19
;Basic settings: Layer height: 1
Walls: 1 Fill: 0
;Print time: 2 hours 43 minutes
;Filament used: 4.605m 36.0g
;Filament cost: None
;M190 S70 ;Uncomment to add your own
bed temperature line
;M109 S210 ;Uncomment to add your own
temperature line
G21        ;metric values
G90        ;absolute positioning
M82        ;set extruder to absolute
mode
M107       ;start with the fan off
G28 X0 Y0  ;move X/Y to min endstops
G28 Z0     ;move Z to min endstops
G1 Z15.0 F9000 ;move the platform down
15mm
G92 E0                  ;zero the
extruded length
G1 F200 E3              ;extrude 3mm
of feed stock
G92 E0                  ;zero the
extruded length again
G1 F9000
;Put printing message on LCD screen
M117 Printing...

;Layer count: 13
;LAYER:0
M107

;LAYER:1
M106 S255
G0 F9000 X15.65 Y0.000  Z1.000
;TYPE:WALL-OUTER
G1 F2400 E0.00000

G1 X15.65 Y0.000 F4800

G1 X15.65 Y15.65 E1.000
G1 X1.15 Y15.65 E2.000
G1 X1.15 Y1.15 E3.000
G1 X15.65 Y1.15 E4.000
; solid layer

G0 X1.15 Y3.52 F4800

G1 X13.28 Y3.52 E1.000 F1007
G1 X13.28 Y5.96 E2.000
G1 X3.52 Y5.96 E3.000
G1 X3.52 Y8.4 E4.000
G1 X13.28 Y8.4 E5.000
G1 X13.28 Y10.84 E6.000
G1 X3.52 Y10.84 E7.000
G1 X3.52 Y13.28 E8.000
G1 X13.28 Y13.28 E9.000


;LAYER:2
M106 S255
G0 F9000 X15.65 Y0.000  Z2.000
;TYPE:WALL-OUTER
G1 F2400 E0.00000

G1 X15.65 Y0.000 F4800

G1 X15.65 Y15.65 E1.000
G1 X1.15 Y15.65 E2.000
G1 X1.15 Y1.15 E3.000
G1 X15.65 Y1.15 E4.000
; solid layer

G0 X13.28 Y1.15 F4800

G1 X13.28 Y13.28 E1.000 F1007
G1 X10.84 Y13.28 E2.000
G1 X10.84 Y3.52 E3.000
G1 X8.4 Y3.52 E4.000
G1 X8.4 Y13.28 E5.000
G1 X5.96 Y13.28 E6.000
G1 X5.96 Y3.52 E7.000
G1 X3.52 Y3.52 E8.000
G1 X3.52 Y13.28 E9.000

;LAYER:3
M106 S255
G0 F9000 X15.65 Y0.000  Z3.000
;TYPE:WALL-OUTER
G1 F2400 E0.00000

G1 X15.65 Y0.000 F4800

G1 X15.65 Y15.65 E1.000
G1 X1.15 Y15.65 E2.000
G1 X1.15 Y1.15 E3.000
G1 X15.65 Y1.15 E4.000
; solid layer

G0 X1.15 Y3.52 F4800

G1 X13.28 Y3.52 E1.000 F1007
G1 X13.28 Y5.96 E2.000
G1 X3.52 Y5.96 E3.000
G1 X3.52 Y8.4 E4.000
G1 X13.28 Y8.4 E5.000
G1 X13.28 Y10.84 E6.000
G1 X3.52 Y10.84 E7.000
G1 X3.52 Y13.28 E8.000
G1 X13.28 Y13.28 E9.000
M84                         ;steppers
off
G90                         ;absolute
positioning
```

`

```
;LAYER:4
M106 S255
G0 F9000 X15.65 Y0.000  Z4.000
;TYPE:WALL-OUTER
G1 F2400 E0.00000

G1 X15.65 Y0.000 F4800

G1 X15.65 Y15.65 E1.000
G1 X1.15 Y15.65 E2.000
G1 X1.15 Y1.15 E3.000
G1 X15.65 Y1.15 E4.000
; solid layer

G0 X13.28 Y1.15 F4800

G1 X13.28 Y13.28 E1.000 F1007
G1 X10.84 Y13.28 E2.000
G1 X10.84 Y3.52 E3.000
G1 X8.4 Y3.52 E4.000
G1 X8.4 Y13.28 E5.000
G1 X5.96 Y13.28 E6.000
G1 X5.96 Y3.52 E7.000
G1 X3.52 Y3.52 E8.000
G1 X3.52 Y13.28 E9.000

;LAYER:5
M106 S255
G0 F9000 X15.65 Y0.000  Z5.000
;TYPE:WALL-OUTER
G1 F2400 E0.00000

G1 X15.65 Y0.000 F4800

G1 X15.65 Y15.65 E1.000
G1 X1.15 Y15.65 E2.000
G1 X1.15 Y1.15 E3.000
G1 X15.65 Y1.15 E4.000
; solid layer

G0 X1.15 Y3.52 F4800

G1 X13.28 Y3.52 E1.000 F1007
G1 X13.28 Y5.96 E2.000
G1 X3.52 Y5.96 E3.000
G1 X3.52 Y8.4 E4.000
G1 X13.28 Y8.4 E5.000
G1 X13.28 Y10.84 E6.000
G1 X3.52 Y10.84 E7.000
G1 X3.52 Y13.28 E8.000
G1 X13.28 Y13.28 E9.000


;LAYER:6
M106 S255
G0 F9000 X15.65 Y0.000  Z6.000
;TYPE:WALL-OUTER
G1 F2400 E0.00000

G1 X15.65 Y0.000 F4800

G1 X15.65 Y15.65 E1.000
G1 X1.15 Y15.65 E2.000
G1 X1.15 Y1.15 E3.000
G1 X15.65 Y1.15 E4.000
; solid layer

G0 X13.28 Y1.15 F4800

G1 X13.28 Y13.28 E1.000 F1007
G1 X10.84 Y13.28 E2.000
G1 X10.84 Y3.52 E3.000
G1 X8.4 Y3.52 E4.000
G1 X8.4 Y13.28 E5.000
G1 X5.96 Y13.28 E6.000
G1 X5.96 Y3.52 E7.000
G1 X3.52 Y3.52 E8.000
G1 X3.52 Y13.28 E9.000

;LAYER:7
M106 S255
G0 F9000 X15.65 Y0.000  Z7.000
;TYPE:WALL-OUTER
G1 F2400 E0.00000

G1 X15.65 Y0.000 F4800

G1 X15.65 Y15.65 E1.000
G1 X1.15 Y15.65 E2.000
G1 X1.15 Y1.15 E3.000
G1 X15.65 Y1.15 E4.000
; solid layer

G0 X1.15 Y3.52 F4800

G1 X13.28 Y3.52 E1.000 F1007
G1 X13.28 Y5.96 E2.000
G1 X3.52 Y5.96 E3.000
G1 X3.52 Y8.4 E4.000
G1 X13.28 Y8.4 E5.000
G1 X13.28 Y10.84 E6.000
G1 X3.52 Y10.84 E7.000
G1 X3.52 Y13.28 E8.000
G1 X13.28 Y13.28 E9.000


;LAYER:8
M106 S255
G0 F9000 X15.65 Y0.000  Z8.000
;TYPE:WALL-OUTER
G1 F2400 E0.00000

G1 X15.65 Y0.000 F4800

G1 X15.65 Y15.65 E1.000
G1 X1.15 Y15.65 E2.000
G1 X1.15 Y1.15 E3.000
G1 X15.65 Y1.15 E4.000
; solid layer

G0 X13.28 Y1.15 F4800

G1 X13.28 Y13.28 E1.000 F1007
G1 X10.84 Y13.28 E2.000
```

`

```
G1 X10.84 Y3.52 E3.000
G1 X8.4 Y3.52 E4.000
G1 X8.4 Y13.28 E5.000
G1 X5.96 Y13.28 E6.000
G1 X5.96 Y3.52 E7.000
G1 X3.52 Y3.52 E8.000
G1 X3.52 Y13.28 E9.000

;LAYER:9
M106 S255
G0 F9000 X15.65 Y0.000  Z9.000
;TYPE:WALL-OUTER
G1 F2400 E0.00000

G1 X15.65 Y0.000 F4800

G1 X15.65 Y15.65 E1.000
G1 X1.15 Y15.65 E2.000
G1 X1.15 Y1.15 E3.000
G1 X15.65 Y1.15 E4.000
; solid layer

G0 X1.15 Y3.52 F4800

G1 X13.28 Y3.52 E1.000 F1007
G1 X13.28 Y5.96 E2.000
G1 X3.52 Y5.96 E3.000
G1 X3.52 Y8.4 E4.000
G1 X13.28 Y8.4 E5.000
G1 X13.28 Y10.84 E6.000
G1 X3.52 Y10.84 E7.000
G1 X3.52 Y13.28 E8.000
G1 X13.28 Y13.28 E9.000


;LAYER:10
M106 S255
G0 F9000 X15.65 Y0.000  Z10.000
;TYPE:WALL-OUTER
G1 F2400 E0.00000

G1 X15.65 Y0.000 F4800

G1 X15.65 Y15.65 E1.000
G1 X1.15 Y15.65 E2.000
G1 X1.15 Y1.15 E3.000
G1 X15.65 Y1.15 E4.000
; solid layer

G0 X13.28 Y1.15 F4800

G1 X13.28 Y13.28 E1.000 F1007
G1 X10.84 Y13.28 E2.000
G1 X10.84 Y3.52 E3.000
G1 X8.4 Y3.52 E4.000
G1 X8.4 Y13.28 E5.000
G1 X5.96 Y13.28 E6.000
G1 X5.96 Y3.52 E7.000
G1 X3.52 Y3.52 E8.000
G1 X3.52 Y13.28 E9.000

;LAYER:11
M106 S255
G0 F9000 X15.65 Y0.000  Z11.000
;TYPE:WALL-OUTER
G1 F2400 E0.00000

G1 X15.65 Y0.000 F4800

G1 X15.65 Y15.65 E1.000
G1 X1.15 Y15.65 E2.000
G1 X1.15 Y1.15 E3.000
G1 X15.65 Y1.15 E4.000
; solid layer

G0 X1.15 Y3.52 F4800

G1 X13.28 Y3.52 E1.000 F1007
G1 X13.28 Y5.96 E2.000
G1 X3.52 Y5.96 E3.000
G1 X3.52 Y8.4 E4.000
G1 X13.28 Y8.4 E5.000
G1 X13.28 Y10.84 E6.000
G1 X3.52 Y10.84 E7.000
G1 X3.52 Y13.28 E8.000
G1 X13.28 Y13.28 E9.000


;LAYER:12
M106 S255
G0 F9000 X15.65 Y0.000  Z12.000
;TYPE:WALL-OUTER
G1 F2400 E0.00000

G1 X15.65 Y0.000 F4800

G1 X15.65 Y15.65 E1.000
G1 X1.15 Y15.65 E2.000
G1 X1.15 Y1.15 E3.000
G1 X15.65 Y1.15 E4.000
; solid layer

G0 X13.28 Y1.15 F4800

G1 X13.28 Y13.28 E1.000 F1007
G1 X10.84 Y13.28 E2.000
G1 X10.84 Y3.52 E3.000
G1 X8.4 Y3.52 E4.000
G1 X8.4 Y13.28 E5.000
G1 X5.96 Y13.28 E6.000
G1 X5.96 Y3.52 E7.000
G1 X3.52 Y3.52 E8.000
G1 X3.52 Y13.28 E9.000


M107
;End GCode
M104 S0                     ;extruder
heater off
M140 S0                     ;heated
bed heater off (if you have it)
G91
;relative positioning
G1 E-1 F300
;retract the filament a bit before
```

`

```
lifting the nozzle, to release some of
the pressure
G1 Z+0.5 E-5 X-20 Y-20 F9000 ;move Z
up a bit and retract filament even
more
```

```
G28 X0 Y0
;move X/Y to min endstops, so the head
is out of the way
M84                         ;steppers
off
G90                         ;absolute
positioning
```

[0,45,90-45]$_3$ Cube with Outline Perimeter

```
M109 S210.000000
;Sliced at: Mon 20-11-2017 12:24:19
;Basic settings: Layer height: 1
Walls: 1 Fill: 0
;Print time: 2 hours 43 minutes
;Filament used: 4.605m 36.0g
;Filament cost: None
;M190 S70 ;Uncomment to add your own
bed temperature line
;M109 S210 ;Uncomment to add your own
temperature line
G21        ;metric values
G90        ;absolute positioning
M82        ;set extruder to absolute
mode
M107       ;start with the fan off
G28 X0 Y0  ;move X/Y to min endstops
G28 Z0     ;move Z to min endstops
G1 Z15.0 F9000 ;move the platform down
15mm
G92 E0                  ;zero the
extruded length
G1 F200 E3              ;extrude 3mm
of feed stock
G92 E0                  ;zero the
extruded length again
G1 F9000
;Put printing message on LCD screen
M117 Printing...

;Layer count: 13
;LAYER:0
M107

;LAYER:1
M106 S255
G0 F9000 X15.65 Y0.000  Z1.000
;TYPE:WALL-OUTER
G1 F2400 E0.00000

G1 X15.65 Y0.000 F4800

G1 X15.65 Y15.65 E1.000
G1 X1.15 Y15.65 E2.000
G1 X1.15 Y1.15 E3.000
G1 X15.65 Y1.15 E4.000
; solid layer

G0 X1.15 Y3.52 F4800

G1 X13.28 Y3.52 E1.000 F1007
G1 X13.28 Y5.96 E2.000
G1 X3.52 Y5.96 E3.000
G1 X3.52 Y8.4 E4.000
G1 X13.28 Y8.4 E5.000
G1 X13.28 Y10.84 E6.000
G1 X3.52 Y10.84 E7.000
G1 X3.52 Y13.28 E8.000
G1 X13.28 Y13.28 E9.000

;LAYER:2
M106 S255
G0 F9000 X15.65 Y0.000  Z2.000
;TYPE:WALL-OUTER
G1 F2400 E0.00000

G1 X15.65 Y0.000 F4800

G1 X15.65 Y15.65 E1.000
G1 X1.15 Y15.65 E2.000
G1 X1.15 Y1.15 E3.000
G1 X15.65 Y1.15 E4.000
; solid layer

G0 X13.28 Y1.15 F4800

G1 X13.28 Y4.531 E1.000 F1007
G1 X12.269 Y3.52 E2.000
G1 X8.819 Y3.52 E3.000
G1 X13.28 Y7.981 E4.000
G1 X13.28 Y11.432 E5.000
G1 X5.368 Y3.52 E6.000
G1 X3.52 Y3.52 E7.000
G1 X3.52 Y5.123 E8.000
G1 X11.677 Y13.28 E9.000
G1 X8.227 Y13.28 E10.000
G1 X3.52 Y8.573 E11.000
G1 X3.52 Y12.024 E12.000
G1 X4.776 Y13.28 E13.000
G1 X3.52 Y13.28 E14.000

;LAYER:3
M106 S255
G0 F9000 X15.65 Y0.000  Z3.000
;TYPE:WALL-OUTER
G1 F2400 E0.00000

G1 X15.65 Y0.000 F4800

G1 X15.65 Y15.65 E1.000
G1 X1.15 Y15.65 E2.000
G1 X1.15 Y1.15 E3.000
G1 X15.65 Y1.15 E4.000
; solid layer

G0 X13.28 Y1.15 F4800
```

`

```
G1 X13.28 Y13.28 E1.000 F1007
G1 X10.84 Y13.28 E2.000
G1 X10.84 Y3.52 E3.000
G1 X8.4 Y3.52 E4.000
G1 X8.4 Y13.28 E5.000
G1 X5.96 Y13.28 E6.000
G1 X5.96 Y3.52 E7.000
G1 X3.52 Y3.52 E8.000
G1 X3.52 Y13.28 E9.000



;LAYER:4
M106 S255
G0 F9000 X15.65 Y0.000  Z4.000
;TYPE:WALL-OUTER
G1 F2400 E0.00000

G1 X15.65 Y0.000 F4800

G1 X15.65 Y15.65 E1.000
G1 X1.15 Y15.65 E2.000
G1 X1.15 Y1.15 E3.000
G1 X15.65 Y1.15 E4.000
; solid layer

G0 X1.15 Y3.52 F4800

G1 X4.531 Y3.52 E1.000 F1007
G1 X3.52 Y4.531 E2.000
G1 X3.52 Y7.981 E3.000
G1 X7.981 Y3.52 E4.000
G1 X11.432 Y3.52 E5.000
G1 X3.52 Y11.432 E6.000
G1 X3.52 Y13.28 E7.000
G1 X5.123 Y13.28 E8.000
G1 X13.28 Y5.123 E9.000
G1 X13.28 Y8.573 E10.000
G1 X8.573 Y13.28 E11.000
G1 X12.02 Y13.28 E12.000
G1 X13.28 Y12.02 E13.000
G1 X13.28 Y13.28 E14.000

;LAYER:5
M106 S255
G0 F9000 X15.65 Y0.000  Z5.000
;TYPE:WALL-OUTER
G1 F2400 E0.00000

G1 X15.65 Y0.000 F4800

G1 X15.65 Y15.65 E1.000
G1 X1.15 Y15.65 E2.000
G1 X1.15 Y1.15 E3.000
G1 X15.65 Y1.15 E4.000
; solid layer

G0 X1.15 Y3.52 F4800

G1 X13.28 Y3.52 E1.000 F1007
G1 X13.28 Y5.96 E2.000
G1 X3.52 Y5.96 E3.000
G1 X3.52 Y8.4 E4.000
G1 X13.28 Y8.4 E5.000
G1 X13.28 Y10.84 E6.000
G1 X3.52 Y10.84 E7.000
G1 X3.52 Y13.28 E8.000
G1 X13.28 Y13.28 E9.000

;LAYER:6
M106 S255
G0 F9000 X15.65 Y0.000  Z6.000
;TYPE:WALL-OUTER
G1 F2400 E0.00000

G1 X15.65 Y0.000 F4800

G1 X15.65 Y15.65 E1.000
G1 X1.15 Y15.65 E2.000
G1 X1.15 Y1.15 E3.000
G1 X15.65 Y1.15 E4.000
; solid layer

G0 X13.28 Y1.15 F4800

G1 X13.28 Y4.531 E1.000 F1007
G1 X12.269 Y3.52 E2.000
G1 X8.819 Y3.52 E3.000
G1 X13.28 Y7.981 E4.000
G1 X13.28 Y11.432 E5.000
G1 X5.368 Y3.52 E6.000
G1 X3.52 Y3.52 E7.000
G1 X3.52 Y5.123 E8.000
G1 X11.677 Y13.28 E9.000
G1 X8.227 Y13.28 E10.000
G1 X3.52 Y8.573 E11.000
G1 X3.52 Y12.024 E12.000
G1 X4.776 Y13.28 E13.000
G1 X3.52 Y13.28 E14.000

;LAYER:7
M106 S255
G0 F9000 X16.8 Y15.65  Z7.000
;TYPE:WALL-OUTER
G1 F2400 E0.00000

G1 X16.8 Y15.65 F4800

G1 X1.15 Y15.65 E1.000
G1 X1.15 Y1.15 E2.000
G1 X15.65 Y1.15 E3.000
G1 X15.65 Y15.65 E4.000
; solid layer

G0 X13.28 Y1.15 F4800

G1 X13.28 Y13.28 E1.000 F1007
G1 X10.84 Y13.28 E2.000
G1 X10.84 Y3.52 E3.000
G1 X8.4 Y3.52 E4.000
G1 X8.4 Y13.28 E5.000
G1 X5.96 Y13.28 E6.000
G1 X5.96 Y3.52 E7.000
G1 X3.52 Y3.52 E8.000
```

`

```
G1 X3.52 Y13.28 E9.000



;LAYER:8
M106 S255
G0 F9000 X16.8 Y15.65  Z8.000
;TYPE:WALL-OUTER
G1 F2400 E0.00000

G1 X16.8 Y15.65 F4800

G1 X1.15 Y15.65 E1.000
G1 X1.15 Y1.15 E2.000
G1 X15.65 Y1.15 E3.000
G1 X15.65 Y15.65 E4.000
; solid layer

G0 X1.15 Y3.52 F4800

G1 X4.531 Y3.52 E1.000 F1007
G1 X3.52 Y4.531 E2.000
G1 X3.52 Y7.981 E3.000
G1 X7.981 Y3.52 E4.000
G1 X11.432 Y3.52 E5.000
G1 X3.52 Y11.432 E6.000
G1 X3.52 Y13.28 E7.000
G1 X5.123 Y13.28 E8.000
G1 X13.28 Y5.123 E9.000
G1 X13.28 Y8.573 E10.000
G1 X8.573 Y13.28 E11.000
G1 X12.02 Y13.28 E12.000
G1 X13.28 Y12.02 E13.000
G1 X13.28 Y13.28 E14.000

;LAYER:9
M106 S255
G0 F9000 X16.8 Y15.65  Z9.000
;TYPE:WALL-OUTER
G1 F2400 E0.00000

G1 X16.8 Y15.65 F4800

G1 X1.15 Y15.65 E1.000
G1 X1.15 Y1.15 E2.000
G1 X15.65 Y1.15 E3.000
G1 X15.65 Y15.65 E4.000
; solid layer

G0 X1.15 Y3.52 F4800

G1 X13.28 Y3.52 E1.000 F1007
G1 X13.28 Y5.96 E2.000
G1 X3.52 Y5.96 E3.000
G1 X3.52 Y8.4 E4.000
G1 X13.28 Y8.4 E5.000
G1 X13.28 Y10.84 E6.000
G1 X3.52 Y10.84 E7.000
G1 X3.52 Y13.28 E8.000
G1 X13.28 Y13.28 E9.000

;LAYER:10
M106 S255
G0 F9000 X16.8 Y15.65  Z10.000
;TYPE:WALL-OUTER
G1 F2400 E0.00000

G1 X16.8 Y15.65 F4800

G1 X1.15 Y15.65 E1.000
G1 X1.15 Y1.15 E2.000
G1 X15.65 Y1.15 E3.000
G1 X15.65 Y15.65 E4.000
; solid layer

G0 X13.28 Y1.15 F4800

G1 X13.28 Y4.531 E1.000 F1007
G1 X12.269 Y3.52 E2.000
G1 X8.819 Y3.52 E3.000
G1 X13.28 Y7.981 E4.000
G1 X13.28 Y11.432 E5.000
G1 X5.368 Y3.52 E6.000
G1 X3.52 Y3.52 E7.000
G1 X3.52 Y5.123 E8.000
G1 X11.677 Y13.28 E9.000
G1 X8.227 Y13.28 E10.000
G1 X3.52 Y8.573 E11.000
G1 X3.52 Y12.024 E12.000
G1 X4.776 Y13.28 E13.000
G1 X3.52 Y13.28 E14.000

;LAYER:11
M106 S255
G0 F9000 X16.8 Y15.65  Z11.000
;TYPE:WALL-OUTER
G1 F2400 E0.00000

G1 X16.8 Y15.65 F4800

G1 X1.15 Y15.65 E1.000
G1 X1.15 Y1.15 E2.000
G1 X15.65 Y1.15 E3.000
G1 X15.65 Y15.65 E4.000
; solid layer

G0 X13.28 Y1.15 F4800

G1 X13.28 Y13.28 E1.000 F1007
G1 X10.84 Y13.28 E2.000
G1 X10.84 Y3.52 E3.000
G1 X8.4 Y3.52 E4.000
G1 X8.4 Y13.28 E5.000
G1 X5.96 Y13.28 E6.000
G1 X5.96 Y3.52 E7.000
G1 X3.52 Y3.52 E8.000
G1 X3.52 Y13.28 E9.000



;LAYER:12
M106 S255
G0 F9000 X16.8 Y15.65  Z12.000
;TYPE:WALL-OUTER
```

`

```
G1 F2400 E0.00000

G1 X16.8 Y15.65 F4800

G1 X1.15 Y15.65 E1.000
G1 X1.15 Y1.15 E2.000
G1 X15.65 Y1.15 E3.000
G1 X15.65 Y15.65 E4.000
; solid layer

G0 X1.15 Y3.52 F4800

G1 X4.531 Y3.52 E1.000 F1007
G1 X3.52 Y4.531 E2.000
G1 X3.52 Y7.981 E3.000
G1 X7.981 Y3.52 E4.000
G1 X11.432 Y3.52 E5.000
G1 X3.52 Y11.432 E6.000
G1 X3.52 Y13.28 E7.000
G1 X5.123 Y13.28 E8.000
G1 X13.28 Y5.123 E9.000
G1 X13.28 Y8.573 E10.000
G1 X8.573 Y13.28 E11.000
G1 X12.02 Y13.28 E12.000
G1 X13.28 Y12.02 E13.000
G1 X13.28 Y13.28 E14.000


M107
;End GCode
M104 S0                     ;extruder
heater off
M140 S0                     ;heated
bed heater off (if you have it)
G91
;relative positioning
G1 E-1 F300
;retract the filament a bit before
lifting the nozzle, to release some of
the pressure
G1 Z+0.5 E-5 X-20 Y-20 F9000 ;move Z
up a bit and retract filament even
more
G28 X0 Y0
;move X/Y to min endstops, so the head
is out of the way
M84                         ;steppers
off
G90                         ;absolute
positioning
```